

THE BOUNCING BOULDERS OF THE ATACAMA

A Thesis

Presented to the Faculty of the Graduate School

of Cornell University

In Partial Fulfillment of the Requirements for the Degree of

Master of Science

by

Paul Monroe Morgan

August 2020

© 2020 Paul Monroe Morgan

## ABSTRACT

In the heart of Chile's Atacama Desert thousands of boulders, some exceeding 5 m in diameter, lie at the bases of steep escarpments. The rapid and forceful descents of the boulders are commonly recorded by the trails of small impact craters the boulders left as they bounced down the escarpments. These craters are exquisitely preserved thanks to the hyper-arid climate of the Atacama, the driest place on Earth. Once at rest, most boulders experience no further downslope motion but instead degrade in place. These unique boulder fields preserve thousands of fallen boulders in various states of degradation, from solid intact boulders to conical mounds of debris.

This thesis focuses on one of the several previously undescribed fallen boulder fields in the Coastal Cordillera between  $19^{\circ}$  and  $23^{\circ}$ S latitude. We characterize this site using field surveys, boulder morphology classifications, and a drone-based structure from motion (SfM) digital elevation model (DEM) in order to exploit the unparalleled preservation of the evidence of past rock falls. The rapid descent of individual boulders suggests triggering by either earthquakes or infrequent rainfall events; we have experienced the former in the field. The spacing of bounce marks left by the boulders as they fell down the scarp are irregular, and their paths are commonly oblique to the maximum slope line, highlighting the stochastic nature of the impact process, and confirming the importance of probabilistic three-dimensional rock fall models. We describe the state of degradation of the boulders using a three-fold classification for relative age of the boulders based on the relative size of their debris skirts, and find that larger numbers of morphologically older boulders are found

further out from the scarp. We also identify a morphometric approach using slope and slope roughness to identify boulder source regions. The uniquely preserved fields of fallen boulders in the Atacama provide an excellent case study to test theories of the processes important to determine rock fall hazards.

## BIOGRAPHICAL SKETCH

Paul Morgan

Paul Morgan was raised in California, where he attended the University of California Santa Cruz and received a B.S. in Earth Science with a minor in Physics. During his undergraduate experience Paul developed a passion for geology through both his field experiences during courses and field camp, and his geophysical research experiences during an internship and his thesis project. After graduating he worked as a research assistant at the Earth Observatory of Singapore for two and a half years, where he studied subduction zone earthquakes using primarily GPS data. Interested in working on field based research Paul embarked on this Masters Thesis project focused on boulder fields in Chile's Atacama Desert with Professor Richard Allmendinger.

During his Master's study Paul was lucky enough to travel to Chile twice and experience the inspiring and other-worldly Atacama Desert. His life was also greatly enriched by the Cornell community, the natural beauty of the finger lakes, and the ever changing seasons of Ithaca, New York. This thesis was finished in a very lucky, healthy, and comfortable quarantine at Paul's home on Cayuga Lake during the COVID-19 global pandemic. Upon graduation, Paul plans to continue learning about the earth and pursue a PhD at the University of Washington.

## ACKNOWLEDGMENTS

First I'd like to acknowledge my funding sources:

- This material was based upon work supported by the US National Science Foundation Graduate Research Fellowship to P.M.M. under Grant No. DGE-1650441.
- The Cornell Fellowship from the Department of Earth and Atmospheric Sciences
- Research funds from Cornell University awarded to and administered by Richard W. Allmendinger that brought me to Chile for field work
- The Bloom fund in the department of Earth and Atmospheric Sciences for helping to pay my way to Chile

Personally I would like to acknowledge...

- My previous advisors who's mentorship has helped me grow academically and whose insights I have surely brought with me to this project, including: Emily Brodsky, Emma Hill, and Lujia Feng.
- Professor Gabriel González for his scientific advice and generosity in the lending of drones from his lab.
- Yerko González, Jean Loins Luciano, and especially Lester Olivares for making the field campaigns successful and enjoyable.
- Friends in Ithaca including but not limited to: Taylor Cyle, Rebekah Minchew, Kyle Murray, Frankie Zhu, Kevin Reath, Casey Root, Martik Chatterjee, Lester Olivarez, Nicolas Rangel Jurado.
- EAS staff- especially Savannah Williams who always had an expert ear for my administrative issues and who not only welcomed me to the department, but made me feel welcome in the department.
- My committee members Matt Pritchard, and especially Terry Jordan, who's expertise and curiosity helped turn this rough manuscript into a formal scientific thesis.
- Professor Rick Allmendinger, for being a curious, thoughtful, and understanding teacher; as well as a strong advocate for good science and interpersonal kindness. I have learned so much more from him than what is presented in this thesis.
- My partner Paula Bürgi, to whom I am grateful for bringing me to Cornell, for her love, encouragement, support, and feedback.

## TABLE OF CONTENTS

<b>ABSTRACT .....</b>	<i>i</i>
<b>BIOGRAPHICAL SKETCH .....</b>	<i>iii</i>
<b>ACKNOWLEDGMENTS .....</b>	<i>iv</i>
<b>TABLE OF CONTENTS .....</b>	<i>v</i>
<b>CH.1: INTRODUCTION.....</b>	<b>7</b>
<b>CH.2: THE CHINCHILLA BOULDER FIELD AS A CASE STUDY OF THE BOUNCING BOULDERS OF THE ATACAMA.....</b>	<b>11</b>
<b>1. Introduction .....</b>	<b>11</b>
<b>2. Background .....</b>	<b>15</b>
2.1: The Atacama Desert.....	15
2.2 The Study Area: The Chuculay Fault System.....	16
2.3 Rockfall hazard.....	18
<b>4. Data collection .....</b>	<b>19</b>
<b>5. Observations .....</b>	<b>23</b>
5.1 Escarpment Scale morphological zones and boulder field.....	23
5.2 Boulder characteristics, morphology and degradation.....	26
5.3 Boulder tracks .....	30
<b>6. Analysis.....</b>	<b>35</b>
6.1 Fall direction relative to slope .....	35
6.2 Bounce Kinematics and the Coefficient of Restitution .....	35
6.3 Boulder distribution .....	41
6.4 Boulder field density and scarp morphology .....	43
<b>7 Discussion .....</b>	<b>48</b>
7.1 Fall trigger mechanism.....	48
7.2 The rock fall.....	50
7.3 The bounces .....	51
7.4 After a boulder has landed .....	52
7.5 Spatial variation of boulder falls .....	54
<b>8. Conclusions .....</b>	<b>55</b>
<b>REFERENCES .....</b>	<b>57</b>
<b>CH.3: CONCLUSION.....</b>	<b>61</b>
<b>REFERENCES .....</b>	<b>64</b>
<b>APPENDIX .....</b>	<b>65</b>
<b>Section A1: Where are the boulder fall fields? .....</b>	<b>65</b>
<b>Section A2: Initial scarp morphology mapping.....</b>	<b>68</b>

<b>Section A3: Field boulder survey .....</b>	<b>71</b>
<b>Section A4: Testing standard deviation of local slope as an age proxy for fallen boulders.</b>	<b>78</b>
<b>Section A5: Boulder tracing, and scarp morphology comparisons.....</b>	<b>81</b>
<b>Section A6: Bounce kinematics calculations .....</b>	<b>87</b>
<b>REFERENCES.....</b>	<b>98</b>

## CHAPTER 1

### INTRODUCTION



**Figure i.1** A photo taken looking North at the Atajaña Fault of northern Chile. In the center is a boulder which fell during or shortly after the 2014  $M_W$  8.1 Pisagua earthquake. The bounce marks it left are visible as white spots on the escarpment. Chelsea Scott for scale. Location [19.298026 S, 70.172420 W]

In 2014 a two meter tall boulder was dislodged from its perch at least 400 meters up on the Atajaña fault scarp, northern Chile, during or shortly after the Pisagua  $M_w$  8.1 earthquake (Fig. i1). The ensuing rapid, energetic, and bouncing decent was exquisitely recorded by the impact craters it made on the scarp and adjacent flats, at one point landing on and shattering a stationary boulder lying in its path. This boulder came to rest ~300 m from the foot of the scarp at the distal margin of a field of thousands of boulders with a similarly rapid and energetic transport history. The aprons of debris built up around some degrading boulders indicate that they disintegrate in place after coming to rest, and are preserved by the hyper-arid climate of the driest place on earth. Yet the 2014 boulder was the only clast of its size in some 20 km of scarp length to be shaken loose during that great earthquake. This event captures the nature of the bouncing boulder fields of the Atacama. This thesis will characterize these unique field sites, and show how these boulder-fall fields provide insights into the nature of rockfalls in general.

The correlation of boulder fall with a major plate boundary earthquake raises the question: can the boulders function as a paleoseismic tool? If we knew the precise ages of a few boulder falls, perhaps we could even use their degradation as a proxy for age, and end up with enough ages to robustly date past earthquakes. Prior to our first field season, we used Google maps to search for boulder fall fields within northern Chile (Appendix 1). During our first field season, Teresa Jordan (Cornell Professor), Richard Allmendinger (Cornell Professor and advisor on this project), and I scouted several boulder fall fields at the base of steep escarpments including the Atajaña scarp, the Pisagua scarp, Caleta Punta Arenas, and the Chuculay scarps (CH. 2 Fig. 2), investigating the features of the boulder fields, looking for datable material, and taking photos to create 3D models of select boulders (Appendix 4). However, during this field season and after we realized that dating the boulder falls using geochronometric techniques like

cosmogenic nuclide exposure ages, or optically stimulated luminescence ages would be a difficult, long, expensive, and possibly futile task, likely not suited for a Masters study. A general characterization of the boulder fields would be necessary prior to investing in the dating.

After the first field season, we used Google Earth and Bing satellite imagery to map the geomorphic features of 3 scarps with boulder fields (Appendix 2), recording the extents of the boulder fields, exposed bedrock, fluvial features. This experience demonstrated that the freely available satellite imagery and globally available Digital Elevation Models (DEM's) were not high enough resolution to probe the processes at the scale of individual boulders, and helped us choose areas for detailed field work. We chose Chuculay for our primary field site for two reasons. First, the Chinchilla fault within the Chuculay fault system had all of the features we wished to study: variations in boulder density, extensive bounce mark preservation, and many boulders with debris aprons. The second is accessibility: Chuculay is relatively accessible, whereas Atajaña is very remote and far from our base in Antofogasta. We also collected data at Caleta Punta Arenas along the Coastal Escarpment, in case we wanted a study to focus on comparing and contrasting different boulder fields. However, gaps in the drone imagery coverage, including our inability to image the high scarp crest, inhibited the creation of a coherent orthomosaic image and DEM of Caleta Punta Arenas which led us to focus on Chuculay.

During the second field season I was accompanied by Lester Olivares (Cornell), Yerko González (Universidad Católica del Norte, Antofagasta; UCN, and Jean Loins Luciano (UCN). First, we spent 5 days collecting drone imagery for the creation of orthomosaics and DEMs, with the help of drone pilot Yerko González. Then we used the drone imagery to survey boulders and characterize the topography with the help of Jean Loins Luciano, for 4 more days. The data

collected during the second field season constitute almost all of the quantitative information analyzed in this thesis.

While characterizing the boulder fall fields, we began to focus on their unique insights into the processes of rockfalls. In most of the world where rockfalls occur, the evidence they leave is ephemeral and washed away by normal surface processes, however within the Atacama Desert the surface processes are not normal. In addition, a vast majority of the rockfall literature describes rockfalls that have occurred in temperate mountain environments and not deserts. By asking what controls the location density of boulders at the base of the scarp, we investigated methods for determining rockfall source areas, and in trying to quantify the information left by the bounce marks we helped to constrain the physics of bouncing rocks. Both of these findings have real world impacts for rockfall hazard and mitigation.

This thesis includes one primary chapter, appendices, and a conclusion in addition to this introductory chapter. In the primary chapter we first characterize the boulder fields, then analyze our data primarily collected through mapping the drone imagery. The main chapter finishes with a discussion of the lifespan of a boulder from what triggered its fall, to what direction it fell and how it bounced, and ending with it degrading at the base of the scarp making up one piece of the spatially variable boulder field as a whole. Appendices detail research that complements the main chapter, but is superseded by further analysis in presented in the main chapter, or provides a more in-depth analysis into peripheral aspects of the study. The final chapter discusses future work that could be done to understand the boulder fields and use these unique study sites to learn about other processes.

## CHAPTER 2

### THE CHINCHILLA BOULDER FIELD AS A CASE STUDY OF THE BOUNCING BOULDERS OF THE ATACAMA

#### *1. Introduction*

In the heart of Chile's Atacama Desert, thousands of boulders lie at the bases of steep escarpments. Though the boulders rest and degrade in place today, their energetic transport to their final resting place is commonly told by the trails of small impact craters the boulders left as they bounced down the escarpments. These impact craters are exquisitely preserved thanks to the hyperarid climate of the Atacama, the driest place on Earth. To tell the story of past rock falls, we use the uniquely preserved data provided by the previously unstudied rockfall-sourced boulder fields of the Atacama.

Three main features of the preserved boulder fields form the focus of this work. First, the trails of impact craters that the rocks left as they bounced and rolled are commonly still visible, such as those leading up to boulder 1 in Figure 1. Second, after coming to rest, when the rocks start to degrade, the resulting clasts are not washed away. This degradation in place transforms solid rocks (Fig. 1, boulder 1) into conical mounds of debris (Fig. 1, boulder 2). Finally, because the fallen rocks degrade very slowly in the absence of precipitation, the boulder fields (Fig. 1, middle ground) record a long history of many rockfalls.

The spacing of bounce marks in single tracks is irregular, highlighting the stochastic nature of rock-ground bounces, and confirming the importance of probabilistic rockfall models (Li & Lan, 2015). We divide the boulders into three classes, based on the relative sizes of their

debris skirts, assuming that younger boulders would have less debris surrounding them. A larger number of morphologically older boulders are found further out from the scarp. The long-preserved history of rockfalls at the base of the scarp, as recorded at the scale of the entire escarpment, helps to identify rockfall source areas, an important step in most rockfall hazard assessments (Dunham et al., 2017; Fanos & Pradhan, 2018; F. Ferrari et al., 2016). A morphometric approach using slope roughness works well to identify boulder source regions. In this study we will examine these three unique features in detail at the rockfall fields along the Chinchilla fault, of the Chuculay fault system (Fig. 2).

We review first the relevant previous studies focused on the Atacama desert and other types of boulder fields, our primary field site, and rockfalls in general. Then we will describe our observations of relevant features starting at the escarpment scale, and zooming in to the boulder scale and the preserved bounce marks. After that we will go over our analysis and calculations, and end with a discussion following the life span of the fallen boulders starting with their fall trigger, moving through the fall and bounces, and ending with its degradation and place in the boulder fall field as a whole.



**Figure 1.** A photo taken looking south at the Chinchilla Fault of the Chuculay fault system. Three important features of Atacama boulder fields are: a trail of depressions marking the fall path of boulder 1, boulders in a “fresh” state (boulder 1) and boulders in a degraded state (boulder 2, 4, & 5), and the large number of boulders in the midground at the base of the escarpment. Boulders are numbered with labels corresponding to Fig. 4b. Location [69.806488°W 21.093914°S]

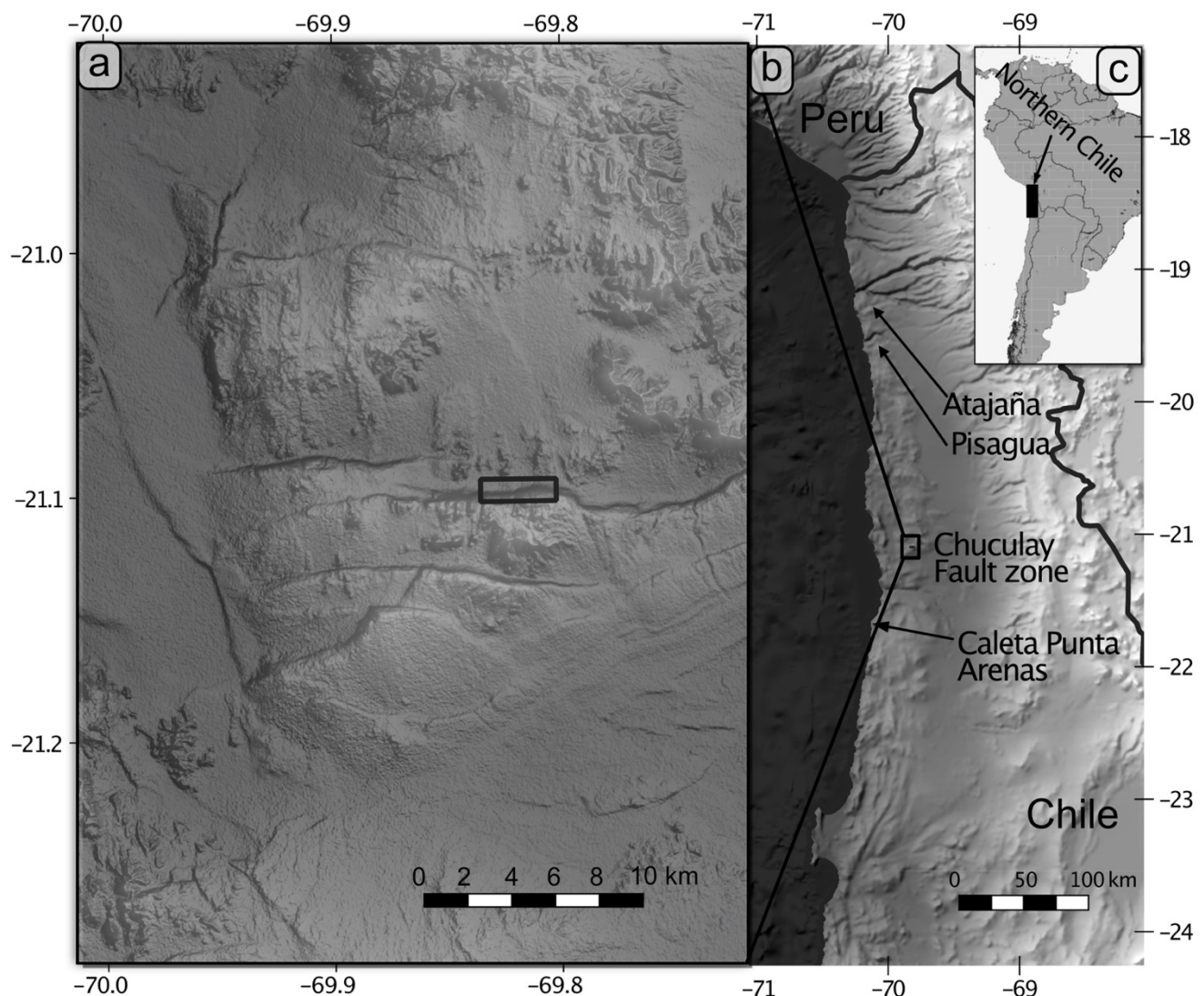


**Figure 2.** (a) our primary field site along the Chinchilla fault of the Chuculay fault System in Northern Chile. Background hillshade is from the 30 m SRTM DEM. The black outline shows the region of detailed data collection represented in figure 3. (b) Locations of other field sites referred to in the text, and part (a).

## **2. Background**

### **2.1: The Atacama Desert**

The Atacama Desert is unique because of the hyper-aridity of the climate, and thus the exceptionally slow erosion rates. Over the study area, the annual average precipitation is well under 10 mm/year (Houston, 2006) and likely closer to 0.5-1 mm/year (Schween, Hoffmeister, & Löhnert, 2020). This hyper-aridity is the result of atmospheric, oceanic and topographic influences. General atmospheric high pressures at these sub-tropical latitudes decrease convection and thus precipitation. The Humboldt Current brings cold water to the surface along the Pacific coast, decreasing the moisture capacity of onshore winds, and leads to temperature inversions (Houston, 2006; Rutllant, 2003). Finally, regionally the Atacama Desert lies in the rain shadow of the Andes to the east, blocking moisture from the Atlantic, and locally the Chuculay site is on the east side of the Coastal Cordillera which acts as a rain shadow for moisture from the Pacific (Houston, 2006). Though rain is rare, the coastal inversion often leads to heavy coastal fog (locally referred to as “Camanchaca”) encroaching inland, increasing salt and gypsum weathering (Goudie, Wright, & Viles, 2002). While debated, the onset of hyper-aridity throughout much of the Atacama Desert is thought to have occurred by around 14 MA (Jordan et al., 2014; Rech, Currie, Michalski, & Cowan, 2006), though there may have been some shorter term wetter periods during the late Pliocene or Pleistocene (Amundson et al., 2012; Placzek et al., 2014). This long-lived hyper-aridity is responsible for the preservation of the boulder fields.

Other types of boulder fields in the southern Atacama desert have already been the subject of several studies (Matmon et al., 2015; Placzek et al., 2014; Quade et al., 2012; Sager et

al., 2020). However, none of these studies examined rockfalls, or the resulting fields of disintegrating boulders with visible debris skirts. Instead, those authors focused on cosmogenic nuclide exposure ages for a variety of landforms across the Atacama, documenting high exposure ages [ $>10$  Ma] for monolithic boulders transported down relatively shallow slopes. Quade et al. (2012) argued that seismicity plays a role in the transport and rocking of similar boulders on low-angle slopes. They found cosmogenic nuclide exposure ages of 0.6 - 2 Ma (Quade et al., 2012). Matmon et al. (2015) summarized and characterized these boulder fields further proposing boulder transport in stages due to seismic shaking.

## **2.2 The Study Area: The Chuculay Fault System**

We have observed rockfall fields at the base of several fresh escarpments in the Atacama (Appendix A), however, in this study we focus primarily on the Chinchilla fault scarp in the Chuculay fault system (Espina Ibáñez, 2011) (Fig. 2), hereafter referred to as Chuculay. This south-dipping East-striking reverse fault accommodates trench-parallel shortening of the forearc. The trench-parallel shortening likely results from the concave-seaward geometry of the plate margin (Allmendinger, González, Yu, Hoke, & Isacks, 2005). We also compare this site to a site studied in less detail along Northern Chile's coastal escarpment at Caleta Punta Arenas and call on additional observations made along the Atajaña fault scarp, 200 km to the north (Fig. 2b).

Locally the Chinchilla fault produced over 340 m of topographic relief (~950 m above sea level at the base) and is the largest scarp of the Chuculay fault system (Espina Ibáñez, 2011). The fault is likely of early Miocene to Pliocene age. Carrizo et al. (2008) used cosmogenic nuclide exposure measurements to date at between 15 and 24 Ma quartz clasts on a paleo-surface offset by the fault system, marking the probable maximum age for the faults. Using similar techniques, they dated an offset channel at the fringe of the fault system at  $3.92 \pm 0.11$  Ma

which, if representative of the entire fault system, suggests that all of the offset occurred during the late Pliocene to recent (Carrizo et al., 2008).

The planar erosional surfaces dated by Carrizo et al. (2008) are covered by air fall tuff deposits, which underlie the boulder fields. One such ash layer located ~5 km from our field site and, like the ash in our field area, is rich in biotite; that tuff yielded an age of  $0.31 \pm 0.19$  Ma (Carrizo et al., 2008). A tuff covering the surface located closer to the field site has been dated at  $1.41 \pm 0.02$  Ma (Vásquez et al., 2018). Preserved morphological fault scarps and local crustal seismicity (Sippl, Schurr, Asch, & Kummerow, 2018) suggest that faulting is ongoing, with several events with east west striking thrust fault focal mechanisms in the area (Salazar et al., 2017). This geologically recent activity makes the Chuculay fault system one of the largest and freshest topographic features in the central Atacama Desert.

On an adjacent fault strand of the Chuculay fault system, horizons within lobate tongues of fine sediment on hillslopes were dated using OSL (optically stimulated luminescence) indicating hillslope activity (possibly triggered by soil humidity or seismic slumping) at ~18 ka. Other internal horizons within the fine sediment lobes were dated as young as  $1.9 \pm 0.3$  ka and as old as  $105 \pm 9.5$  ka (May et al., 2020), though how these layers were formed and/or transported is not entirely clear. On another hillslope, 22 km northwest from our field site, of similar dimensions (~200 m tall) but lacking a steep exposed bedrock crest and scree, the shallowest layer was dated at  $35.6 \pm 3.5$  ka, with several meters of accumulated sediment within 130 ka (including pulses from 35-80 ka and 100-130 ka) (Medialdea et al., 2020). These studies indicate that the youngest slope surfaces in the region are likely tens of thousands of years old, though stable surfaces approach hundreds of thousands to millions of years (Medialdea et al., 2020).

The bedrock underlying the study area is the Chuculay monzonitic complex, comprised mostly of monzonites and monzodiorites (Vásquez et al. 2018). Due to hyperaridity unique to the Atacama, in most locations the bedrock is covered by thick layers of evaporite-mineral dominated soils (May et al., 2020). These soils are accreting from aeolian and atmospheric origin, and include gypsum, anhydrite, nitrate, and/or iodate (Ewing et al., 2006). The uppermost layer in the soil is often a powdery layer of evaporite minerals ten plus centimeters thick called “Chusca”. The surface along the base of the escarpment is made up of the powdery chusca, sometimes with a mm scale “crisp” crust, scattered angular clasts varying in density and size (2 cm to tens of centimeters), and of course the boulders. Local landforms at the base of the escarpment include 10 m in diameter areas of stronger salt crusts.

### **2.3 Rockfall hazard**

A wealth of studies addresses rockfall from the engineering geology/hazard perspectives. The first step in identifying rockfall hazards is often a qualitative assessment, where an expert will inspect and rate potentially dangerous rock slopes, as well as assess the risk posed by potential rock falls (F. Ferrari et al., 2016). The identification of source zones is often accomplished by analyzing slope morphometrics like slope steepness and roughness (Fanos & Pradhan, 2018; Frattini et al., 2008; Marquinez et al., 2003) or, in more detailed geomechanical studies, using specific fractures and overhang geometries (Dunham et al., 2017; Fanos & Pradhan, 2018).

Once a source for potential rockfalls is found, one way to decide on the proper mitigation is to use process-based rockfall simulation models to find how far potential rockfalls may runout. Rocks can move downhill in 4 ways: freefall, sliding, bouncing, and rolling (Dorren, 2003). Models simulating these processes have been used and refined for decades (Dorren, 2003;

Pfeiffer and Higgins, 1990; Wu, 1984). These rockfall simulations require a model of the topography the rock is falling over, estimates of the source zone of the rock, estimates of possible size and shape of the falling rock (though it is often simulated as a lumped mass), and the setting of some parameters which determine how the rock slows down as it rolls or bounces (Dorren, 2003). These slowing parameters may vary spatially to reflect different material properties of the runout zone or remain static, and often include coefficients of friction for a rolling rock, and a coefficient of restitution to define the bounces (Dorren, 2003).

The coefficient of restitution (COR) is a kinematic metric (Dorren, 2003; Guzzetti et al., 2015; Pfeiffer & Higgins, 1990) that is defined by the ratio between a rock's velocity into a bounce point to the rock's velocity as it rebounds out of the bounce, as defined in equation 1.

$$COR = V_{out}/V_{in} \quad (1)$$

A perfectly elastic collision where the falling rock loses no energy to the ground would have a COR value of one. Often the COR value is broken up into its normal and tangential components, these are often given values from 0.2 to 0.5 and 0.4 to 0.9 respectively (Guzzetti et al., 2002). Though not the only method to quantify what happens during a bounce (Lu et al., 2019), the COR is a commonly used metric, and because the bounce marks provide us a window into the rock's bounce, we will focus on the COR.

#### **4. Data collection**

During an initial field campaign, we spent ~7 days investigating and scouting boulder fall fields of the Atacama, including at the Atajaña and Pisagua scarps as well as locations along the coastal escarpment (Fig. 2). During a second field campaign, we spent 9 days collecting detailed data at our primary field site at Chuculay. In the field, we cataloged boulders along three 50 m

wide transects perpendicular to the escarpments, recording boulders size, shape, rock type, fractures, and size of their debris apron (Appendix 3). A five-tier morphologic classification system in the field was based on the percent of the boulder covered by its debris apron; here, we have simplified this to a three-class system that would be identifiable in person and in high resolution imagery (see section 5.2).

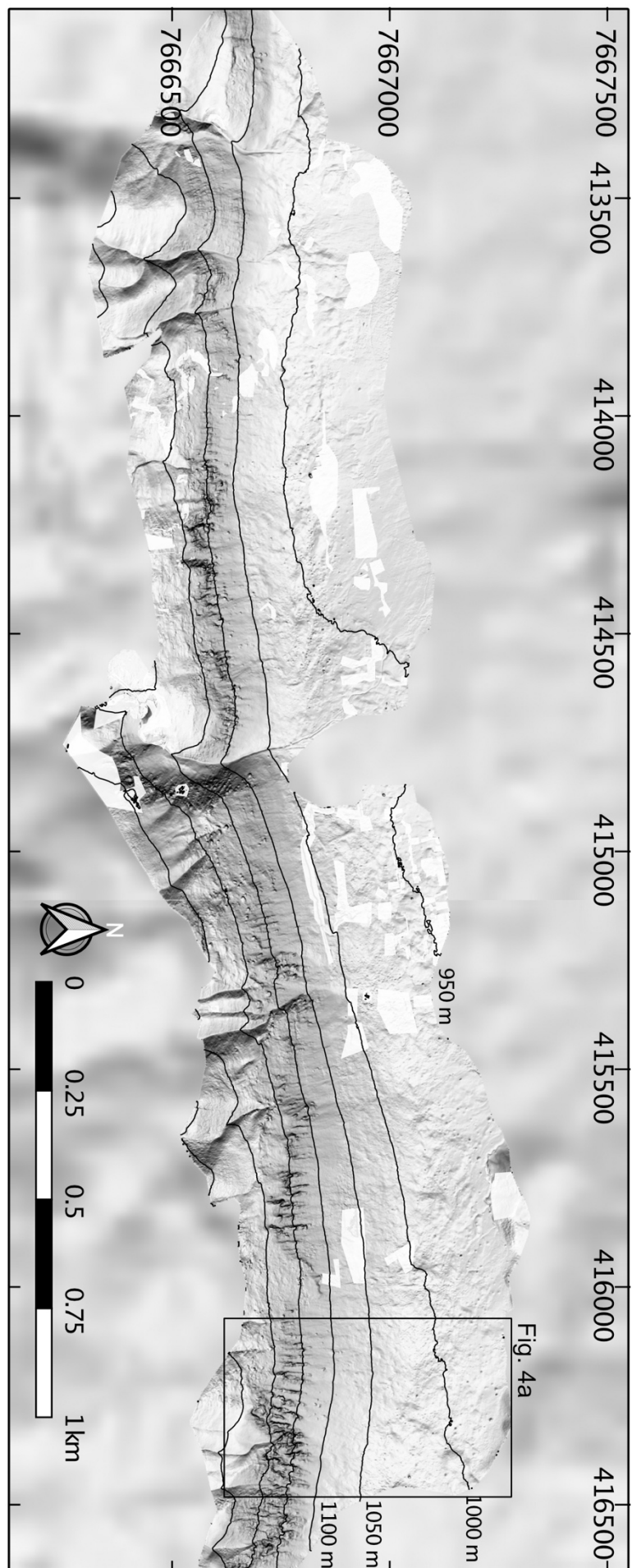
We used satellite imagery available through Google Earth and Bing (Between ~1m and 30 cm resolution), to complete some initial mapping of the morphologic features of the escarpments, including extents of the boulder fields in the deposit zones, area of exposed bedrock, and alluvial features (Appendix 2). We used these maps to choose the extent of our primary study area. We found that the freely available satellite imagery, and 30 m resolution SRTM (Shuttle Radar Topography Mission) DEM (Digital Elevation Model) were not high enough resolution to capture the fine details illuminating individual boulders.

Our primary base maps were made using high resolution drone photogrammetry, which is well suited to the vegetation-free environment of the Atacama. Our drone imagery covers a 3 km long segment of the Chinchilla scarp from which an orthomosaic image and a high-resolution DEM were created using structure from motion photogrammetry implemented in Agisoft Photoscan (Fig. 3). The aerial imagery was collected using two different drones on several different flights to cover the entire field area. Due to the separate flights, the quality of the imagery and DEM vary throughout the study area with some alignment errors producing blurred imagery and sharp digital elevation artifacts (blocked by the white polygons in Fig. 3). Maximum resolution of the DEM and imagery in some key test areas is 10 cm. Visibility of certain features, like the bounce marks, is also dependent on sun angle, which varies between each flight in each location. Despite these inconsistencies, the drone-based imagery and DEM

form high resolution base maps capturing the information needed to categorize individual boulders and see bounce marks. Through the rest of this study we use the drone-based DEM, which is usually down sampled to a 1 m horizontal resolution.

Using the drone ortho-imagery, we manually traced as ellipses all boulders with a minimum diameter exceeding two meters along the ~3 km stretch of scarp imaged. Recorded with the location of each boulder is a descriptor of its degradation morphology, using the 1-3 remote classification scale described more fully in section 5.2. We also marked the center of every bounce mark that we could find leading up to a boulder.

**Figure 3** Hillshade map of digital elevation models at two resolutions. The central section shows the high-resolution digital elevation model (DEM) created using drone imagery. The background hillshade map is based on the SRTM DEM. Fifty meter interval contours are plotted on the drone DEM. DEM errors are masked with white polygons. Border labels are Eastings and Northings corresponding to WGS 84 UTM zone 19s.



## **5. Observations**

We describe three different aspects of the boulders: (1) the broad-scale characteristics of the boulder field and the accompanying scarp, (2) boulder characteristics and morphology classes, and (3) evidence of boulder transport recorded in the desert surface. Here, we focus observations made at Chuculay, but also draw on observations made along the Atajaña scarp and the Pisagua scarp ~200 km to the north (Fig. 2).

### **5.1 Escarpment Scale morphological zones and boulder field**

The part of the Chuculay escarpment described here is about 3 km long and in this section, its relief varies from 200 to 350 m. The fault offsets older topographic hills visible on the footwall and hanging wall. This relict topography is made up of 10°-25° steep smooth slopes on the order of 100 m in height and a few hundred meters from crest to crest. The 3 km section of the scarp spans regions with both higher and lower concentrations of fallen boulders, that are hundreds of meters in length along the scarp front. This variability enables us to compare the morphology of areas with and without many boulder falls.

In any transect across the escarpment, there are four distinct regions of the escarpment (Fig. 4c). At the base of the escarpment with slopes of less than 10° is the boulder deposit zone, which locally exhibits hummocky microtopography. This zone has many large boulders (>1 m in average dimension) lying on top of a mix of “Chusca soils” and angular cobbles. Above the deposit zone occurs a smooth talus slope composed mostly of loose cobbles, which we refer to as the transport zone. The boundary between the transport zone and deposit zone is marked as the base of the escarpment or scarp front. Large boulders are found below the boundary, and just

below the boundary or at the boundary there is commonly a large density or piling up of colluvial cobbles to small boulders (< 1 m). In the transport zone slope exceeds 10° and the surface is mostly covered by colluvial cobbles. At the top of the transport zone talus slope, exposed bedrock forms the steepest slopes on the escarpment, from 40° to 60°, and discrete 1-5 m wide ribs are commonly separated by gullies (Fig. 1 top center). We refer to this bedrock region as the source zone (Fig. 4). The slope continues upward from these bedrock exposures, albeit at gentler angles of 20-30°, in a region we refer to as the uplands. The uplands include some evidence of heavily weathered bedrock, chusca soil cover, and extensive surface cracks which evolved as the fault headwall uplifted and stretched over the footwall (González et al., 2008).

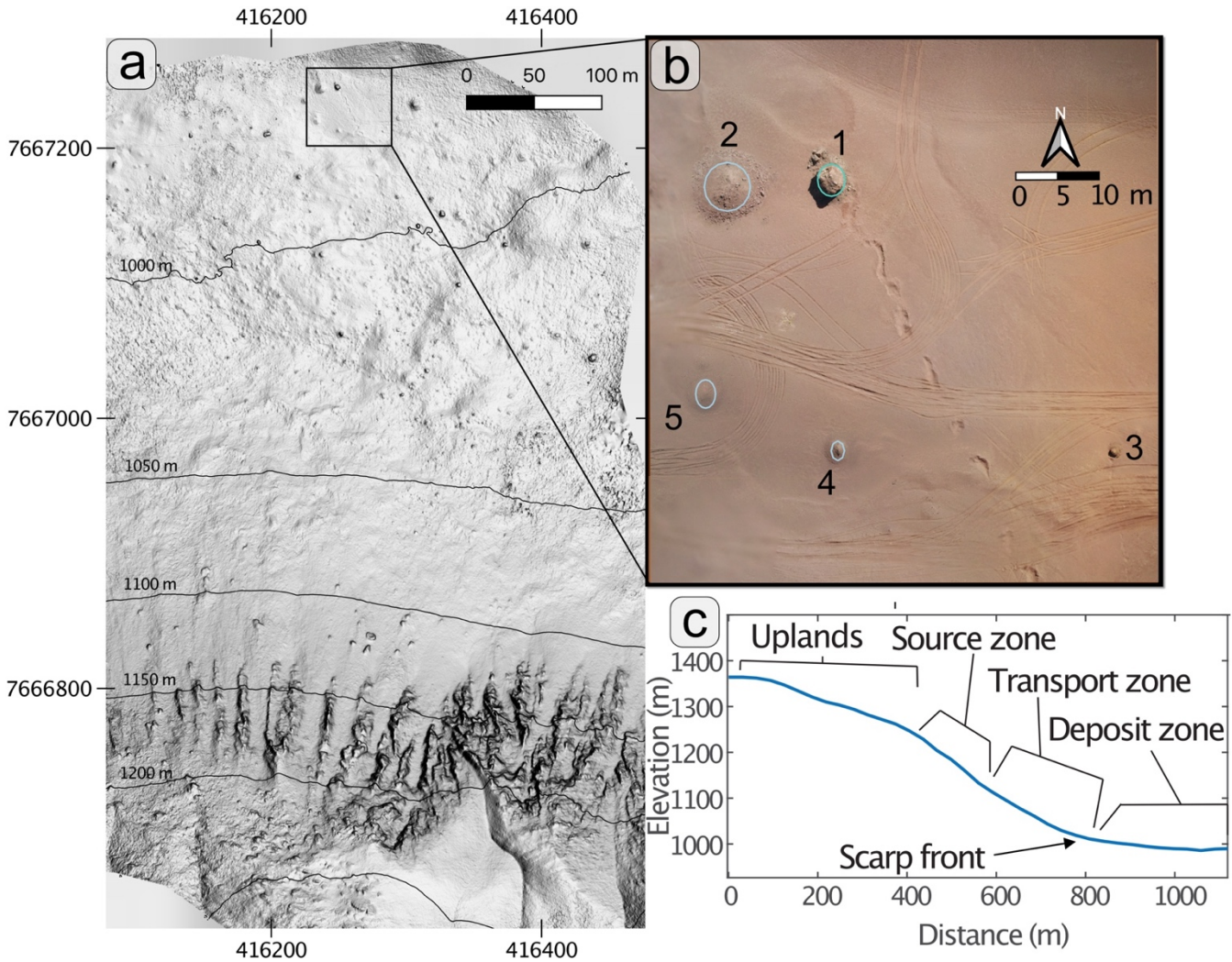


**Figure 4(a)** Detailed hillshade inset of the eastern-most portion of the study area of the Chinchilla fault scarp from the drone-based digital elevation model (located on Fig. 3). Each boulder with a diameter greater than 2 m is traced with an oval as described in section 4. (b) High resolution imagery from the inset in (a) boulders are labeled with numbers matching those of Figure 1. (c) is a generalized cross section illustrating the different sections of the escarpment, with no vertical exaggeration.

## 5.2 Boulder characteristics, morphology and degradation

At Chuculay, the boulders are composed primarily of Mesozoic igneous rocks from the Chuculay monzonitic complex (Vásquez et. al, 2018), that are commonly brecciated and/or fractured (Fig. 5). This is a contrast to the monolithic and unfractured boulders collected in fields elsewhere in the Atacama (Matmon et al., 2015; Quade et al., 2012). Forty of the 146 boulders surveyed at Chuculay had regular sets of more or less parallel fractures, with a range of spacing between fractures from 1-2 cm to 40 cm (Fig. 5c). The fractures are occasionally filled with and cemented with gypsum and/or halite (Fig 5a). The fact that the breccias hold together during catastrophic falls attests to the strength of the gypsum and/or halite cement. At Atajaña (Fig. 2), the boulders are much less brecciated and composed of Cretaceous conglomerate.

At Chuculay we observed boulders with a variety of shapes. During our field catalog we recorded that many boulders have a more or less circular footprint, and that for 92% of the boulders of the long axis of their footprint is less than twice as long than the short axis (Fig. 5d). We also observed that a majority of the boulders are shorter or much shorter than they are long. For only 25% of the boulders surveyed, the average footprint length was less than twice the height of the boulder (Fig. 5d).

Of course, in addition to the 0.5-10 m boulders, the deposit zones are also covered with innumerable small boulders and cobbles, but we cannot tell the nature of their travel downslope. The options include that a cobble fell or diffused downslope as an individual clasts, that it spalled off of a falling boulders during collisions, or that it weathered off of a disintegrating boulder after the parent boulder came to rest. After the boulders come to rest there is no evidence that they move again, except in relatively rare cases where they are incorporated into coarse

grained debris flows that result from infrequent precipitation events or they are involved in a collision with another falling boulder.

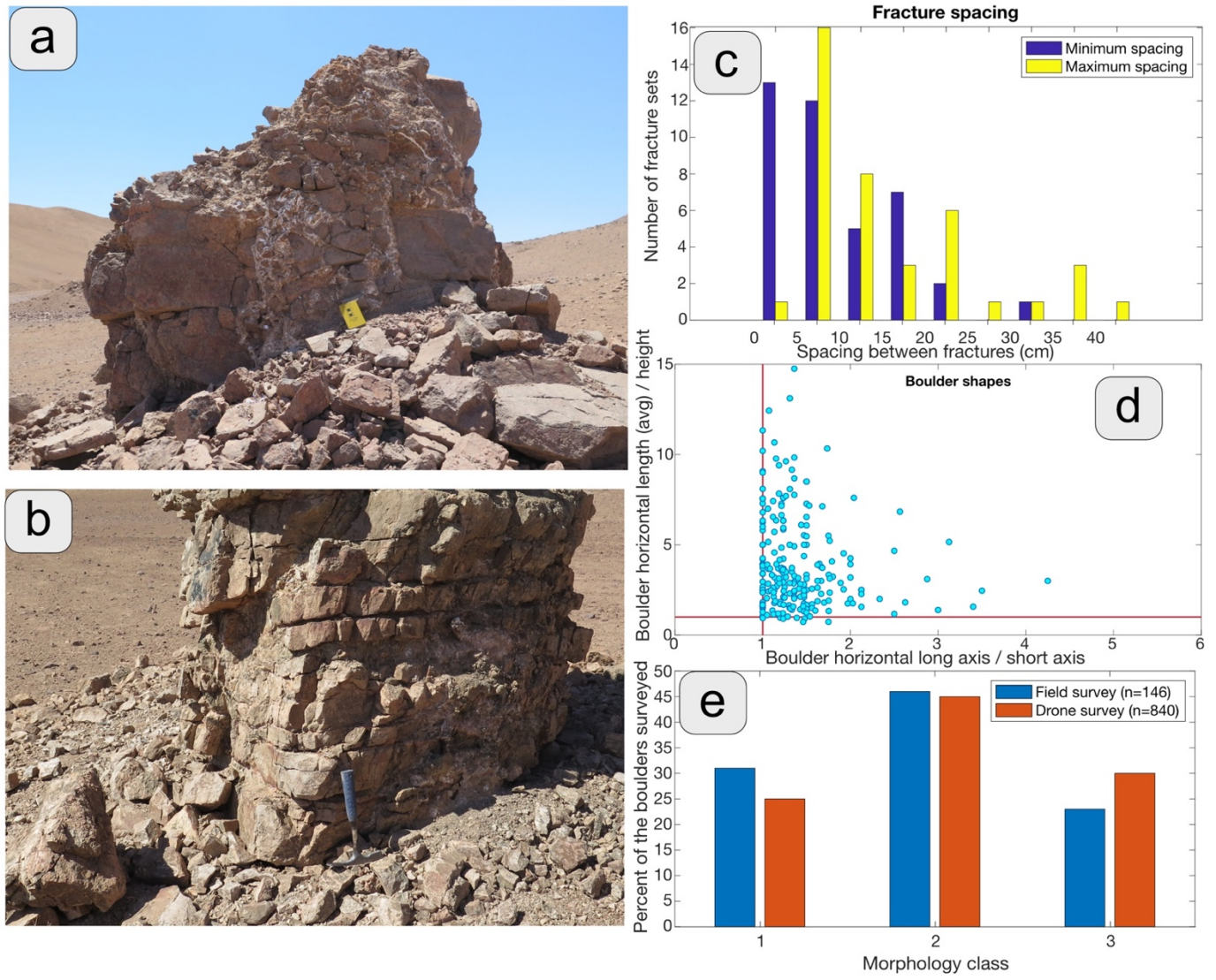


**Figure 5** Detailed images of the boulders at Chuculay. a) Fractured and brecciated boulder showing evaporite cementation. b) heavily fractured boulder, with apron clasts reflecting the dimensions and forms of the boulder fractures. c) Recorded fracture spacing from boulder survey, using field measurements that only recorded minimum and maximum spacing of sets of fractures. This plot represents the range of values rather than the relative abundance. d) The shapes of the boulders measured during the field survey, x axis represents the boulder long axis/boulder short axis. Y axis value is the ratio of the horizontal axis (the average of the long axis and short axis) and the height of the boulder, the shorter a boulder is compared to its length the larger the value is. Red lines are at  $x = 1$  and  $y = 1$ ; a spherical boulder or cubic boulder would lie at the (1,1) point. e) Number of boulders of each morphology class recorded during the field survey (blue), and the drone imagery survey (red).

We observe boulders in all phases of their lifespan in the deposit zone. Some boulders appear “fresher”, with near vertical sides or overhangs, and no apron of debris surrounding them. With time, they begin to break apart and an apron of debris forms around the boulder. Though a wide range of sizes of clasts in the apron occur, the diameters and shape of clasts in the apron appear to depend on the source rock, for example at Chuculay the tens of centimeter diameter angular clasts in the apron are similar to the size of clasts within the breccia or between fractures in the source rocks (Fig. 5b). The debris apron grows in height and width at the expense of the boulder and in the end member case, a conical mound is all that remains of the boulder. Where we have excavated the mounds, a core of fractured and disintegrating rock can commonly be found.

To classify the degree of degradation, we developed a three-tier morphology scale for the boulders that is diagnosable in the field or on the drone imagery. Class 1 boulders (Fig. 6, a and d) have little to no debris — fallen clasts have not begun to pile up around all sides of the boulder. Class 2 boulders (Fig. 6, b and e) are surrounded by clasts that have begun to pile up in a debris apron, but the parent boulder is still at least twice as tall as the debris apron. Class 3 boulders (Fig. 6, c and f) are conical mounds of debris or boulders with a debris apron that is greater than 60% the height of the core boulder. While we observed more class 2 boulders than class 1 or 3 boulders in the drone and field surveys (Fig. 5e), a majority of those class 2 boulders had smaller aprons, between 10 and 20% of the total boulder height.

During our field survey and drone imagery assessments we found similar relative abundances of the different class boulders. Class 2 being the most abundant type of boulder, making up around 45% of the boulders surveyed.

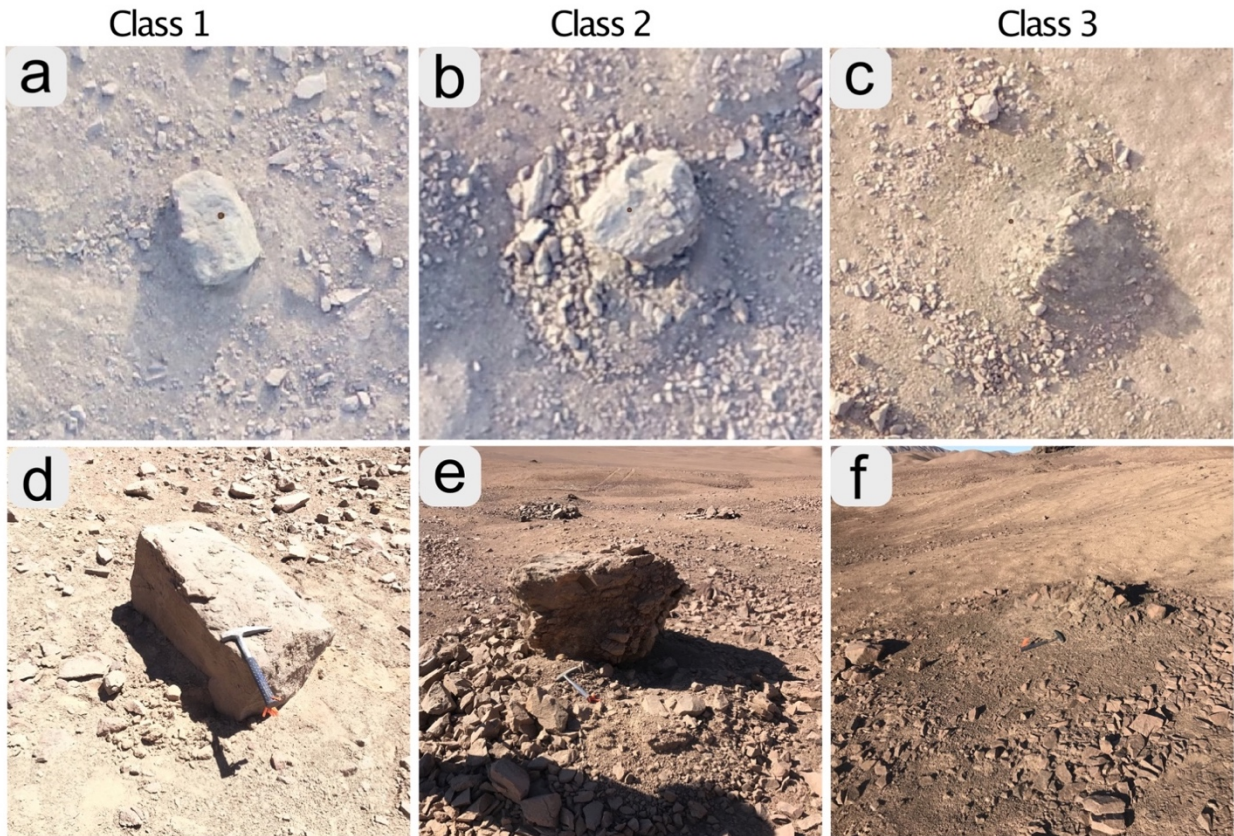


**Figure 6** Drone imagery (a-c) and field photo's (d-f) of three example boulders illustrating the distinctions between the morphology classes. Top row and bottom row images are of the same boulders. Rock hammer in bottom photos for scale.

### 5.3 Boulder tracks

Evidence for rapid descent of fresh or large boulders comes from well preserved tracks left in the desert floor. Sets of oval depressions can be followed up-slope from individual boulders within the deposit zone, primarily within areas of predominantly fine-grained material.

The bounce marks are preserved infrequently within the transport zone (they were observed at Atajaña, but not Chuculay). The depressions vary in size from tens of centimeters across and less than 5 cm deep to 2-3 m across and ~0.5-1 m deep, depending on the size of the rock that created it. They are usually elongated in the travel direction of the boulder, and deeper on the downhill end. The microtopography shows that, often, the fine grained “chusca” soils have been pushed up at the down-slope end and/or the sides of individual depressions indicating that the depressions are formed by impacts of the boulder with the surface.

The boulder fields along the Atajaña fault scarp 200 km north of Chuculay shed additional light on the processes associated with boulder descent. There, we observed three months after the 2014 Pisagua  $M_w$  8.1 earthquake a freshly fallen boulder (Fig. 7a), about 100 km from the epicenter. At that time the bounce marks had sharply defined rims. The pits exposed fine grained sediment that was much lighter in tone than the surrounding surfaces, and outside the pits there were light-colored zones. We infer that the light colors inside and outside indicate that the shallow sub-surface chusca was ejected upon impact, and its deposit is the light-colored material outside the pit. We re-observed the same boulder and associated bounce marks in October, 2017 (Fig. 7b). Over that three years span, the boulder impacts, though still quite visible, had lost some of their well-defined outline, were partially filled with aeolian sand, and their initial color had darkened. More significantly, in 2014, individual bounce marks were visible at least half way up the talus slope (transport zone); those marks were mostly erased by 2017, suggesting that the near angle-of-repose slopes recover quickly from impact damage. Additionally, during field work in 2017, the authors were camped out at Atajaña when a  $M_w$  6.8 earthquake occurred in the subducted plate at 85 km depth and ~90 km northeast of the scarp. The following morning several fresh boulder tracks made by small boulders and clasts were

observed on the talus-covered part of the scarp where none had been noticed in the previous days. We have not revisited that scarp since, but suspect that those tracks are no longer visible.

In the orthomosaic constructed from drone photography at Chuculay, we identified 31 tracks of bounce marks leading up to boulders in a 3 km long section field area (Fig. 8). We mapped the center of visible depressions, and did not distinguish between possible short rolls and bounces, because mostly distinct depressions were visible. The mosaic and drone topography show that several bounce tracks are oblique to the direction of maximum slope. The orthomosaic also reinforces field observations that the bounce mark spacing is quite irregular. In general, the spacing diminishes as the boulders approached their final destination, but this general trend is overshadowed by a large variance in spacing of the bounce marks before the last few bounces. This phenomenon is explored in greater detail in section 6.2. Finally, the track maps from the orthomosaic show that a significant curl commonly occurs in the final ~10 m of the boulder trajectory (Fig. 8).

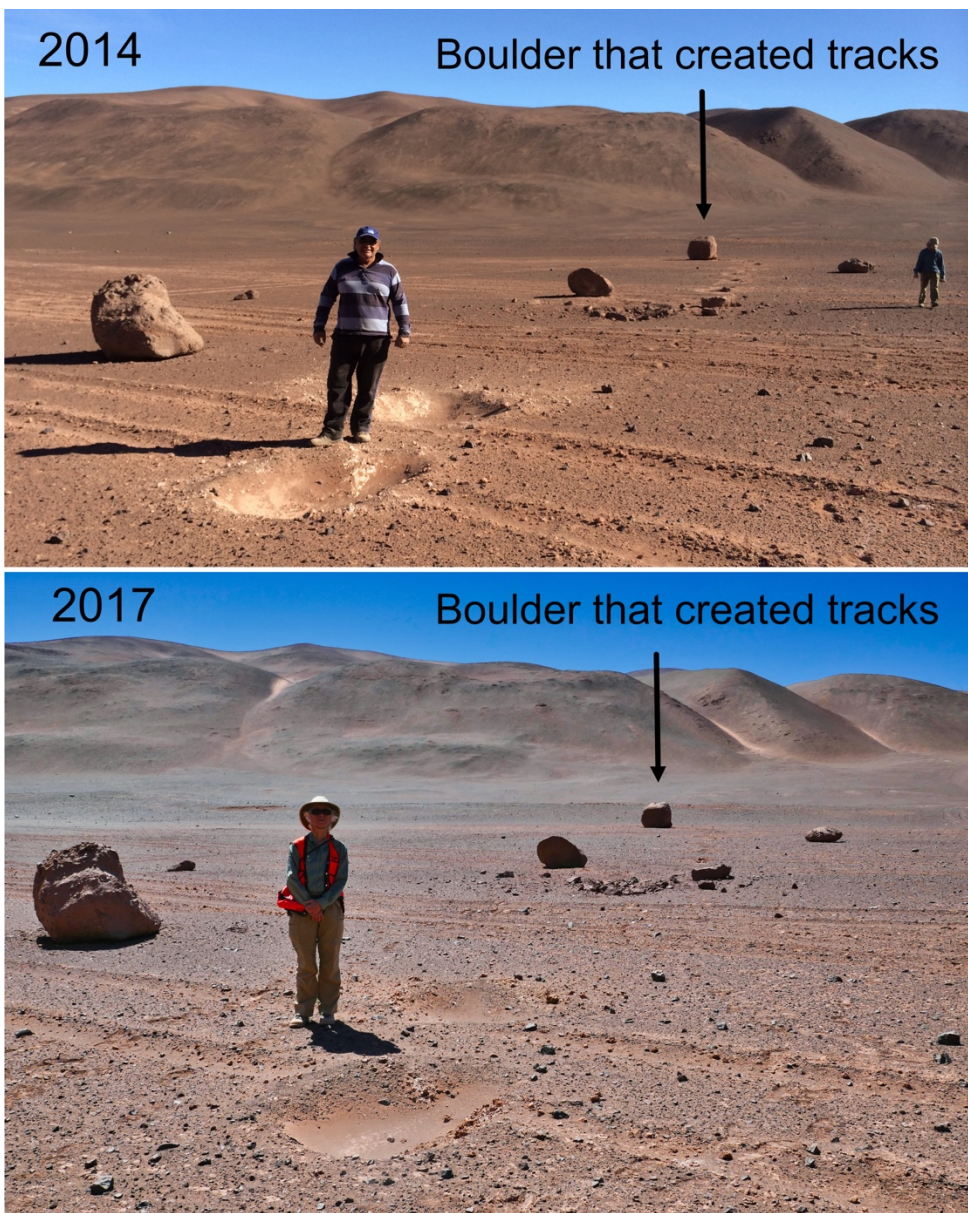


**Figure 7** Photos of the same bounce marks at Atajaña on two different dates. Photo A, taken in July 2014, 3 months after an earthquake, shows bounce marks that obliterate vehicle tracks. That superposition and the very light tone of the material in the bounce mark suggest that the recent strong earthquake likely triggered the rockfall. Photo B bottom was taken in October 2017, three years later. Location [19.298894 S, 70.171937 W]

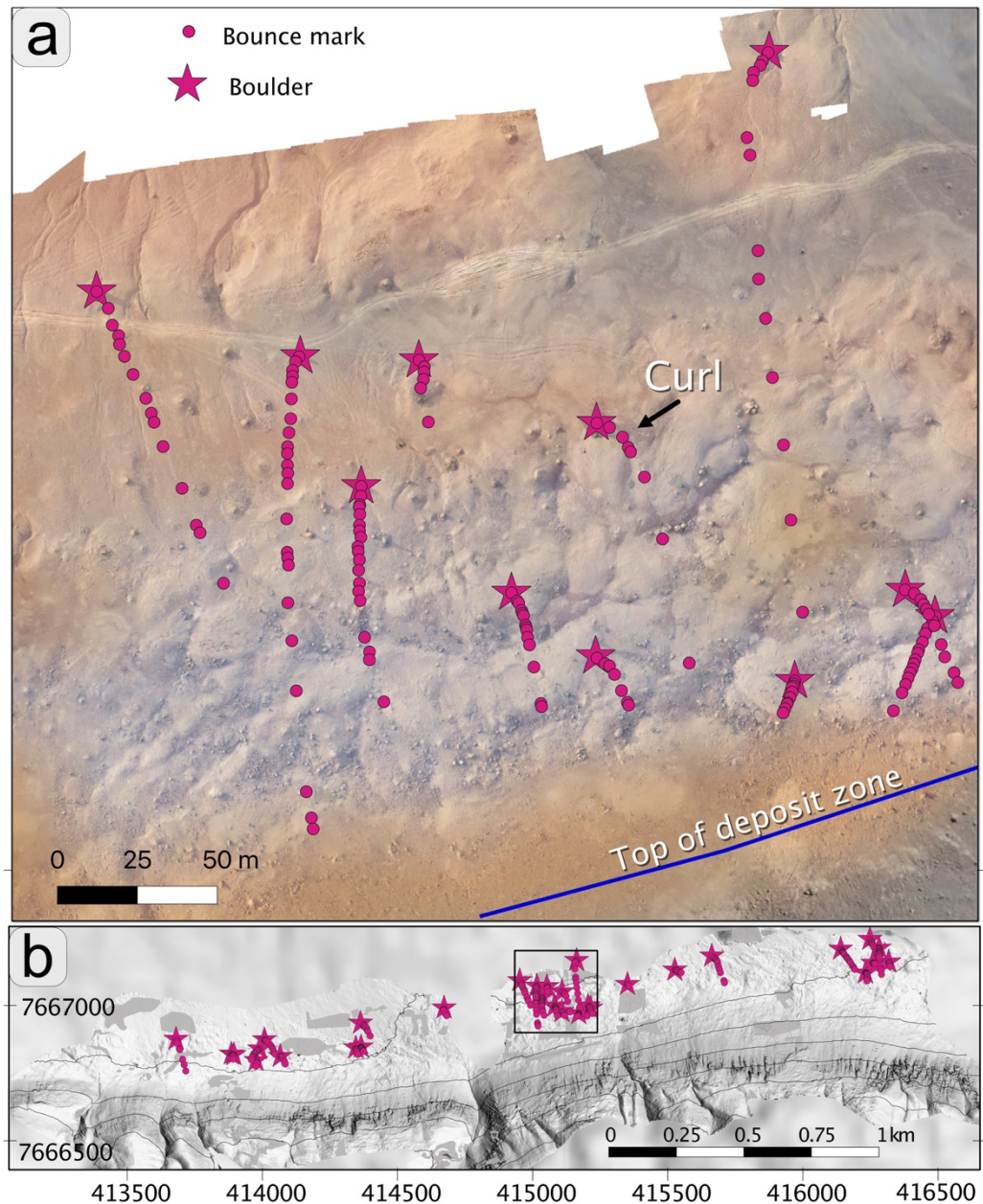


**Figure 8** Drone orthophoto mosaic of the sample region with the highest density of mapped boulder tracks, corresponding to the square in (b). (b) All 31 of the mapped boulder trails in the study area.

## 6. Analysis

### 6.1 Fall direction relative to slope

We calculate the boulder fall directions by fitting a line to the points corresponding to the mapped bounce marks (Fig. 8) and then finding the angle ( $\phi$ ) between this bounce mark line and the line of steepest slope. For the line of steepest slope, we use a line perpendicular to a smoothed contour line running through the deposit area. More than one quarter of the bounce mark directions deviate by more than 30 degrees from the line of steepest slope (Fig. 9).

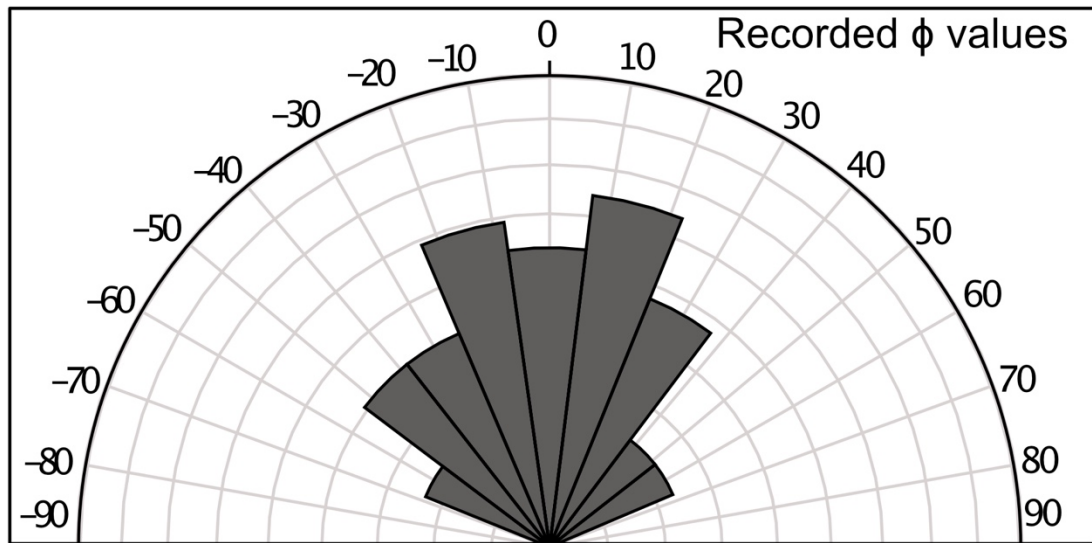


**Figure 9** A rose diagram depicting the actual measurements of the angle ( $\phi$ ) between the line following the trail of bounce marks and the line of steepest slope for the 31 mapped boulder trails. Bins are 15 degrees wide, area scaled, and centered on zero.

### 6.2 Bounce Kinematics and the Coefficient of Restitution

Our observations of discrete bounce marks for Chuculay, Atajaña, Pisagua, and coastal escarpment boulders show us that bouncing is an important mechanism of boulder travel, and

these observations can help us gain insight into the process of a rock bounce. In an attempt to quantify the bounces, we back calculate the coefficient of restitution (COR) for each bounce (Eq. 1). COR is often broken up into the normal and tangential components (Fig. 9,  $v_{i,n}$  and  $v_{i,t}$ , respectively), though in our calculations we will also focus on the “total velocity COR” or  $COR_v$ . The phrase “COR values” may refer to any of the components ( $COR_N$ ,  $COR_T$ , or the total  $COR_v$ )

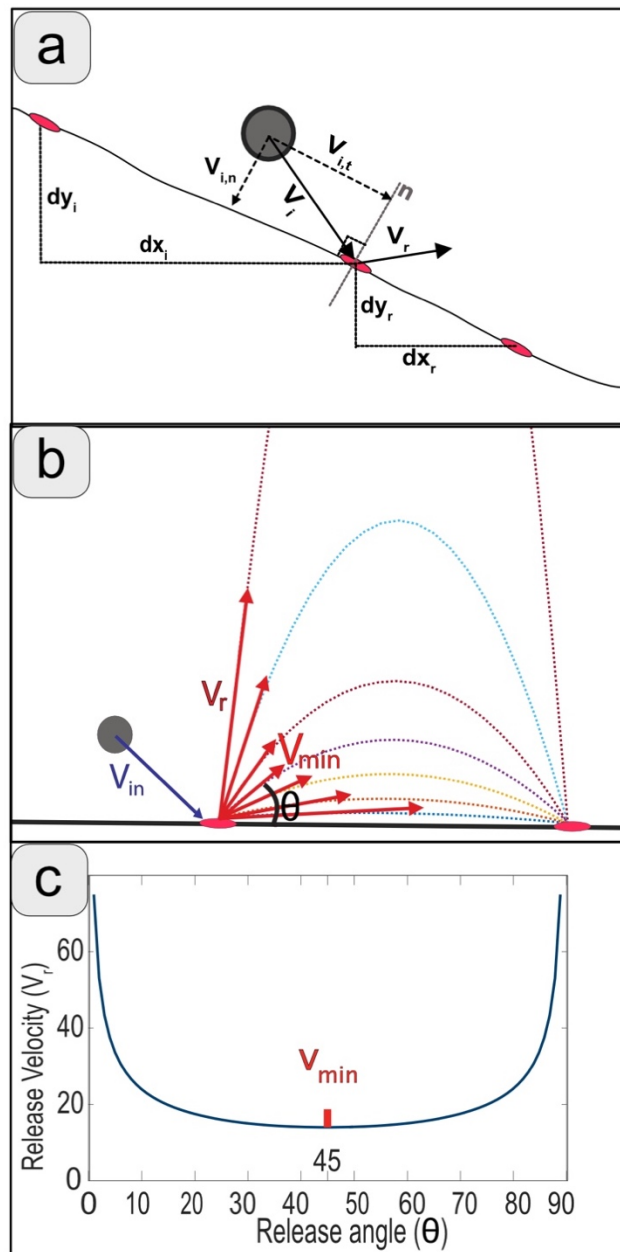


**Figure 10** a) Schematic illustrating the variables used to define the coefficient of restitution. Grey circle refers to the falling rock, pink ovals refer to bounce marks, and arrows with solid lines represent the trajectory of the falling rock. b) Schematic illustrating the possible trajectories (dashed lines) defined by different release velocities (red arrows) at corresponding release angles (theta) a rock may have flown along between two bounce marks. c) Each point on the graph represents one possible trajectory connecting 2 locations defined by a release speed and release angle. This plot is for trajectories connecting a starting and ending position 20 m apart, with no vertical change between them.

In order to back calculate the COR values from the observed bounce marks, we follow the methods of Saroglou et al. (2018). The required assumptions include, first, that the boulder follows a ballistic trajectory through the air from one bounce mark to the next. Second, because the solution for the rock's trajectory between impact points is non-unique due to a trade-off between release speed and release angle (Fig 10 b-c), we assume that the rock follows the path corresponding to the trajectory that requires the minimum release velocity ( $V_{\min}$ ). This minimum release velocity assumption is not a trivial assumption.

Our hypothetical  $COR_V$  results show a large range (Fig. 11a), from 0.24 up to 4.2, with many (58%) estimated  $COR_V$  values greater than one (Fig. 11). The normal ( $COR_N$ ) and tangential ( $COR_T$ ) components of the coefficient of restitution also show a wide range in values (Fig. 11b,d), though because they are even more affected by the assumed release angle, we will continue focusing on the  $COR_V$  values. Due to the minimum velocity assumption, hypothetical airborne velocities are essentially determined by the distance between bounce marks, resulting in the strong relationship between  $COR_V$  and the ratio between the downhill bounce distance and the uphill bounce distance, or  $dx_{\text{diff}}$  (EQ 2),

$$dx_{\text{diff}} = dx_r/dx_i \quad (2)$$

where  $dx_r$  and  $dx_i$  are defined in Fig. 10a. In almost all bounces where the  $dx_{\text{diff}}$  is greater than one, so is the estimated  $COR_V$  value (Fig. 11c).

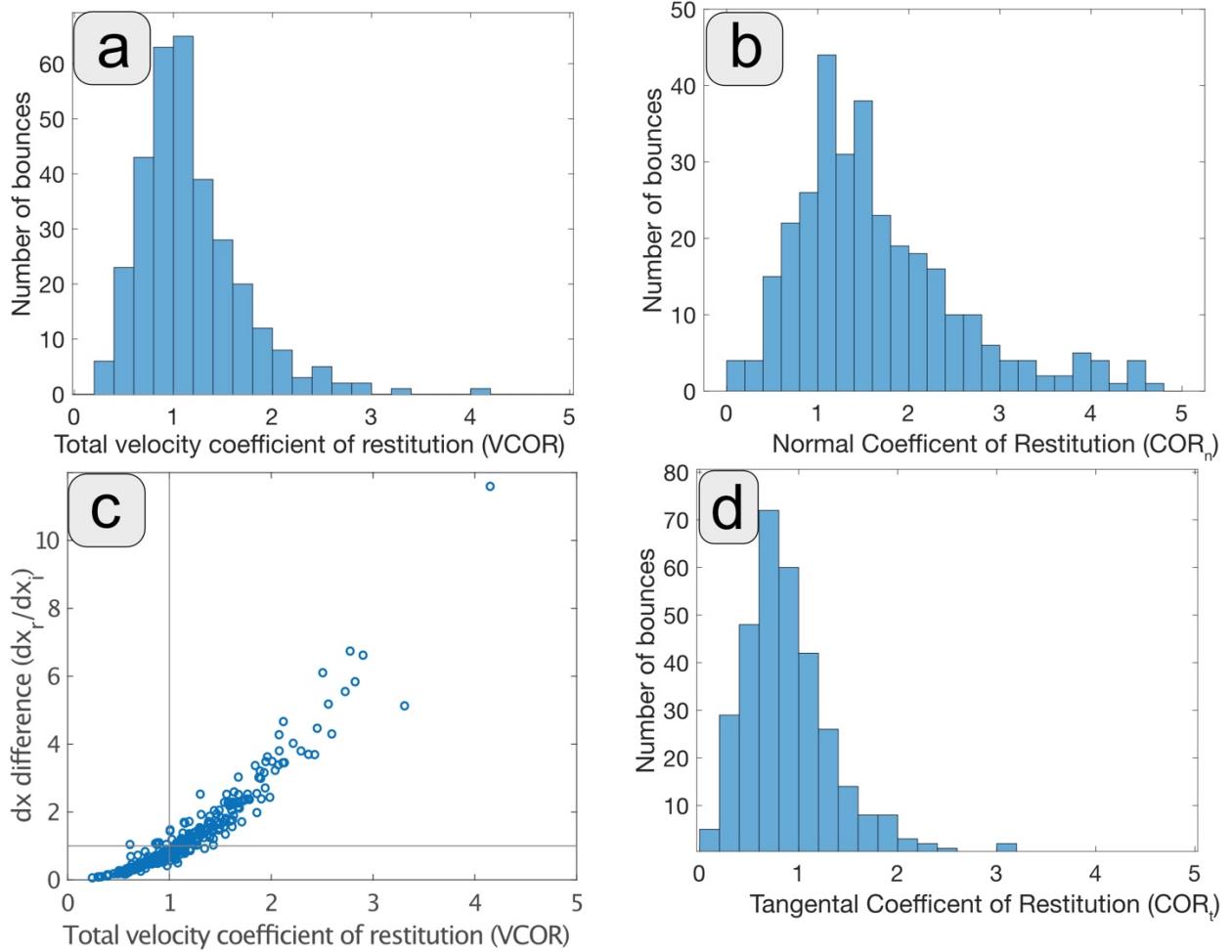


**Figure 11** a) histogram of the calculated hypothetical total velocity coefficient of restitution for each of the 321 individual bounces. b) and d) histograms of the normal and tangential components of the COR, respectively. c) Calculated  $dx_{\text{diff}}$  values for each bounce plotted vs hypothetical  $COR_V$  (total Velocity Coefficient of Restitution) values of the same bounce, showing strong relationship between the two.

Estimated  $COR_V$  values greater than one do not mean that the boulders violate the laws of motion and gain energy (Federica Ferrari, Giani, & Apuani, 2013; Louge & Adams, 2002). A

combination of factors could lead to estimated COR or COR<sub>V</sub> values greater than one. First, the minimum velocity assumption, that for each bounce the rock flies with the minimum velocity required for it to make it to the next impact point, is likely not realistic for many bounces. Though an assumption is necessary to constrain the kinematic equations, it is not likely that falling boulders change speeds to match the most efficient trajectories for each bounce. For example, if a long bounce is followed by a short bounce, the boulder likely does not ‘slow’ down to fly the short distance along an efficient trajectory. Rather, the boulder likely keeps the faster velocity and flies at a much lower angle than the minimum velocity assumption would predict. Flat, low flying jumps were commonly observed in experiments (Bourrier, Berger, Tardif, Dorren, & Hungr, 2012; Caviezel et al., 2019).

Second, laboratory and field experiments recorded normal component coefficient of restitution (COR<sub>n</sub>) values greater than one (Federica Ferrari et al., 2013; Louge & Adams, 2002). While these studies do not mention the total velocity coefficient of restitution, they do illustrate that COR values are kinematic and not energetic, and thus values greater than one do not prove that the boulder created energy. Through well constrained field experiments filming rockfalls, and marking their bounce locations, Caviezel et al. (2019) initially found what appeared to be a kinematic energy increase at select bounces. However, when the impact point parameter was expanded to include the entire scar extent, rather than its central point, kinetic energy was found to stay constant, or decrease.

Also, this calculation only uses translational velocities and completely neglects boulder spin and angular momentum which are observed in all experiments of boulders bouncing down slopes. For example, rotational energy could be transferred into translational energy during a bounce. In addition to spin missing from the calculation, the rock could lose mass, or small slope

variations could promote inefficient trajectories. While our hypothetical COR calculations rely on many simplifications and assumptions, and thus may not result in the actual COR values, the calculation are based on measured parameters so they provide some real insights into the bounces.

### 6.3 Boulder distribution

Although, overall, boulder density diminishes with distance from the base of the transport zone, the proportion of the boulders that are large increases with distance from the scarp (Fig. 12a). This relationship would be exaggerated more if one includes the boulders under 2 m in diameter, which are not included in this analysis due to inadequate imagery resolution and time constraints. However, the greater number of small boulders (< 2 m) near the scarp front is visible in Figure A5-1b. It is possible that this increase in size further away from the scarp may reflect that larger boulders make it to the deposit zone with more momentum and thus are able to bounce further across the gently inclined zone. An alternative hypothesis is that the larger a boulder is as it descends across the transport zone and into the deposit zone, the more difficult it is for stationary boulders to slow down via impacts. The size-distance relationship is complicated by relative ages. For example, a hypothetical class 1 rock cube 1 m on each side would have a volume of  $1\text{m}^3$  and a surface footprint of  $1\text{m}^2$ , but if that rock decayed without losing volume into a class 3 cone with 1 m height, the new surface footprint would be  $3\text{ m}^2$ . This means that older rocks have a larger surface footprint, so a relationship involving surface footprints would be affected by both the initial volume and the age of the boulders.

Relatively more morphologically old boulders occur further away from the scarp front (Fig. 12b). The peak concentration for class 1 boulders is at the scarp front, for class 2 the maximum is 50-75 m from the scarp front, and class 3 it is 125-150 m from the scarp front.

Three hypotheses exist that may explain why there are more morphologically older boulders observed further away from the scarp. One possibility is that the number of class 3 boulders is actually constant regardless of distance from the scarp, yet that the ones closer to the base of the scarp were buried by younger rock falls and other slope processes. This is supported by the decrease in elevation away from the toe of the transport zone, which implies that the net rate of deposition decreases with distance from the source area. Another hypothesis is that most of the class 3 boulders whose evidence remains are the larger boulders, and those boulders went further than the average boulder. If so, the bias in age towards the far parts of the scarp reflects a bias in boulder size. Another, less likely but more interesting, hypothesis is that the old boulders far away from the scarp front represent the last remnants of a boulder field that formed when the source zone and transport zone parts of the scarp were either further forward (northward), or higher. In this case, the majority of the class 1 boulder falls represent the subsequently eroded scarp.

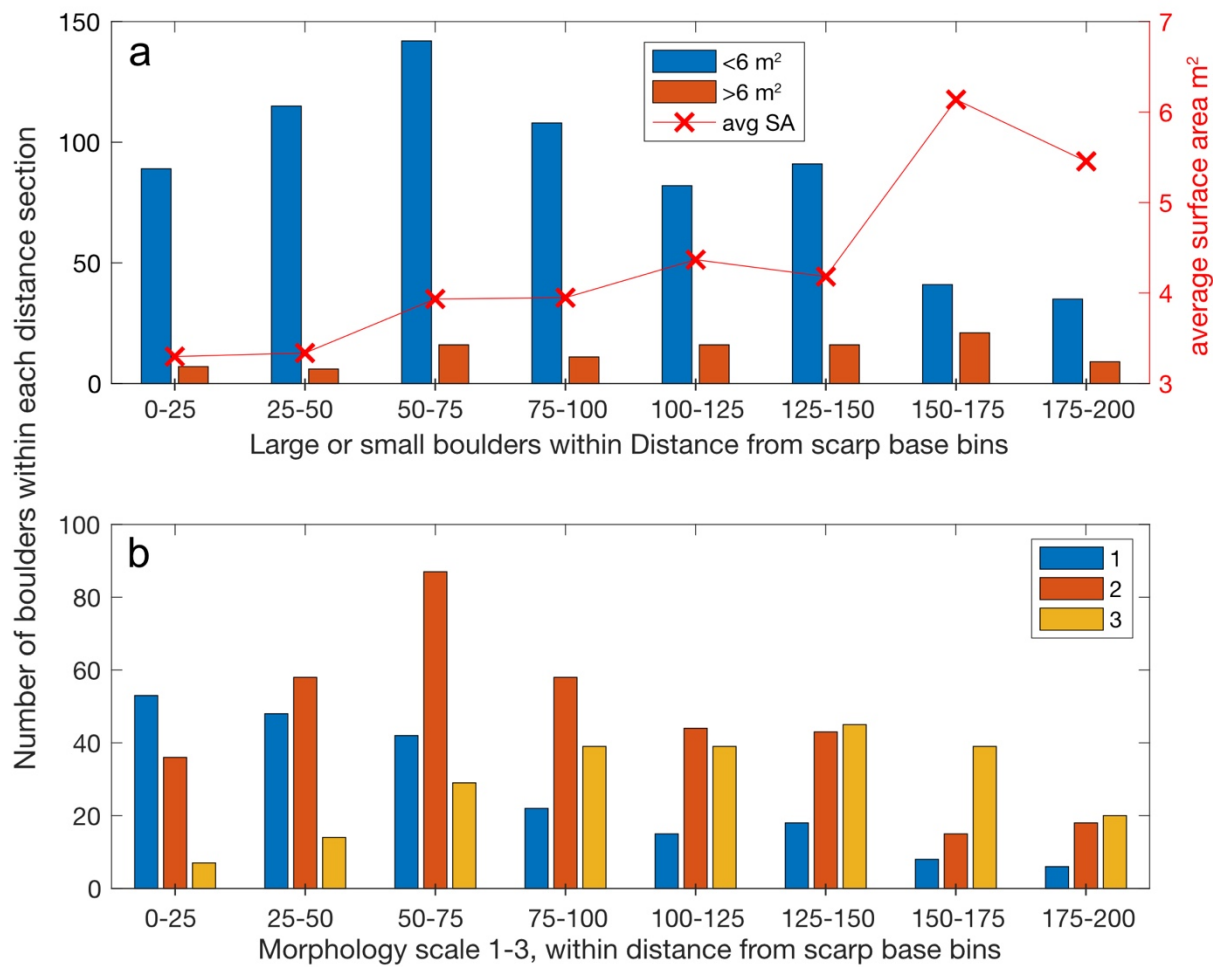


**Figure 12** A set of histograms displays the boulders identified on drone imagery in bins of distance from the scarp front. (a) Boulders classified based on their surface area. Note that the ‘smaller’ ( $< 6\text{m}^2$  surface area) boulders make up less of the proportion of total boulders further away from the scarp. Red X’s and right y-axis represent the average surface area for all boulders in that distance bin. (c) Boulders classified by their morphology (Fig. 6). Morphologically older boulders make up a higher proportion of the boulders at further distances from the scarp front.

#### 6.4 Boulder field density and scarp morphology

Working under the assumptions that the processes causing rockfalls are ongoing, and that the location of past rock falls can inform us about the process of past and future rockfalls, we

compare the density of boulders within the deposit zone to the morphology of the source zone, to learn where rockfalls may occur most commonly.

Morphologic metrics can describe and quantify the topography of the source zone, including elevation, slope, roughness, and slope independent roughness. We performed all of our morphometric calculations using our drone-based DEM down-sampled to 1 by 1 m cells. The slope calculation we used takes into account the height of the neighboring 8 DEM cells to calculate the slope at one DEM cell (GDAL contributors 2020). The roughness metric we use (Wilson et al., 2007, GDAL contributors 2020) records the largest elevation difference between the neighboring cells. However, this roughness is dependent on slope, because a tilted smooth plane would register a roughness value recording the slope in the difference between the lower cells and higher cells. To calculate roughness mostly independent of slope, we first removed the long wavelength elevation changes from the DEM. We down-sampled the 1m DEM into a 10 m DEM (using cubic interpolation), and then subtracted the 10 m DEM elevations from our 1 m DEM values, thus removing the signal from long wavelength slopes and leaving only the local (< 10 m) topography, essentially high pass filtering the topography. We then calculated the roughness on this filtered DEM (Background in Fig. 13).

In the boulder deposit zone at the base of the escarpment, we used our set of manually traced boulders whose diameters exceed 2m to find a rough estimation of the density of fallen boulders. For the boulder density map, we created a heatmap of the fallen boulders using a 50 m radius (Fig. 13, white to blue tones).

The map shows a moderately good relationship between the meter scale roughness of the exposed bedrock in the source zone and the density of boulders currently sitting down-slope of that stretch of bedrock (Fig. 13a). A comparison among swath profiles of the boulder density,

slope, and roughness (Fig. 13b-d) (see appendix A5 for details on the swath profiles) demonstrates that slope and roughness each roughly matches the boulder density profile and that, despite removing the slope from our roughness calculation, the swath profile mean slope and mean slope independent roughness follow similar trends.

This relationship is especially notable in the western half of the transects, where a transition from nearly no boulders to many boulders at the base of the scarp is mirrored by an increase in the roughness and slope of the source area (Fig. 13b-d). The roughness metric mirrors this increase remarkably well, matching each spike in boulder density. In the eastern half of the area, correlations are less straightforward, and similarly loosely fit by both roughness and slope. Two factors appear to contribute to the lower degree of correspondence in the eastern zone than in the western zone. First, because of scarp curvature, an X value along the deposit zone profile may not be directly down-slope from that X values along source profile (Fig. A5-1). There is greater curvature of the fault scarp in the east than in the west. Second, and perhaps more importantly, along-strike changes in boulder density are less pronounced in the East.

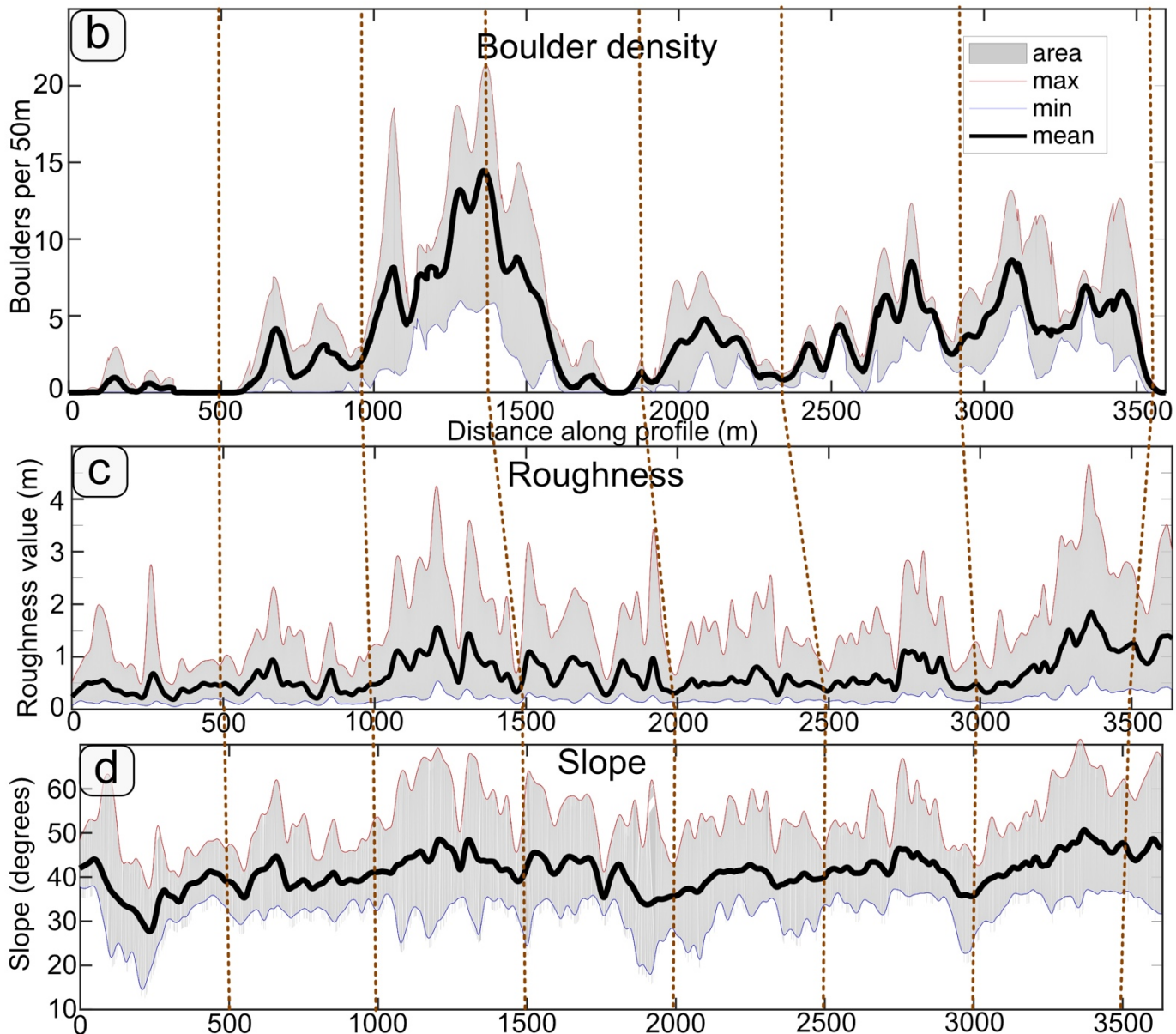
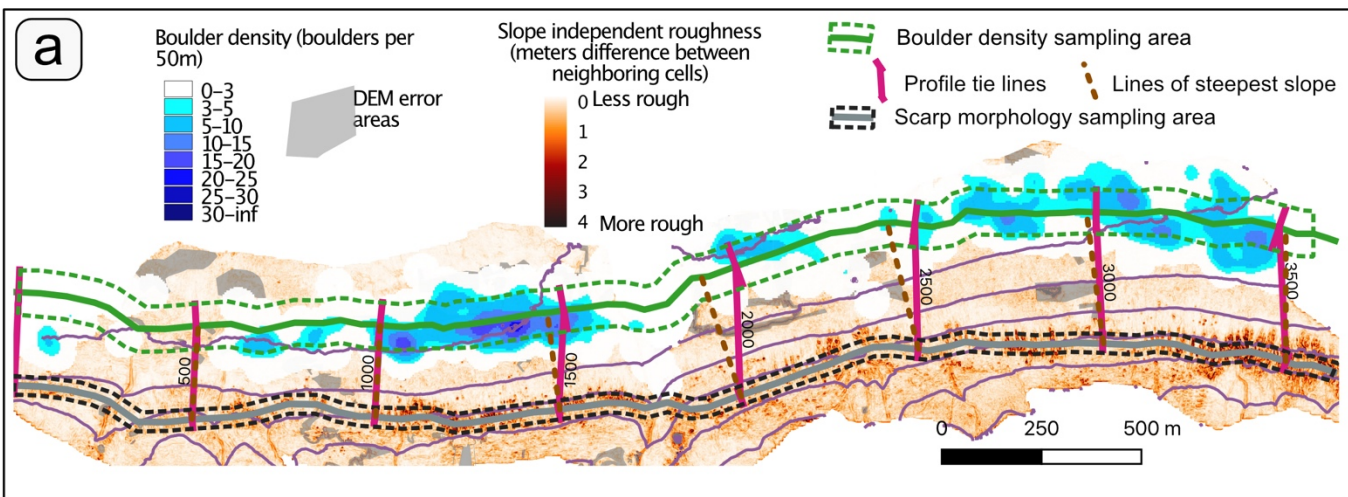


**Figure 13** a) Comparison of boulder fall density to the roughness of the escarpment. Background red to white color scale image represents the slope independent roughness value of

the 1-m drone-based DEM. Blue to white color gradients represent the number of manually traced boulders within a 50 m radius within the deposit zone. Purple lines are 50 m contour lines. Green solid and dashed lines show data sample area for the boulder density swath profile plot, and grey solid line with black dashed lines show the sample area for the source area swath profile plots. Magenta profile tie lines show points with the same X value in both the source area and deposit area profiles, while the brown dashed lines of steepest slope show what points lie directly downhill from those x values on the source zone profile. Note that one x value on the source area profile line does not necessarily lie directly uphill from location with the same x value along the deposit zone profile line. b) boulder density data extracted from within the green dashed area along the deposit zone in (a). Thick black line is the mean of the data points extracted along each perpendicular cross-profile line to the along scarp profile line, while the red upper bound represents the highest value and the blue lower bound represents the lowest value along each cross-profile line. c) The slope independent roughness metric discussed in section 6.4 . d) is slope data from the 1 m drone DEM. The Data in c and d are filtered with a 50 m window butterworth filter. Brown dashed lines across b-d represent comparison lines following the line of steepest slope from the source profile to the deposit profile

## **7 Discussion**

### **7.1 Fall trigger mechanism**

Major triggering mechanisms for rockfalls in general are: precipitation events, frost-thaw activity, thermal weathering, and seismic activity (Dorren, 2003). Although light frosts can occur in this part of the Atacama, frozen ground is unknown both due to lack of sustained low temperatures at 21°S and lack of significant soil moisture. Thermal stressing is a common trigger for rockfalls generated through exfoliation fractures (Collins & Stock, 2016). In the Atacama average daily temperature swings are around  $\pm 5\text{K}$  (Schween et al., 2020), and while we do not observe exfoliation fractures in the bedrock, thermal expansion of salts observed in fractures may be important (Amit, Gerson, & Yaalon, 1993). While precipitation is very rare in this region (Schween et al., 2020), when it does occur the results can be catastrophic. Debris flow deposits, alluvial fans, and channels in the escarpment all evince infrequent precipitation events (May et al., 2020).

In this area, earthquakes present one of the most likely triggers for rock falls. The northern Chile Coastal Cordillera (20°S-22°S) is affected by great earthquakes on the plate boundary about every 150 years (Comte & Pardo, 1991). Furthermore, unusually active crustal seismicity directly underlies the Chuculay escarpment (Sippl et al., 2018). Three months after the 2014 Pisagua  $M_w$  8.1 earthquake, the authors observed a freshly fallen boulder along the Atajaña fault scarp about 100 km from the epicenter (Fig. 7). This very freshly fallen boulder most likely fell during the shaking, but was the only newly fallen boulder observed along the 20 km fault scarp following the earthquake. Also, while the authors were camped at the Atajaña scarp, a  $M_w$  6.1 occurred 90 km away, and bounce tracks that had not been noticed earlier were observed on

the slope the following day. There are also reports of seismically triggered rock falls during the 2007 Tocopilla earthquake, received from the residents near Caleta Punta Arenas, and the 2005 Tarapacá earthquake (Marquardt et al., 2006).

Using our loose age constraints, we can make a back of the envelope calculation of the rate of boulder falls. At Chuculay, all of the boulders fell after the deposition of the underlying ash deposits which range from 0.3 to 1.4 Ma (Carrizo et al. 2008; Vásquez et al., 2018). In our 3 km section we observed  $840 > 2$  m diameter boulders. If those 840 boulders fell over the last 1.4 Ma, this gives a boulder fall rate of only 1 boulder every  $\sim 1,600$  years. If we assumed the youngest ash age of 300 ka, or an age comparable to layers recording local hillslope activity of  $\sim 120$  ka (May et al., 2020), the boulder fall rate increases to 1 every  $\sim 350$  or  $\sim 150$  years, respectively. These data and age constraints imply that large boulders fall at the rate of 1 per every hundred to few hundred years, or if many boulders fall at the same time, several boulders every thousand years. Small boulders (0.25-2 m diameter) are not fully represented in our data, and might fall more frequently. For example, along one 50 m wide swath perpendicular to the Chinchilla scarp we found only 16 2 m boulders (in our primary dataset) and 364 boulders with the short axis longer than 0.4 m (Appendix Fig. A5-1), if we extrapolate this discrepancy along the 3 km study area, the 1 large boulder per 350 years fall rate becomes 1 any size boulder per  $\sim 13$  years. However due to the small size of these additional boulders we cannot be sure that they were emplaced via rockfall.

This slow rate would not be surprising if the boulders were predominantly related to crustal earthquakes which tend to have recurrence intervals of thousands of years (Cortés A. et al., 2012). Great earthquakes on the plate boundary occur every 150-300 years (Comte & Pardo, 1991), but the megathrust is around 50 km deep where it passes under Chuculay (Hayes, Wald,

& Johnson, 2012) and thus deeper than the many nearby crustal faults (Allmendinger & González, 2010). The EW scarps which commonly exhibit boulder fields are oriented approximately parallel to the travel of seismic surface waves from the interplate earthquakes and at high angles to crustal earthquake seismic wave propagation. Nearly 200 years ago, Charles Darwin showed that stone walls parallel to seismic wave travel remained standing whereas those perpendicular to propagation were toppled in Concepción, Chile, following the devastating 1835 great earthquake (Darwin, 1845).

We suspect that rare precipitation events and earthquakes are the primary triggers for boulder falls in the Atacama, and that crustal earthquakes may be more important at Chuculay.

## 7.2 The rock fall

The rockfall sourced boulder fields provide two key pieces of data bearing on the process of the rockfalls: the rock's final position and, in more recent cases, the bounce marks that they left during their descent. Our area provides a time-integrated view of rock fall processes, offering complementary data to the dynamic parameters captured in experiments that document rock fall on camera or 4D structure from motion (Caviezel et al., 2019; Dorren, Berger, & Putters, 2006; Volkwein et al., 2018). Furthermore, this study evaluates rockfalls in a desert environment, whereas most rockfall observation studies took place in alpine mountain environments.

Perhaps most surprising, many of the boulders do not fall straight downhill (Fig. 9). We saw that lines fit to the bounce tracks describe a descent path that is an angle ( $\phi$ ) greater than 30 degrees from the gravitational fall line 25% of the time. Except for the finishing curl, the tracks are fairly straight. Two hypotheses may explain why the boulders fall oblique to slope. The first hypothesis is that their trajectories begin oblique to the slope. Perhaps the boulders topple off one of the source area bedrock 'fingers' falling perpendicular to the greater slope (Fig. 1 top center),

and thus begin their trajectories obliquely and never recover. This resistance to further changes in direction to match the slope over which they travel may be due to the angular momentum of the irregularly shaped boulders. A second hypothesis is that the boulders changed direction mid slope. We observe only around 15% of the bounce sequences revealing direction changes in the deposit zone, usually as the result of an impact with another boulder or topographic change. In the transport zone, where the surface is relatively smooth and there are few obstacles, the main cause for a direction change would be the irregular shape of the boulder. However, due to a lack of bounce mark preservation in the transport zone, we cannot confirm this. Our observations confirm the importance of accounting for the possible oblique fall of a boulder from its source, especially on slopes with linear trends.

A curl at the end of the boulder trajectories is visible in 18 of the 31 tracks at Chuculay. It may signal that the boulder was spinning about a short axis and, when the momentum slowed, the boulder fell to the side, like a rolling coin falling over as it loses momentum. This may signal that the bounce marks at the end of the boulder paths may actually be recording a process more akin to rolling than bouncing, even though the pits which define the tracks appear discrete or only slightly connected.

### 7.3 The bounces

In our calculations that used the rock bounce marks, we observed a wide distribution in the spacing between bounce marks and therefore also saw a spread in our calculated hypothetical coefficient of restitution values (Fig. 11) including many values which are greater than one. Though the assumptions necessary to calculate our hypothetical coefficient of restitution may not be entirely realistic (section 5.2), the spread in COR values and  $dx_{diff}$  values do illustrate that the bounce marks are spaced irregularly. For this to be true, the amount of energy absorbed by the

ground must not be constant, so the actual COR values must not be constant. While some, mostly older, popular rockfall modelling software uses constant values for the restitutions of coefficients (Lan, Derek Martin, & Lim, 2007; Li & Lan, 2015; Pfeiffer & Higgins, 1990), the variation we observe matches experimental data (Bourrier et al., 2012; Caviezel et al., 2019; Dorren et al., 2006). Variations of the coefficients of restitutions can be attributed to shape of the rock, variability in the rebounding surface, variable spin of the rock, and even angle of the impact. Further tests into what may control calculated COR values are presented in appendix 6. However, our observations limited to only mapped bounce mark locations, do not indicate which factors play a larger role in accounting for the variability in the bounce mark spacing.

#### **7.4 After a boulder has landed**

Once the falling boulder has come to rest, there is no evidence that it continues to move. If, after the initial rapid fall and descent, individual boulders continued to creep over the surface, one would observe a trail of small debris rather than circular skirts of debris about the boulders that we do observe. This is in contrast to the other type of boulder fields in the Atacama, which appear to creep, likely during earthquakes, to collect in depressions (Matmon et al., 2015; Quade et al., 2012; Sager et al., 2020). The boulders in our study area are generally brecciated and/or fractured and not coherent monolithic blocks, which means that they weather by shedding layers and clasts. The preexisting fractures in the rock are likely a major reason that we observe debris skirts and continuing degradation. This is in contrast to the exceptionally old monolithic granitic boulders documented elsewhere in the Atacama (Matmon et al., 2015; Placzek et al., 2014).

In the absence of frost and vegetation, the likely mechanisms for weathering of the boulders into debris skirts are thermal changes, abrasion from wind-blown sediment, and salt wedging. Goudie et al. (2002) found that the combination of fog and salt availability controlled

the rate and timing of rock breakdown in experiments simulating the climate in the northern Atacama Desert. While the fog is stronger and more consistent closer to the coast (Schween et al., 2020), we did observe the Camanchaca (fog) at Chuculay.

We consider the morphology classification we created to be a nonlinear proxy for age of the boulder. Of course, the size and cohesive strength of each individual boulder likely affects how the morphology classification relates to absolute age. For example, weathering processes may only act on the surface of a boulder, thus larger boulders with lower surface area to total mass or volume ratios may take longer to weather to the point of being buried in their own debris aprons. We also expect that a stronger, more cohesive, boulder would weather more slowly towards class 3. Given the lithologic similarity of much of the boulder population at Chuculay, we suspect that the variance in cohesive strength does not outweigh the size of the boulder when determining the progression from class 1 to class 2.

The rate of degradation remains poorly constrained. At Chuculay, the oldest boulders must have fallen after the deposition of the underlying ash deposits which range from 0.3 to 1.4 Ma (Carrizo et al. 2008; Vásquez et al., 2018). Thus, the oldest boulders must not take longer than 0.3 to 1.4 Ma to degrade. At Caleta Punta Arenas (Fig. 2), similar boulder fields with similar degrees of degradation lie atop an uplifted marine abrasion platform which, at 25-50 m elevation, is lower than the regional 100 m high terrace thought to be about  $400\pm100$  ka (Regard et al., 2010). Though environmentally different, again the oldest boulders likely are not older than hundreds of thousands of years. Our constraints on how young a degraded boulder can be are also quite loose. Our observations made over the course of 3 years (Fig. 7), and word of mouth evidence from residents near Caleta Punta Arenas that a class 1 boulder fell during the 2007 Tocopilla earthquake, show that degradation does not occur on the decadal timescale. In contrast,

at the Pisagua fault scarp (~160 km North of Chuculay), we observed small (< 0.5 m diameter) class 3 boulders, whose falls we believe were related to railroad construction. Historical context for the railroad suggests that the rock falls were likely on the order of 100 years prior to observation, and hence that small boulders transformed into class 3 mounds by decadal-scale weathering. At Chuculay, local hillslope processes, including slumping of fine grained material, which have been active during the last tens of thousands of years (May et al., 2020; Medialdea et al., 2020) may be contemporary with boulder degradation. In summary, small and weak boulders may degrade within a century, while large more coherent or well cemented boulders may take tens of thousands of years, if not longer.

## 7.5 Spatial variation of boulder falls

The boulder fields represent thousands of individual rock falls. The variation of the locations of the fallen rocks hints at where to expect rock falls in general. The relative densities of fallen boulders at the base of the scarp can be compared with the morphology of the source area. If we assume that the density of boulders at the base of the slope represents ongoing processes that will continue, it follows that new boulders are more likely to fall where we have measured the highest density of older boulders.

Presumably, higher roughness and higher slopes in the source area correlate with decreased slope stability and boulder stability. Other authors have observed the correlation between roughness and rockfalls when searching for ways to estimate likelihood of future rockfalls (Dunham et al., 2017; Marquinez et al., 2003). While we observed this roughness metric to rockfall correlation; in order to determine a predictive relationship, one would need to assess the nature of the outcrop, joint spacing, rock strength, vegetation, and other factors.

## **8. Conclusions**

The boulder fields in the Coastal Cordillera of the hyperarid central Atacama Desert record time-integrated histories of Pleistocene and Holocene rock falls. The boulder field along the east-trending Chinchilla fault scarp in the Chuculay fault system reveals (a) that rougher scarp morphology and to a lesser extent steeper slopes corresponds to a higher density of boulder falls; (b) that the boulders fall as individuals and bounce rather than roll or slide to their place of deposition; and (c) that boulder degradation advances while conserving the debris in situ.

Boulder falls triggered by earthquake shaking have been well documented but release of boulders from the source area may also, in some cases, be triggered by rare precipitation events. The boulders documented here differ from the Atacama Desert boulder fields previously described in the literature (Matmon et al., 2015; Quade et al., 2012; Sager et al., 2020) by their evidence for rapid, bouncing descent and subsequent weathering in place with no additional movement.

Our results have implication for rock fall hazard assessment and for the software packages that have been prepared by and for geotechnical engineers tasked with that hazard evaluation. Especially germane in that regard are our results highlighting the irregular bounce mark spacing, the significant deviations from the slope fall line, and general correlation with source area roughness. We show that estimated coefficients of restitution (COR), a common parameter in rockfall modeling software, may significantly exceed a value of 1 and are not likely constant. The COR values are influenced by several factors such as angular momentum of the boulder, stochastic variability of the impact process and boulder shape, and the possibility of loss of boulder mass during transport. We also show that boulders often fall along a path that does not

follow the path of steepest slope, which highlights the importance of using 3D models that may allow for this fall obliquity over 2D models where the fall path is predetermined.

Rather than providing a complete picture of the physics of a single boulder fall, the boulder fields of the Atacama provide evidence of the long-term average behavior of boulder falls from steep slopes. Within the uncertainty limits of the age constraints, the long-term time averaged rate of fall for large boulders (>2 m) along the Chinchilla scarp is surprisingly low, on the order of one every few hundred years.

Future studies of the boulders may be able to offer further insights into particular rockfall processes and physics. One might even be able to use the degradation boulder morphology as a proxy for age to gain insights on the timing of the fall triggers, and the surface process rates acting on the escarpment as a whole.

## REFERENCES

- Allmendinger, R. W., & González, G. (2010). Invited review paper: Neogene to Quaternary tectonics of the coastal Cordillera, northern Chile. *Tectonophysics*, 495(1–2), 93–110. <https://doi.org/10.1016/j.tecto.2009.04.019>
- Allmendinger, R. W., González, G., Yu, J., Hoke, G., & Isacks, B. (2005). Trench-parallel shortening in the Northern Chilean Forearc : Tectonic and climatic implications, (1), 89–104. <https://doi.org/10.1130/B25505.1>
- Amit, R., Gerson, R., & Yaalon, D. H. (1993). Stages and rate of the gravel shattering process by salts in desert Reg soils. *Geoderma*, 57(3), 295–324. [https://doi.org/10.1016/0016-7061\(93\)90011-9](https://doi.org/10.1016/0016-7061(93)90011-9)
- Amundson, R., Dietrich, W., Bellugi, D., Ewing, S., Nishiizumi, K., Chong, G., ... Caffee, M. (2012). Geomorphologic evidence for the late Pliocene onset of hyperaridity in the Atacama Desert. *Bulletin of the Geological Society of America*, 124(7–8), 1048–1070. <https://doi.org/10.1130/B30445.1>
- Berti, M., Corsini, A., & Daehne, A. (2013). Comparative analysis of surface roughness algorithms for the identification of active landslides. *Geomorphology*, 182, 1–18. <https://doi.org/10.1016/j.geomorph.2012.10.022>
- Bourrier, F., Berger, F., Tardif, P., Dorren, L., & Hungr, O. (2012). Rockfall rebound: Comparison of detailed field experiments and alternative modelling approaches. *Earth Surface Processes and Landforms*, 37(6), 656–665. <https://doi.org/10.1002/esp.3202>
- Carrizo, D., González, G., & Dunal, T. (2008). Constricción neógena en la Cordillera de la Costa, norte de Chile: Neotectónica y datación de superficies con  $^{21}\text{Ne}$  cosmogónico. *Revista Geologica de Chile*, 35(1), 1–38. <https://doi.org/10.4067/s0716-02082008000100001>
- Caviezel, A., Demmel, S. E., Ringenbach, A., Bühler, Y., Lu, G., Christen, M., ... Bartelt, P. (2019). Reconstruction of four-dimensional rockfall trajectories using remote sensing and rock-based accelerometers and gyroscopes. *Earth Surface Dynamics*, 7(1), 199–210. <https://doi.org/10.5194/esurf-7-199-2019>
- Collins, B. D., & Stock, G. M. (2016). Rockfall triggering by cyclic thermal stressing of exfoliation fractures. *Nature Geoscience*, 9(5), 395–400. <https://doi.org/10.1038/ngeo2686>
- Comte, D., & Pardo, M. (1991). Reappraisal of great historical earthquakes in the northern Chile and southern Peru seismic gaps. *Natural Hazards*, 4(1), 23–44. <https://doi.org/10.1007/BF00126557>
- Cortés A., J., González L., G., Binnie, S. A., Robinson, R., Freeman, S. P. H. T., & Vargas E., G. (2012). Paleoseismology of the mejillones fault, northern Chile: Insights from cosmogenic  $^{10}\text{Be}$  and optically stimulated luminescence determinations. *Tectonics*, 31(2), 1–21. <https://doi.org/10.1029/2011TC002877>
- Darwin, C. (1845), Journal of Researches Into the Natural History and Ge- ology of the Countries Visited during the Voyage of H.M.S. ‘Beagle’ Round the World: Under the Command of Capt. Fitzroy, 2nd ed., Corrected with Additions, John Murray, London.
- Davis,Dorren, L K A, Berger, F., & Putters, U. S. (2006). *Real-size experiments and 3-D simulation of rockfall on forested and non-forested slopes*. *Natural Hazards and Earth System Sciences* (Vol. 6). Retrieved from <https://www.nat-hazards-earth-syst-sci.net/6/145/2006/nhess-6-145-2006.pdf>
- Dorren, Luuk K.A. (2003). A review of rockfall mechanics and modelling approaches. *Progress in Physical Geography: Earth and Environment*, 27(1), 69–87.

- <https://doi.org/10.1191/0309133303pp359ra>
- Dunham, L., Wartman, J., Olsen, M. J., O'Banion, M., & Cunningham, K. (2017). Rockfall Activity Index (RAI): A lidar-derived, morphology-based method for hazard assessment. *Engineering Geology*, 221, 184–192. <https://doi.org/10.1016/j.enggeo.2017.03.009>
- Ewing, S. A., Sutter, B., Owen, J., Nishiizumi, K., Sharp, W., Cliff, S. S., ... Amundson, R. (2006). A threshold in soil formation at Earth's arid-hyperarid transition. *Geochimica et Cosmochimica Acta*, 70(21), 5293–5322. <https://doi.org/10.1016/j.gca.2006.08.020>
- Fanos, A. M., & Pradhan, B. (2018). Laser Scanning Systems and Techniques in Rockfall Source Identification and Risk Assessment: A Critical Review. *Earth Systems and Environment*, 2(2), 163–182. <https://doi.org/10.1007/s41748-018-0046-x>
- Ferrari, F., Giacomini, A., & Thoeni, K. (2016). Qualitative Rockfall Hazard Assessment: A Comprehensive Review of Current Practices. *Rock Mechanics and Rock Engineering*, 49(7), 2865–2922. <https://doi.org/10.1007/s00603-016-0918-z>
- Ferrari, Federica, Giani, G. P., & Apuani, T. (2013). Why can rockfall normal restitution coefficient be higher than one? *Rendiconti Online Societa Geologica Italiana*, 24, 122–124.
- Frattini, P., Crosta, G., Carrara, A., & Agliardi, F. (2008). Assessment of rockfall susceptibility by integrating statistical and physically-based approaches. *Geomorphology*, 94(3–4), 419–437. <https://doi.org/10.1016/j.geomorph.2006.10.037>
- González, G., Gerbault, M., Martinod, J., Cembrano, J., Carrizo, D., Allmendinger, R., & Espina, J. (2008). Crack formation on top of propagating reverse faults of the Chuculay Fault System, northern Chile: Insights from field data and numerical modelling. *Journal of Structural Geology*, 30(6), 791–808. <https://doi.org/10.1016/j.jsg.2008.02.008>
- Goudie, A. S., Wright, E., & Viles, H. A. (2002). The roles of salt (sodium nitrate) and fog in weathering: A laboratory simulation of conditions in the northern Atacama Desert, Chile. *Catena*, 48(4), 255–266. [https://doi.org/10.1016/S0341-8162\(02\)00028-0](https://doi.org/10.1016/S0341-8162(02)00028-0)
- Guzzetti, F., Crosta, G., Detti, R., & Agliardi, F. (2002). STONE: a computer program for the three-dimensional simulation of rock-falls. *Computers & Geosciences*, 28(9), 1079–1093. [https://doi.org/10.1016/S0098-3004\(02\)00025-0](https://doi.org/10.1016/S0098-3004(02)00025-0)
- Hayes, G. P., Wald, D. J., & Johnson, R. L. (2012). Slab1.0: A three-dimensional model of global subduction zone geometries. *Journal of Geophysical Research: Solid Earth*, 117(1), B01302. <https://doi.org/10.1029/2011JB008524>
- Houston, J. (2006). Variability of precipitation in the Atacama Desert: its causes and hydrological impact. *International Journal of Climatology*, 26(15), 2181–2198. <https://doi.org/10.1002/joc.1359>
- Jordan, T. E., Kirk-Lawlor, N. E., Nicolás Blanco, P., Rech, J. A., & Cosentino, N. J. (2014). Landscape modification in response to repeated onset of hyperarid paleoclimate states since 14 Ma, Atacama Desert, Chile. *Bulletin of the Geological Society of America*, 126(7–8), 1016–1046. <https://doi.org/10.1130/B30978.1>
- Kim, D. H., Gratchev, I., Berends, J., & Balasubramaniam, A. (2015). Calibration of restitution coefficients using rockfall simulations based on 3D photogrammetry model: a case study. *Natural Hazards*, 78(3), 1931–1946. <https://doi.org/10.1007/s11069-015-1811-x>
- LaHusen, S. R., Duvall, A. R., Booth, A. M., & Montgomery, D. R. (2016). Surface roughness dating of long-runout landslides near Oso, Washington (USA), reveals persistent postglacial hillslope instability. *Geology*, 44(2), 111–114. <https://doi.org/10.1130/G37267.1>
- Lan, H., Derek Martin, C., & Lim, C. H. (2007). RockFall analyst: A GIS extension for three-dimensional and spatially distributed rockfall hazard modeling. *Computers and*

- Geosciences*, 33(2), 262–279. <https://doi.org/10.1016/j.cageo.2006.05.013>
- Li, L., & Lan, H. (2015). Probabilistic modeling of rockfall trajectories: a review. *Bulletin of Engineering Geology and the Environment*, 74(4), 1163–1176.  
<https://doi.org/10.1007/s10064-015-0718-9>
- Louge, M. Y., & Adams, M. E. (2002). Anomalous behavior of normal kinematic restitution in the oblique impacts of a hard sphere on an elastoplastic plate. *Physical Review E - Statistical Physics, Plasmas, Fluids, and Related Interdisciplinary Topics*, 65(2), 6–11.  
<https://doi.org/10.1103/PhysRevE.65.021303>
- Lu, G., Caviezel, A., Christen, M., Demmel, S. E., Ringenbach, A., Bühler, Y., ... Bartelt, P. (2019). Modelling rockfall impact with scarring in compactable soils. *Landslides*, (July).  
<https://doi.org/10.1007/s10346-019-01238-z>
- Marquínez, J., Menéndez Duarte, R., Farias, P., & Jiménez Sánchez, M. (2003). Predictive GIS-based model of rockfall activity in mountain cliffs. *Natural Hazards*, 30(3), 341–360.  
<https://doi.org/10.1023/B:NHAZ.0000007170.21649.e1>
- Matmon, A., Quade, J., Placzek, C., Fink, D., Copeland, A., & Neilson, J. W. (2015). Seismic origin of the Atacama Desert boulder fields. *Geomorphology*, 231, 28–39.  
<https://doi.org/10.1016/j.geomorph.2014.11.008>
- May, S. M., Meine, L., Hoffmeister, D., Brill, D., Medialdea, A., Wennrich, V., ... Bubenzer, O. (2020). Origin and timing of past hillslope activity in the hyper-arid core of the Atacama Desert – The formation of fine sediment lobes along the Chuculay Fault System, Northern Chile. *Global and Planetary Change*, 184(May 2019).  
<https://doi.org/10.1016/j.gloplacha.2019.103057>
- Medialdea, A., May, S. M., Brill, D., King, G., Ritter, B., Wennrich, V., ... Bubenzer, O. (2020). Identification of humid periods in the Atacama Desert through hillslope activity established by infrared stimulated luminescence (IRSL) dating. *Global and Planetary Change*, 185(November 2019), 103086. <https://doi.org/10.1016/j.gloplacha.2019.103086>
- Pfeiffer, T. J., & Higgins, J. D. (1990). Rockfall hazard analysis using the Colorado Rockfall Simulation Program. *Transportation Research Record*, 1288(4), 117–126.
- Placzek, C., Granger, D. E., Matmon, A., Quade, J., & Ryb, U. (2014). Geomorphic process rates in the central atacama desert, Chile: Insights from cosmogenic nuclides and implications for the onset of hyperaridity. *American Journal of Science*, 314(10), 1462–1512.  
<https://doi.org/10.2475/10.2014.03>
- Quade, J., Reiners, P., Placzek, C., Matmon, A., Pepper, M., Ojha, L., & Murray, K. (2012). Seismicity and the strange rubbing boulders of the Atacama desert, Northern Chile. *Geology*, 40(9), 851–854. <https://doi.org/10.1130/G33162.1>
- Rech, J. A., Currie, B. S., Michalski, G., & Cowan, A. M. (2006). Neogene climate change and uplift in the Atacama Desert, Chile. *Geology*, 34(9), 761–764.  
<https://doi.org/10.1130/G22444.1>
- Regard, V., Saillard, M., Martinod, J., Audin, L., Carretier, S., Pedoja, K., ... Héral, G. (2010). Renewed uplift of the Central Andes Forearc revealed by coastal evolution during the Quaternary. *Earth and Planetary Science Letters*, 297(1–2), 199–210.  
<https://doi.org/10.1016/j.epsl.2010.06.020>
- Ruttlant, J. A. (2003). Climate dynamics along the arid northern coast of Chile: The 1997–1998 Dinámica del Clima de la Región de Antofagasta (DICLIMA) experiment. *Journal of Geophysical Research*, 108(D17), 4538. <https://doi.org/10.1029/2002JD003357>
- Sager, C., Airo, A., Arens, F. L., Rabethge, C., & Schulze-Makuch, D. (2020). New types of

- boulder accumulations in the hyper-arid Atacama Desert. *Geomorphology*, 350, 106897. <https://doi.org/10.1016/j.geomorph.2019.106897>
- Salazar, P., Kummerow, J., Wigger, P., Shapiro, S., & Asch, G. (2017). State of stress and crustal fluid migration related to west-dipping structures in the slab-forearc system in the northern Chilean subduction zone. *Geophysical Journal International*, 208(3), 1403–1413. <https://doi.org/10.1093/gji/ggw463>
- Saroglou, C., Asteriou, P., Zekkos, D., Tsiambaos, G., Clark, M., & Manousakis, J. (2018). UAV-based mapping, back analysis and trajectory modeling of a coseismic rockfall in Lefkada island, Greece. *Natural Hazards and Earth System Sciences*, 18(1), 321–333. <https://doi.org/10.5194/nhess-18-321-2018>
- Schween, J. H., Hoffmeister, D., & Löhnert, U. (2020). Filling the observational gap in the Atacama Desert with a new network of climate stations. *Global and Planetary Change*, 184(May 2019), 103034. <https://doi.org/10.1016/j.gloplacha.2019.103034>
- Sippl, C., Schurr, B., Asch, G., & Kummerow, J. (2018). Seismicity Structure of the Northern Chile Forearc From > 100,000 Double-Difference Relocated Hypocenters. *Journal of Geophysical Research: Solid Earth*, 123(5), 4063–4087. <https://doi.org/10.1002/2017JB015384>
- Volkwein, A., Brügger, L., Gees, F., Gerber, W., Krummenacher, B., Kummer, P., ... Sutter, T. (2018). Repetitive rockfall trajectory testing. *Geosciences (Switzerland)*, 8(3), 1–27. <https://doi.org/10.3390/geosciences8030088>
- Wilson, M. F. J., O'Connell, B., Brown, C., Guinan, J. C., & Grehan, A. J. (2007). *Multiscale terrain analysis of multibeam bathymetry data for habitat mapping on the continental slope*. *Marine Geodesy* (Vol. 30). <https://doi.org/10.1080/01490410701295962>
- Wu, Shie-Shin. "Rockfall evaluation by computer simulation." *Transportation research record* 1031 (1984): 1-5.

## CHAPTER 3

### CONCLUSIONS

This thesis acts as an introduction to the boulder fall fields of the Atacama Desert north of 23°S latitude. The nature of this project was exploratory and focused on many different aspects of the boulder fields. Many possible future studies about the nature of the boulder fields and their insights into rockfall processes remain. Below are listed some other possible topics involving the boulder field that one could further investigate.

We discovered a correlation between source area roughness (and slope) and boulder density at the base of the Chinchilla fault scarp. There are many possible directions to further test the robustness of this relationship. We use visual inspection of swath profiles to check the correlation, in which the X values do not always correspond to areas directly upslope/downslope of the other profile. This test could be improved by carefully adjusting the positions and lengths of the profiles so that similar X values corresponded to gravitational fall lines. Then the better matched profiles may be suited to a mathematical comparison like a cross correlation, rather than visual inspection, though one might need to account for the possible lateral spread of falling boulders and weight or filter the cross correlation accordingly. Whereas we see that the mean slope independent roughness metric matches the boulder density slightly better than does the mean slope, a more thorough comparison may test other roughness metrics (like the standard deviation of slope, or wavelet based analysis) (Berti, Corsini, & Daehne, 2013; LaHusen, Duvall, Booth, & Montgomery, 2016).

We observed a correlation between the source and deposit zone, however it remains unclear if the boulders fall because the source zone is rough, or the source zone is rough because boulders have fallen from it. At Chuculay, the relative mass of fallen boulders below each

section compared to the missing pieces in the source area (spaces between the bedrock ‘fingers’) may provide further insights. If the mass values of the boulders and the ‘missing pieces’ are close than the cause for the roughness may be the lost boulders, and if the mass of the boulders is much less than that of the ‘missing pieces’ than we may assume that the fallen boulders are a symptom of the processes eroding the scarp. This analysis may also tell us what percent of the escarpment degradation on a whole is due to rockfalls.

We observed the roughness to boulder density relationship at one scarp only; to test its global applicability, it would be useful to see if this relationship works for other Atacama boulder fall fields. In fact, many of our findings could be tested at other boulder fall fields including: the distributions of the boulders by size, shape, and the degradation morphology. Are the relationships we observed universal to boulder fall fields in the Atacama? We would expect the nature of the underlying bedrock (lithology, cohesive strength, fracture density) to affect the processes releasing blocks from in situ bedrock, the size and shape of the blocks falling, the cohesive strength of the falling block, and the dominant mode of weathering once the block has landed. We would also expect the local environmental conditions to play a large role in eroding escarpment faces to produce rockfalls, possibly triggering rockfalls, and degrading fallen boulders. Tests at a variety of locations could determine the relative importance of local geology versus climate in controlling the type of boulder degradation or even scarp erosion in general.

A regional scale study would also address more questions about the origin of boulder fall fields. What are the environmental limits to their locations? How much rain is required to wash away or prevent the formation of debris aprons? How do the boulder fall fields relate to tectonic activity? Many of the boulder fall fields we observed are near active faults (Fig. A1-1), but we do not know if the activity of those faults affects the development of boulder fall fields, or instead whether the necessary condition is a tall, steep slope, and this is more likely to occur at fault scarps than elsewhere? We suggest that boulder falls are triggered by earthquakes, but is nearby earthquake activity necessary to generate a boulder fall field? To answer these questions,

one would need to create a more detailed catalog of boulder fall fields than what is presented in appendix figure A1-1, and likely requires the field checking of many remote escarpments.

We used our findings of a large range of hypothetical coefficients of restitution (COR), and large boulder fall obliquity to suggest that certain rockfall modelling approaches be preferred (notably 3D models with stochastic impacts). However, we never used the data we have from Chuculay to test any rockfall models. A natural first comparison would be to test the Chuculay boulder fall density heatmap to the fall probability heatmaps generated by stochastic process based on hundreds or thousands of virtual rockfalls. Do the models predict the density to distance, or size to distance relationships we observe? In this way, our high sample size rockfall map could help tweak how rockfall models produce their stochastic iterations and eventually fall distance probabilities.

Can the models recreate the oblique fall angles, or the variable bounce mark spacing we observe? If so, what parameters of the model most determine the variability of the spacing between bounce marks, or the possible obliquity of the fall path? I would likely start my rockfall modelling tests with the RAMMS rockfall modelling software (Bartlet et al., 2013) published by the Swiss Federal Institute for Forest, Snow and Landscape Research (WSL) perhaps the most sophisticated rockfall modelling software, which is directly calibrated using full scale experiments recorded with state of the art technologies (Caviezel et al., 2019; Lu et al., 2019).

## **REFERENCES**

- P. Bartelt, Y. Buehler, M. Christen, Y. Deubelbeiss, C. Graf, B. W. McArdell, RAMMS—Rapid Mass Movements Simulation: A Numerical Model for Rockfall in Research Practice, User Manual v1.5 (Institut für Schnee- und Lawinenforschung, Davos, 2013).
- Berti, M., Corsini, A., & Daehne, A. (2013). Comparative analysis of surface roughness algorithms for the identification of active landslides. *Geomorphology*, 182, 1–18.  
<https://doi.org/10.1016/j.geomorph.2012.10.022>
- Caviezel, A., Demmel, S. E., Ringenbach, A., Bühler, Y., Lu, G., Christen, M., ... Bartelt, P. (2019). Reconstruction of four-dimensional rockfall trajectories using remote sensing and rock-based accelerometers and gyroscopes. *Earth Surface Dynamics*, 7(1), 199–210.  
<https://doi.org/10.5194/esurf-7-199-2019>
- LaHusen, S. R., Duvall, A. R., Booth, A. M., & Montgomery, D. R. (2016). Surface roughness dating of long-runout landslides near Oso, Washington (USA), reveals persistent postglacial hillslope instability. *Geology*, 44(2), 111–114. <https://doi.org/10.1130/G37267.1>
- Lu, G., Caviezel, A., Christen, M., Demmel, S. E., Ringenbach, A., Bühler, Y., ... Bartelt, P. (2019). Modelling rockfall impact with scarring in compactable soils. *Landslides*, (July).  
<https://doi.org/10.1007/s10346-019-01238-z>

## APPENDIX

### ***Section A1: Where are the boulder fall fields?***

As is briefly mentioned in CH. 2-2.1, we differentiate between boulder fall fields and other boulder fields on the desert floor. For a set of boulders lying on the desert floor to be considered a boulder fall field, the boulders must lie at the base of a steep slope and be much more common in the low-gradient area beyond the steep slope. Were a set of boulders moved by gradual creep, there is a high probability of finding them at all slope positions below their source region. In contrast, rock fall-generated boulders will mostly accumulate where their descent has been slowed by reaching a zone of low gradient. Boulder fall fields often, but not always, have degrading boulders building up aprons of debris. In all four cases we examined closely, boulder fall fields have bounce marks, providing direct evidence of rapid descent and deposition.

Mapped boulder fall fields plotted in Figure A1 were first identified by viewing in tandem a slope map based on the SRTM 30m DEM, and Google or Bing satellite imagery. Scrolling through imagery of Northern Chile I looked for boulders at the base of all slopes that are steeper than 30 degrees. If there appeared to be dark spots (likely boulders) at the base of a steep slope that location was plotted as a yellow circle in Figure 1A. The major pattern that emerged from this search was the lack of boulders at the base of slopes (steep or not) that had well developed drainage systems. In other words, boulder fall fields are more likely to be spotted at the base of linear escarpments. Mapped boulder fall field locations are presented in Table 1.

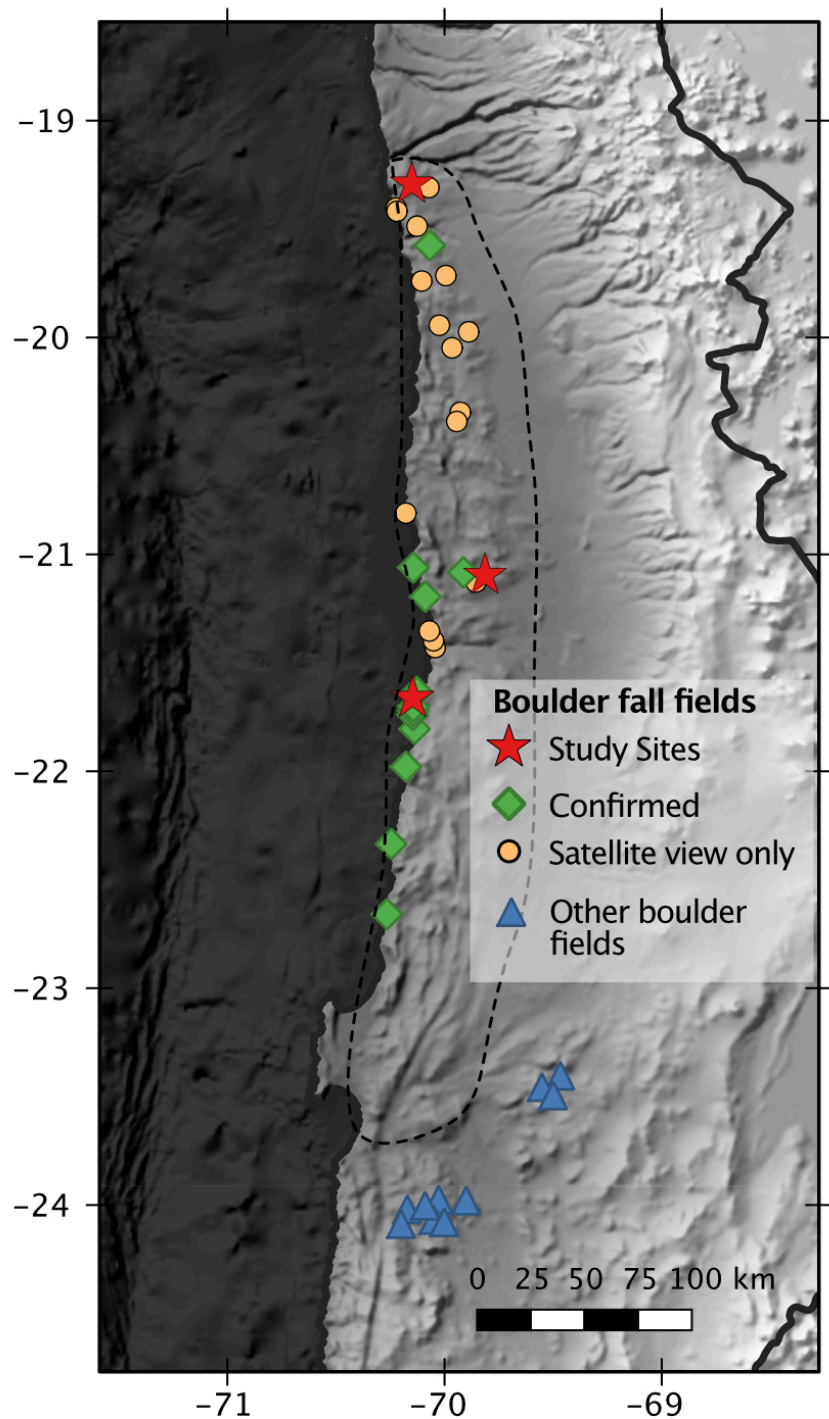


**Figure A1:** Location of boulder fall fields in Northern Chile, north of 23°S. Red stars indicate locations of our primary study areas where more than one day was spent examining the fallen boulders; from north to south these are Atajaña, Chuculay, and Caleta Punta Arenas. Green diamonds indicate locations where boulder fall fields were confirmed in person; these sites are either along the coastal highway at the base of the coastal escarpment, or along prominent east-west trending fault scarps. Yellow circles are locations where possible boulder fall sites have been viewed through satellite imagery readily available through Google or Bing (resolution varies but

is sometimes as high as ~0.5 or 1 m). These sites have not been confirmed. Dashed line represents the loosely defined boundary outside of which we did not search for boulder fall fields. Blue triangles represent location of other types of boulders fields studied in the Atacama (Matmon et al., 2015; Placzek et al., 2014; Quade et al., 2012; Sager et al., 2020)

### **Section A2: Initial scarp morphology mapping.**

Figures A2 -1-3 are surface morphology maps of three boulder fall field sites. All features were mapped on Bing or Google earth imagery.

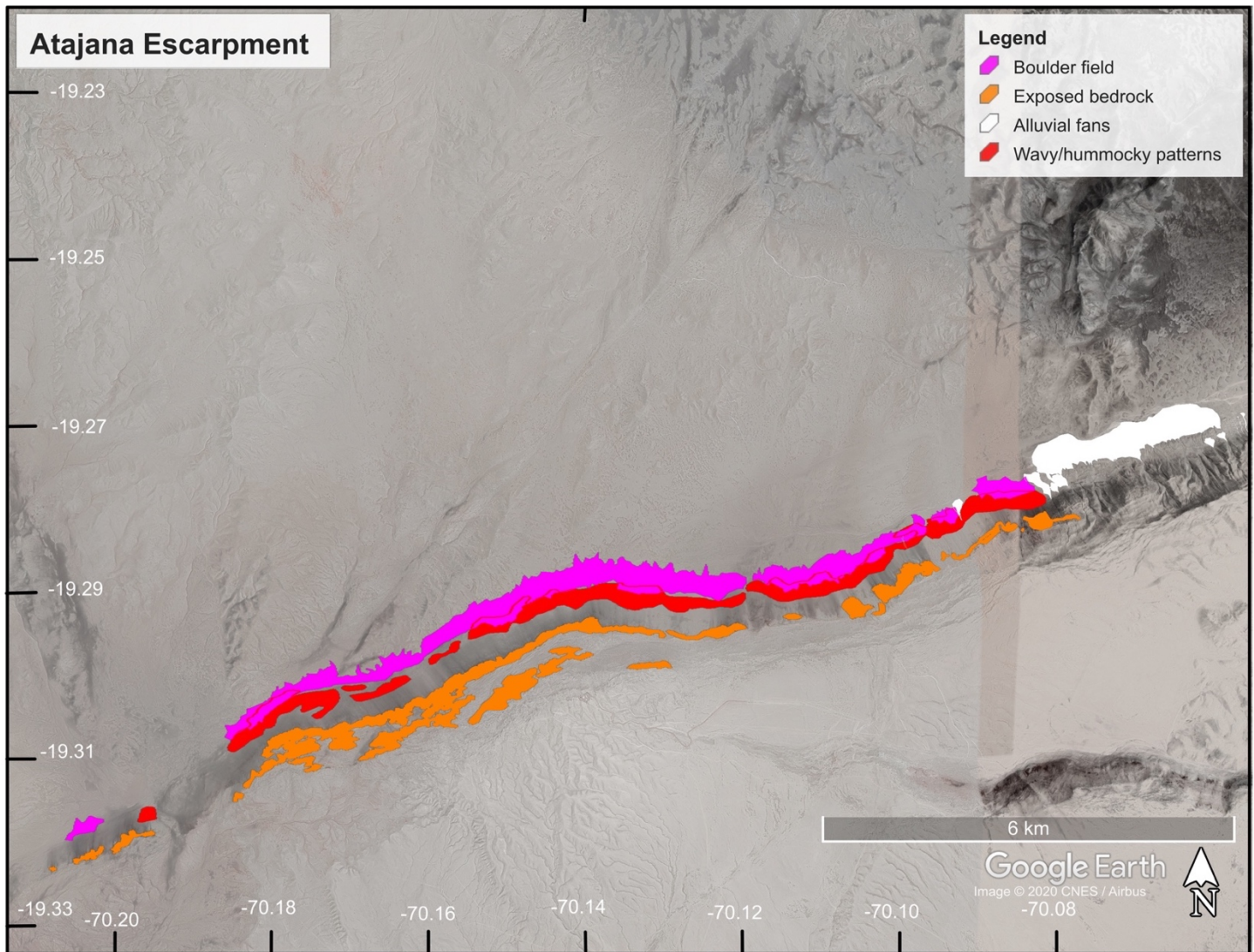


**Figure A2-1:** Satellite image landform class mapping. Pink delineates extent of fallen boulder field based on the occurrence of visible boulders. Orange indicates extent of exposed bedrock, primarily mapped based on the texture of the imagery. White indicates alluvial fan deposits. Red indicates wavy/hummocky areas, as defined by variations in color, appearing to be wavelike successions of dark and light gray. Two types of wavy/hummocky terrane are present. For one type, the color variations occur on a wavelength of ~ 20-30m from peak dark to dark, and the color bands are elongated down slope. For the second type, the wavelengths are shorter, around 10 m, and the forms are less elongate, and better described as hummocky areas.

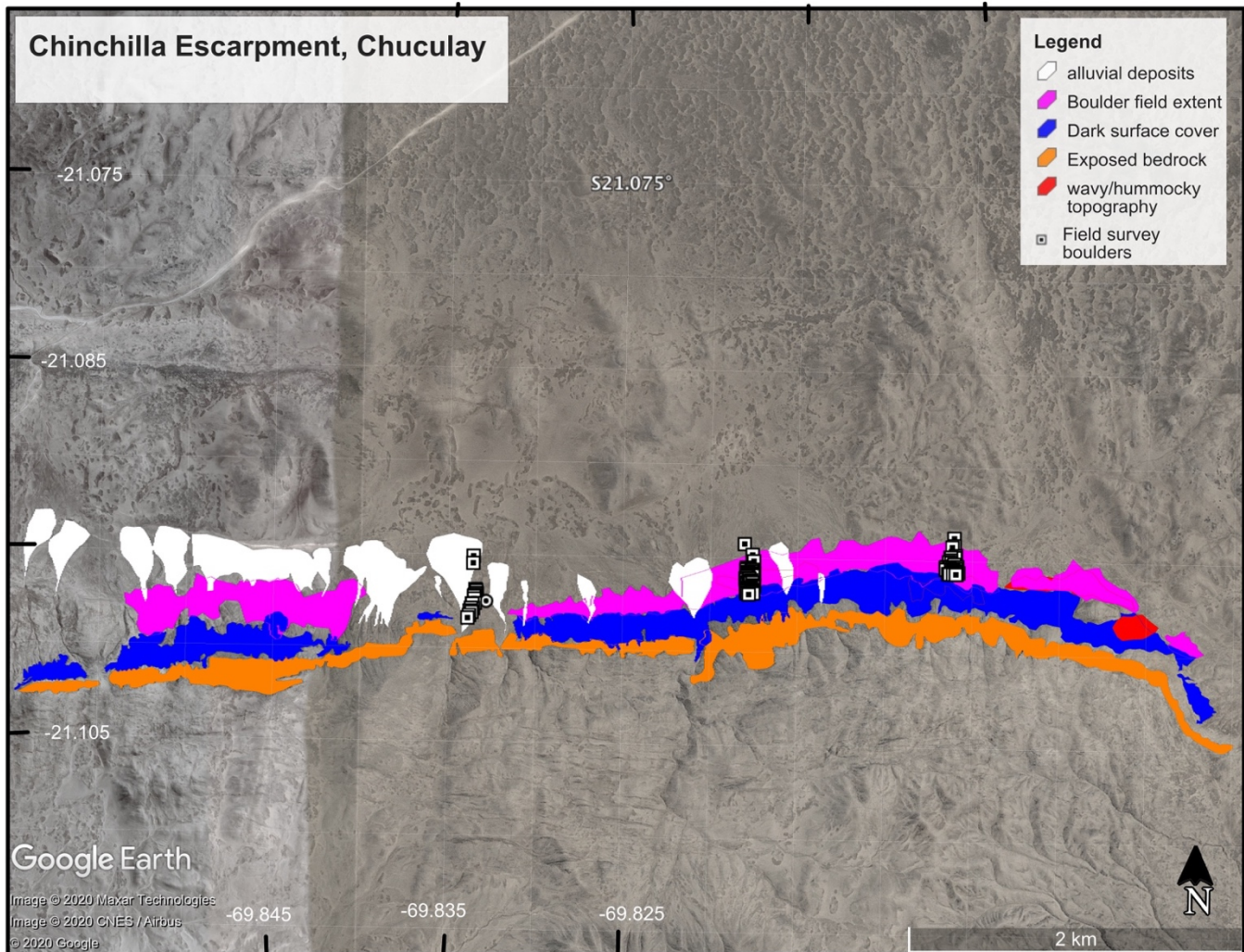
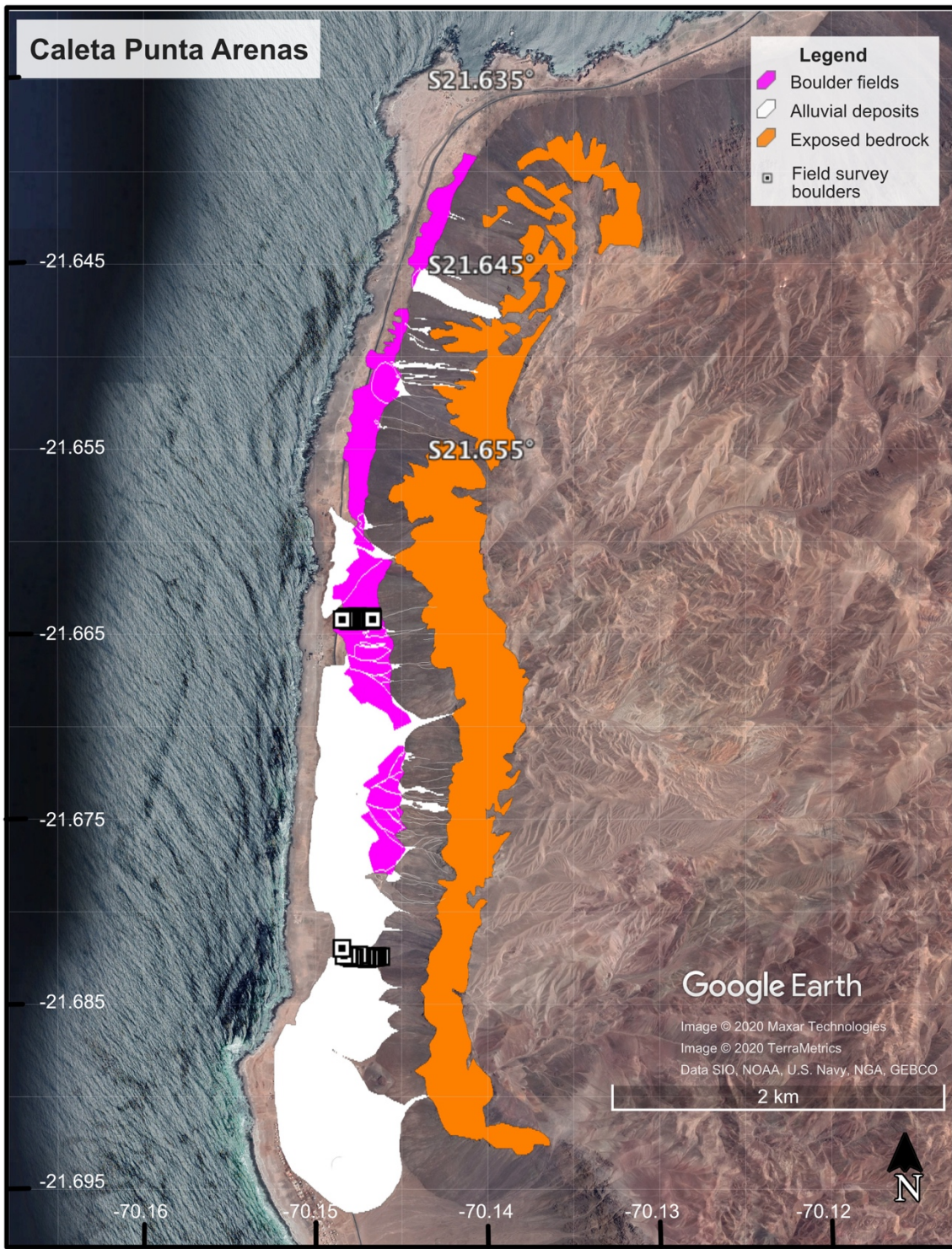


Figure A2-2: Satellite image landform class mapping of the Chinchilla escarpment of the Chuculay fault system. Pink delineates extent of fallen boulder field based on the occurrence of visible boulders. Orange indicates extent of exposed bedrock, primarily mapped based on the texture of the imagery, and including talus chutes between bedrock ‘fingers’. White indicates alluvial fan deposits. Red indicates wavy/hummocky areas, as defined by variations in color, appearing to be wavelike successions of dark and light gray. Two types of wavy/hummocky terrane are present. For one type, the color variations occur on a wavelength of ~ 20-30m from peak dark to dark, and the color bands are elongated down slope. For the second type, the wavelengths are shorter, around 10 m, and the forms are less elongate, and better described as hummocky areas. The eastern wavy/hummocky topography is collocated with the boulder fields, and therefore not very visible on this map. Blue is a dark layer, strongly visible in satellite imagery, with uncertain origins and significance, likely representing scree cobbles. Squares are locations of boulders cataloged in person at Chucualy. Data recorded at each boulder available in Table 2.



**Figure A2-3:** Satellite image landform class mapping of the Caleta Punta Arenas section of the coastal escarpment. Pink delineates extent of fallen boulder field based on the occurrence of visible boulders. Orange indicates extent of exposed bedrock, primarily mapped based on the texture of the imagery. White indicates alluvial fan deposits. Squares are locations of boulders cataloged in person. Data recorded at each boulder available in Table 2.

### ***Section A3: Field boulder survey***

At Caleta Punta Arenas and Chuculay we conducted a field survey of ~250 boulders, recording their degradation morphology, size, strength, and composition. In addition to creating a catalog of measured boulders (Table 2), with which to test our initial observations, the act of creating this catalog informed our knowledge of the boulder processes. While most of the data presented in this section was not used in the primary chapter of this thesis, these observations formed the baseline for further analysis of the position, relative abundance, and degradation of the boulders.

#### *Locations of the boulder surveys*

At Chuculay, we chose three 50 m wide strips perpendicular to the fault to survey boulders (Fig. A2-2). We picked three strips spanning the study area. In the strip to the farthest east, a wide variety of degradation morphologies and bounce marks were observed. In the central strip, high resolution drone imagery was obtained due to high bounce mark density. In the strip at the far west of the study region, less boulders and no bounce marks were observed, making it contrast with the other regions. Within the far west site, the abundance of alluvial deposits (see Fig. A2-2), and dearth of class 2 or 3 boulders suggest that surface processes may be different and rapid boulder falls may not be the dominant emplacement mechanism for the boulders. All of these sites were also selected due to the high quality of drone imagery upon a quick initial processing. We also selected boulder survey area where landforms suggested there had been no fluvial processes (i.e., we avoided the center of an alluvial fan).

At Caleta Punta Arenas we chose one 25 m strip perpendicular to the scarp in an area where fluvial processes did not dominate, and a second linear transect on an alluvial fan (Fig. A2-3). We chose to use a 25 m strip width instead of a 50 m strip width because the density of boulders was much higher. In fact, close to the scarp front there were too many boulders for us to catalog. Instead, for the crowded areas of the fault scarp we adopted a linear transect approach, selecting to record data for each boulder that was touching a line. This methodology still gives us a sense of how the boulders change as distance from the scarp changes while meeting timing requirements for our data collection.

#### Boulder selection criteria

The first criterion was that the boulder must have been identifiable on the 1:12,000 scale map imagery. This means that boulders which we did not catalog would fall into 3 groups:

- 1) The rock was too small to see in the imagery. Unfortunately this is not entirely consistent between areas. Nevertheless, the cutoff size for a perfectly black boulder laying by itself on the sand was around 50 x 50 cm.
- 2) The rock tone was too similar to the tone of its surroundings, resulting in trouble discriminating the boundaries of the boulder. This is particularly true towards the base of the scarp where much of the surface is covered in debris, so a smaller fallen rock there is more difficult to identify than further away from the scarp where the image might be less noisy. This is also true in areas where many boulders have collected.
- 3) The boulder was in an area of the imagery that our initial processing rendered too blurry. Mistakes in the initial imagery acquisitions did make some regions of the boulder field difficult to process.

*Observations*

Figures A3-1 through A3-4 detail the main relationships observed during the field surveys. These relationships are extrapolated on and further investigated using the drone imagery based surveys represented in the main text.

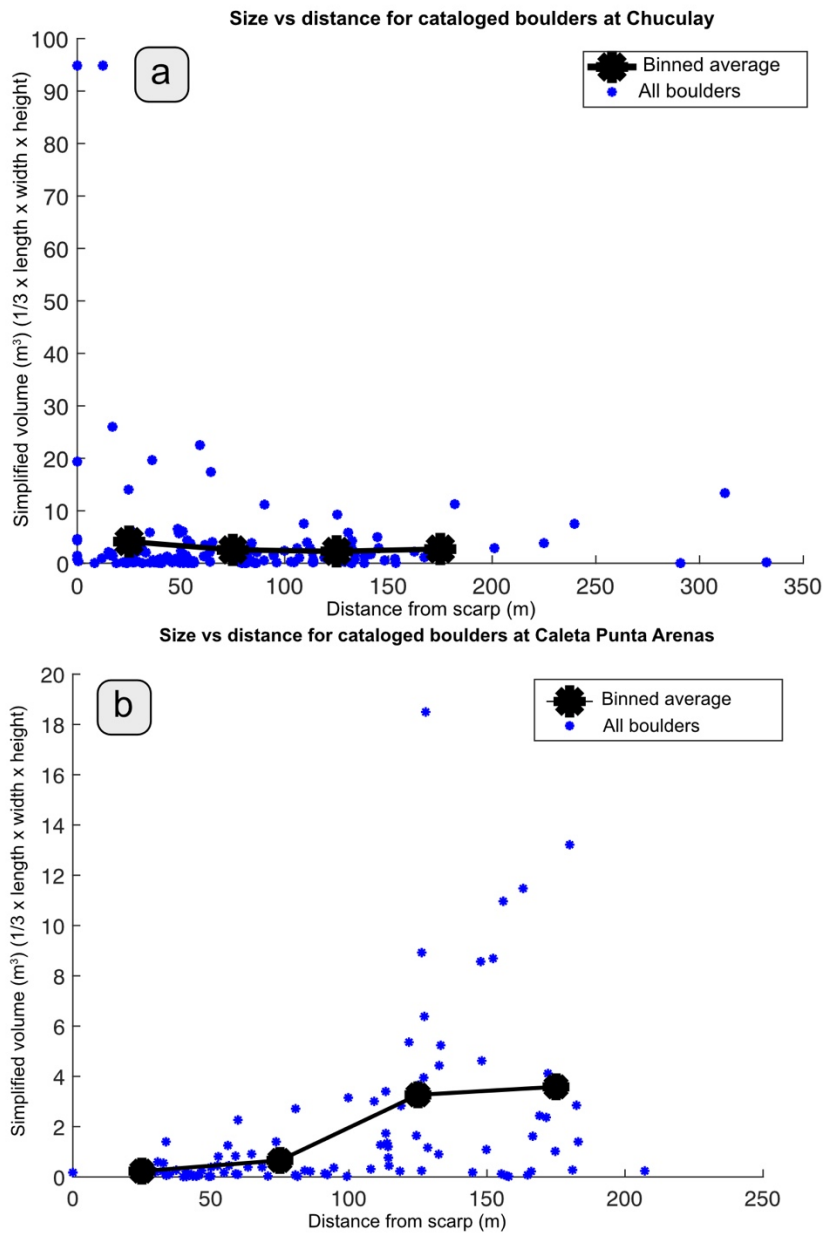


**Figure A3-1:** Size vs distance from scarp: Blue dots mark each boulder's distance from scarp base and simplified volume. Simplified volume calculated assumes each boulder is a pyramid. Black dots represent the average simplified volume of all boulders within a 50 m long bin. In general we observed that boulders increase in size as they increase in distance from slope (Ch. 2 Fig. 12a). Surprisingly, a pair of outliers measured at Chuculay leads to mean values in 50 m long bins that conceal the size versus distance relationship observed in the drone imagery based survey. The data of the cataloged boulders at Caleta Puna Arenas more clearly illustrate that larger boulders are transported further from the base of the escarpment.

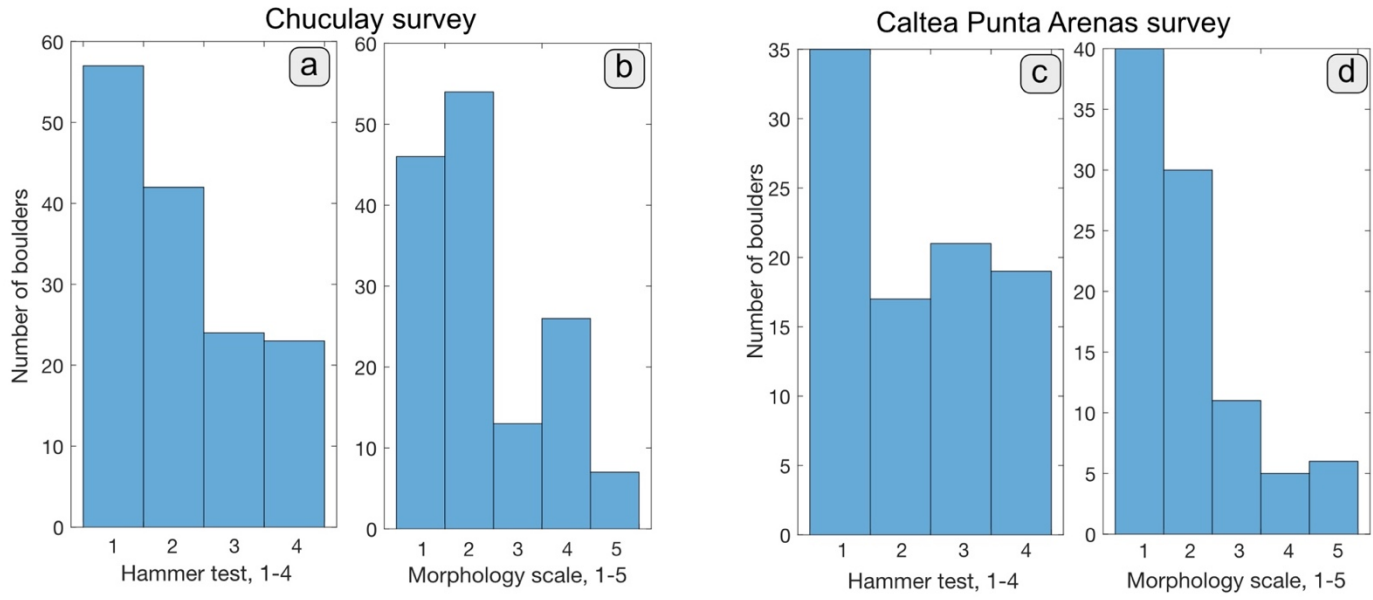


**Figure A3-2:** Histogram of the strength and morphology tests on the surveyed boulders at both survey sites. Hammer test conducted by hitting the pick end of the rock hammer against the boulder.

**Hammer scale:** 1- Rock hammer bounces back leaving nothing but a light scratch on the boulder. Often accompanied by a high pitched “ping”. 2-The Rock hammer bounces right back, but cracks the rock or does some damage in some way. Any damage is small and localized within ~10 cm of the area the hammer hit. 3-The hammer bounces back but causes large damage, breaking rock in areas where joint/fractures exist greater than ~10 cm away from the hammer hit. 4- The rock hammer does not bounce back, the rock absorbs all of the energy from the blow into damage or soil displacement.

**Morphology scale:** 1- A fresh rock. No visible skirt surrounding the boulder (less than ~20 cobbles of debris). 2-A clear rock with a small debris skirt, the debris skirt does not exceed 25% of the core rock height. 3-The boulder skirt went from 40-60% of the core rock’s height. 4- The debris skirt made up a majority of the height of the Rock, 60% and greater. 5-Only a pile of debris, the core rock is no longer visible.

To compare the field assessment 5 tier morphology scale to the drone imagery assessment 3 tier scale: field scale class 1 boulders are equivalent the drone scale class 1 boulders, the field scale class 2 and class 3 boulders are drone scale class 2, and the field scale class 4 and class 5 boulders are drone scale class 3.

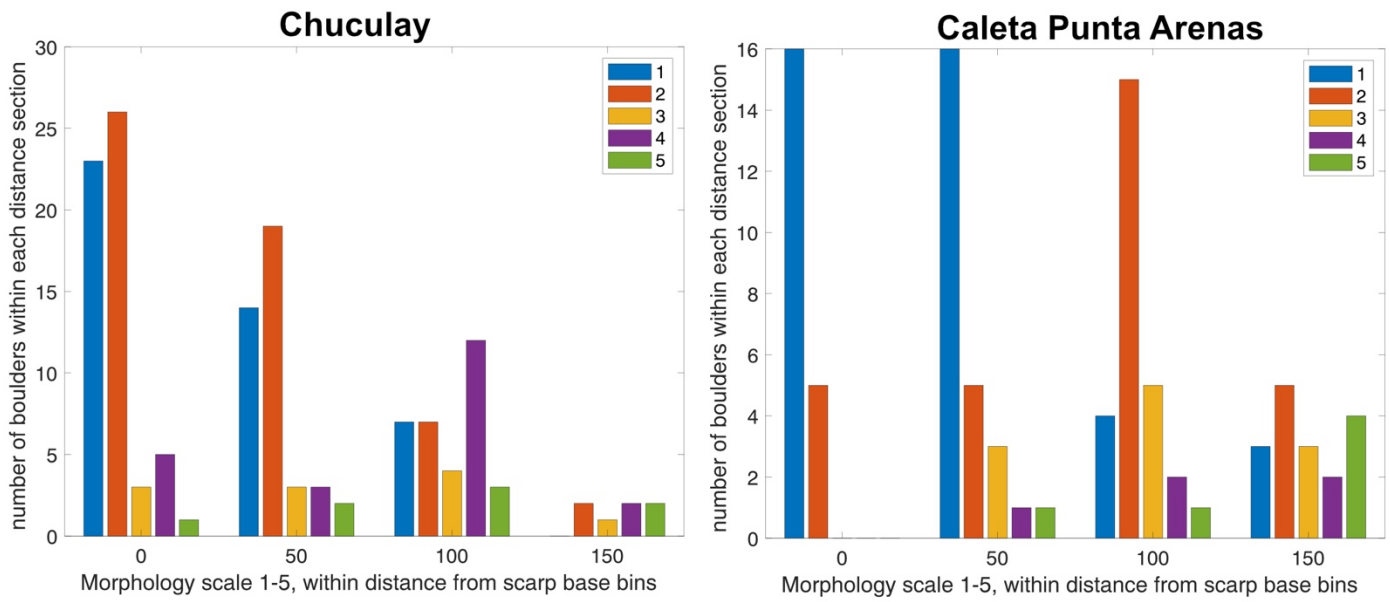


**Figure A3-3:** Boulder morphology vs distance from the scarp. Boulders that are further away from the scarp front are, on average, morphologically older than boulders near the scarp front. See caption of Figure A3-2 for details on the morphology classes.

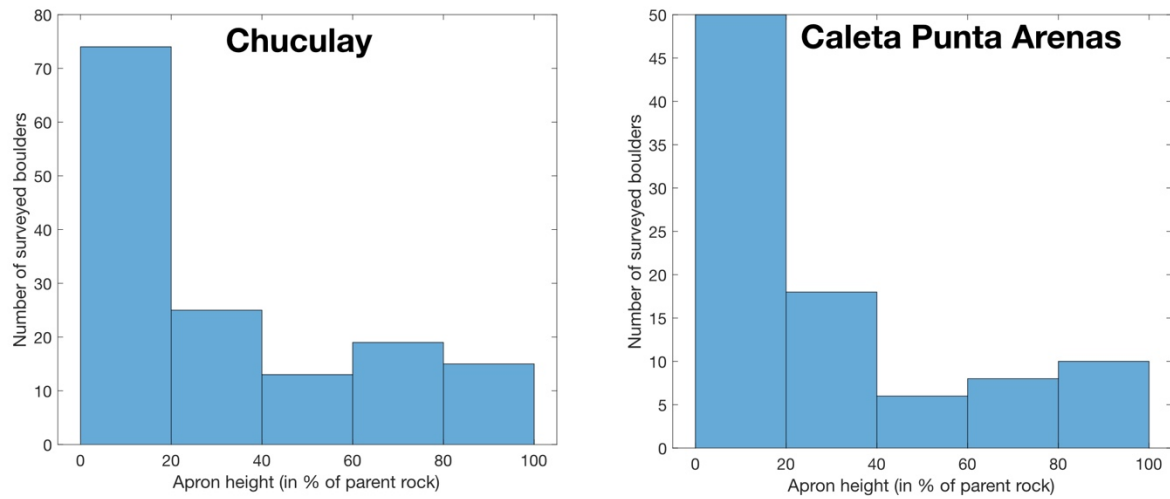


**Figure A3-4:** Boulder debris apron height measured as a percentage of the height of the parent boulder. Note that at both fields sites boulders with smaller debris skirt heights make up most of the surveyed boulders. The boulders with debris skirt heights between 0 and 20 percent may be class 1 or class 2 degradation morphology boulders.

#### **Section A4: Testing standard deviation of local slope as an age proxy for fallen boulders.**

The unique style of boulder degradation in the boulder fall fields could possibly allow for the dating of a boulder fall, simply by using the 3-D shape of that boulder. The first step of this task is to create a metric which acts as a proxy for age of the boulder. In this section we test the standard deviation of slope as this proxy, using 3 models of boulders from Chuculay, spanning different apparent ages.

Models of the boulders were created using Agisoft Photoscan (Fig. A4-1 a-c). I extracted 10 profiles passing through the highest point of each model (Fig. A4-1d). Slopes were then extracted from the best fit line to all the points with a moving window along the profile length axis (Fig. A4-1e), with each window keeping a 50% overlap with the previous window. Then the standard deviation of the slopes calculated for every window was computed. While various moving window sizes are tested, 30 cm is chosen as a preferred size, because it is large enough to discount the roughness caused by a small cobble, but small enough to capture the shape of the boulder.

Initial results (Fig. A4-2) show a general discrimination between an older mound of debris (boulder C) and intact boulders (boulders A & B). However, the standard deviation of slope value for boulder A is lower than for boulder B, indicating that the standard deviation of slope does not capture the relative age of boulders.

Various other roughness measuring metrics could be tested on this data. Additionally, one could attempt to use diffusion modelling to test the age of boulders. Any age-morphology metric would require extensive calibration using real dates, and multiple boulders to create a robust methodology.

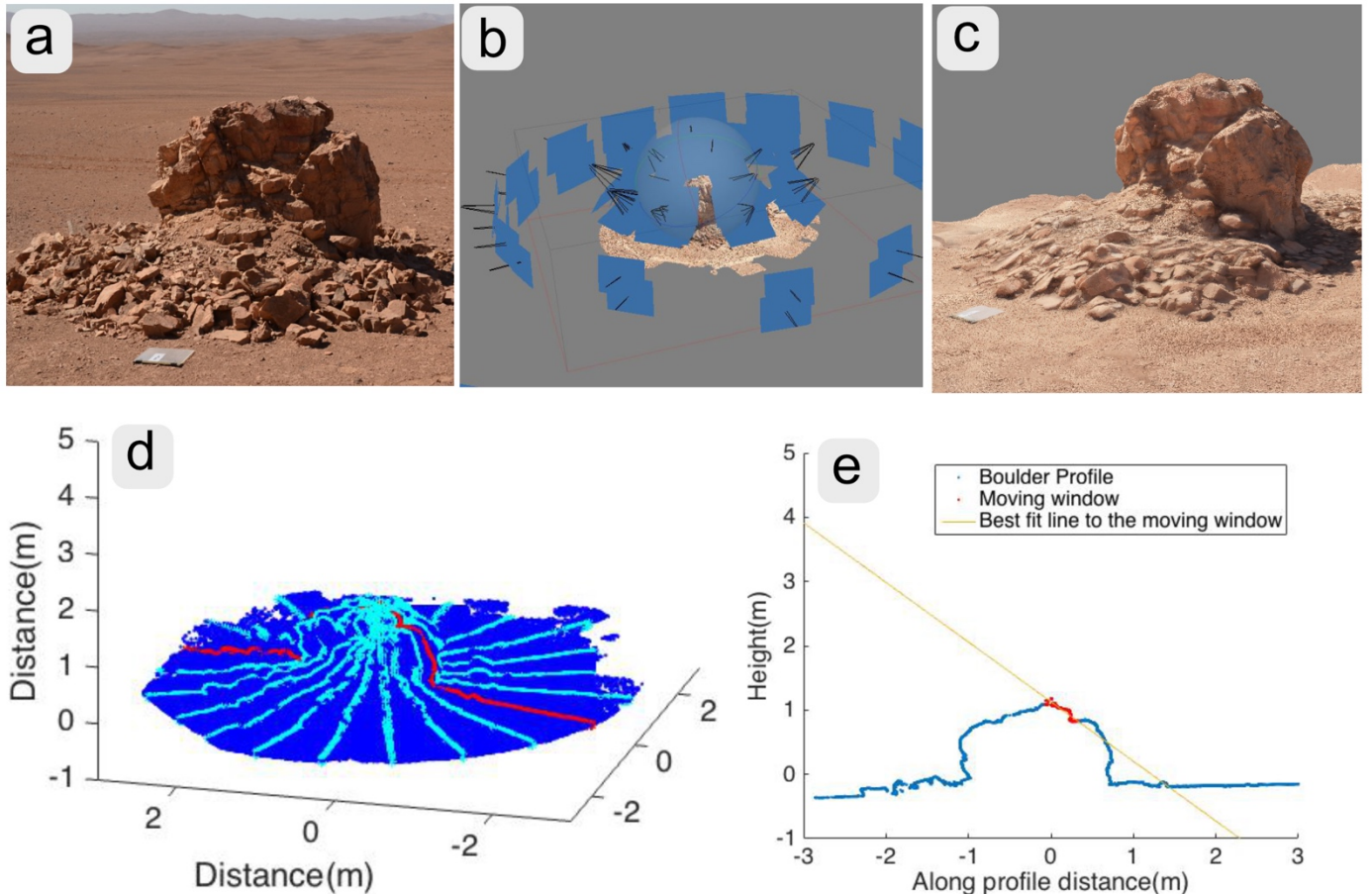


**Figure A4-1:** Digitizing a boulder for analysis. a) raw photo of a boulder (boulder B). b) The position of each photo taken of the boulder (121 total). c) A screenshot of a textured digital mesh of the boulder output from Agisoft photoscan. d) A plot of the point-cloud of the boulder used for analysis, overlain by the 10 cyan profiles used with the red profile plotted in e. e) a moving window slope extraction, points within the moving window in red, and the line to fit them in orange.

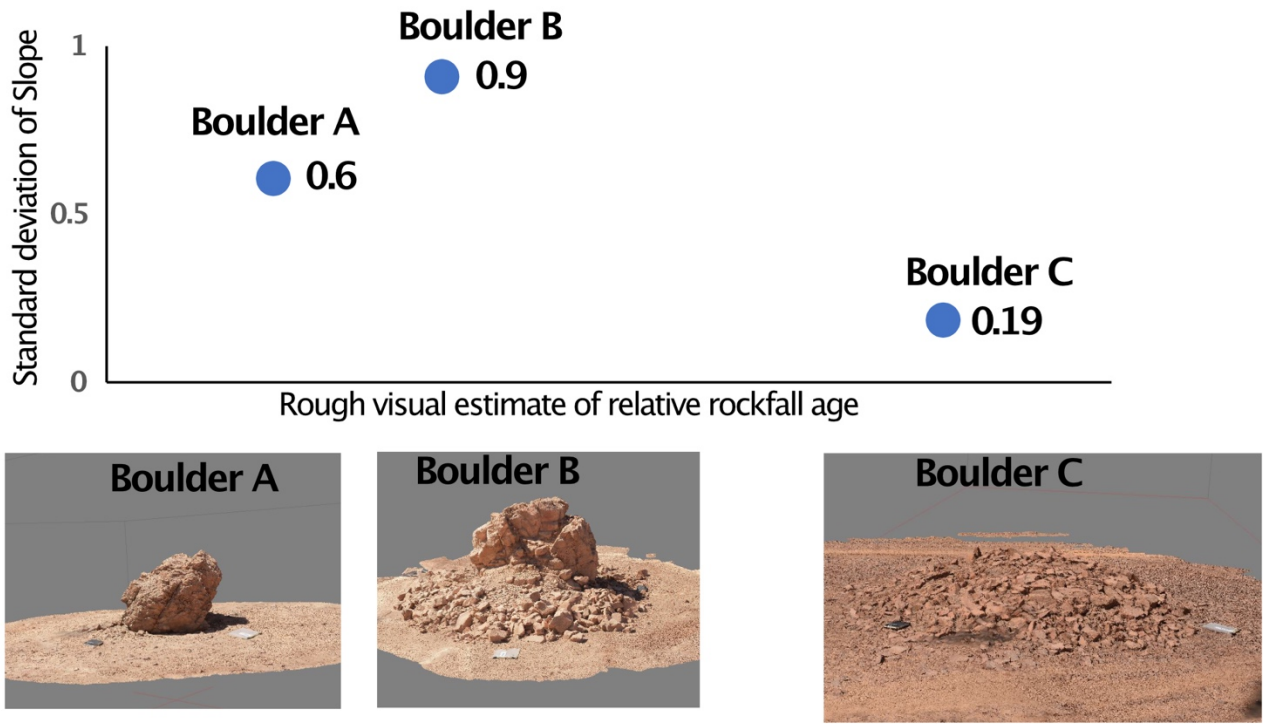


**Figure A4-2:** Standard deviation of slope, initial results.

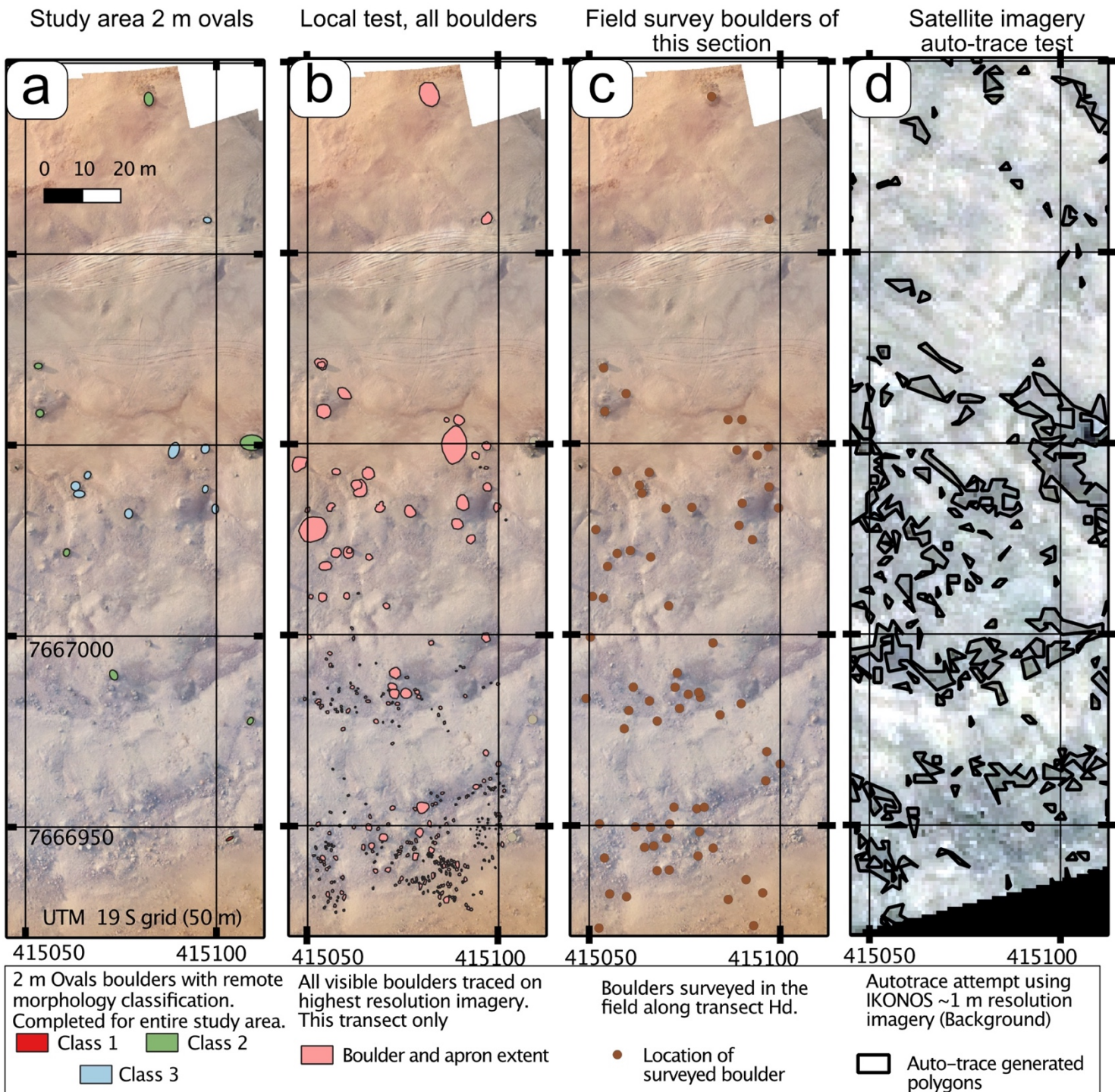
Radial profile extracted standard deviation of slope values, for a moving window size of 30 cm. The X axis reflects a rough estimation of relative age based on the relative volume of the debris skirt around the center of the boulders. Below are models of each of the boulders, the map board is present for scale in each model.

### ***Section A5: Boulder tracing, and scarp morphology comparisons.***

The boulders are not evenly positioned within the deposit zone. At Chuculay, in the west of our study area there is a 200 m gap along the escarpment where there are almost no boulders, and the density of fallen boulders along the rest of the escarpment isn't constant along strike of the scarp. If we assume that the density of boulders at the base of the slope represents ongoing processes that will continue, it follows that new boulders may be likely to fall where we have measured the highest density of older boulders. Thus we wish to measure the density of boulders along the base of the escarpment.

To measure the boulder density, we used the drone orthomosaic to trace ellipses around every boulder with a diameter greater than 2 meters (Fig. A5-1a). This was done through the entire length of the study area. If a class 2 or 3 boulder had an especially large apron, then the area captured was inside of the total extent of the apron. While this technique did not capture all of the boulders that may have been possible to map (Fig A5-1b), limiting the mapping to only large boulders ( $> 2$  m) was time efficient, and made the measurement more consistent across the entire study area, because in locations with poor image resolution smaller boulders would be missed. Our initial attempts at automatic boulder tracing were unsuccessful (Fig A5-1d), revealing that algorithms were not able to delineate between boulders and regions of surface covered with cobbles whose color is similar to a boulder .

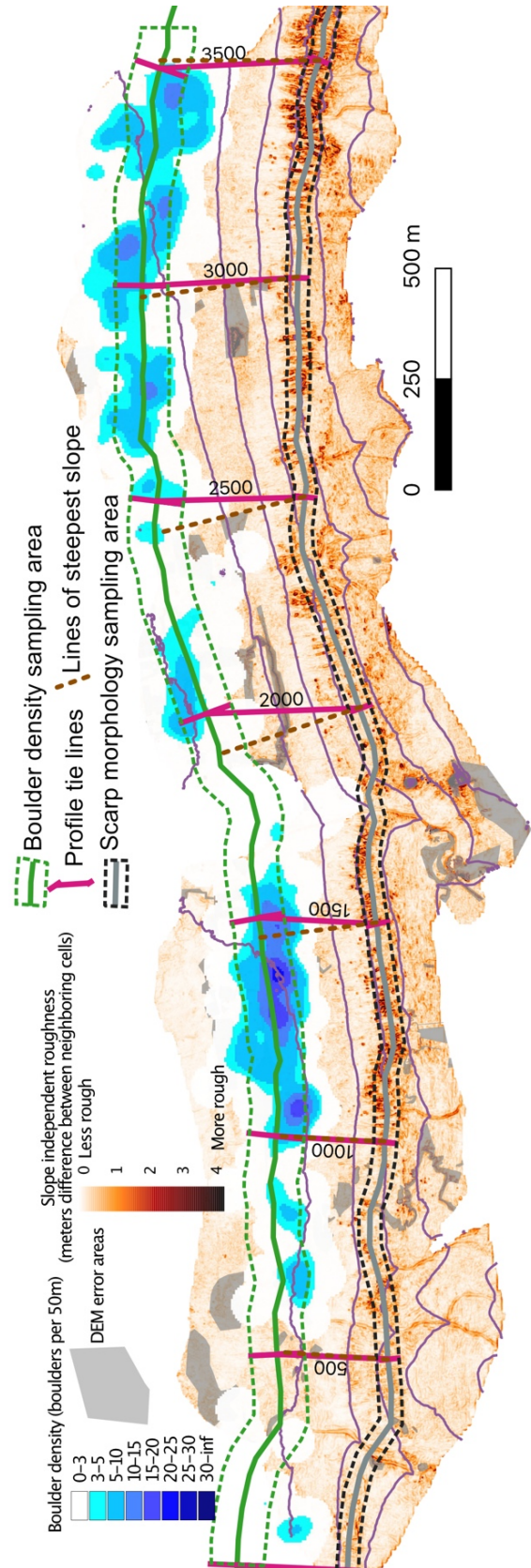
We then compared the boulder density to features of the source area of the escarpment (Fig A5-2 & 3). In addition to map view qualitative assessments, we used swath profiles to make this comparison (still qualitatively). This methodology is described in figure A5-2.



**Figure A5-1:** Tracing of boulders. a) shows what boulders were traced using the slope wide  $> 2$  m diameter tracing method. b) shows all the boulders that could be traced on only this section of particularly high resolution drone ortho-imagery. Note the clumping of boulders in topographic depressions. This methodology could not be used for the entire slope because 1) time constraints and 2) not all of the imagery is as high resolution as this section, so this method would artificially decrease the boulder count in areas with slightly blurry imagery. c) points of boulders

surveyed in the field along this section (Fig. A2-2 center). d) attempt at automatically tracing boulders, using IKONOS ~1 m resolution satellite imagery, and the auto-trace algorithm in CANVAS pro.

**Figure A5-2** Swath profile comparison explanation. Repeated figure from Ch. 2. Fig. 13 but with expanded explanation. Background white to red map is the slope independent roughness, and background white-blue is the boulder density map. Purple lines are 50 m elevation contour lines. Green solid and dashed lines show data sample area for the boulder density swath profile plot, and grey solid line with black dashed lines show the sample area for the source area swath profile plots. Magenta profile tie lines show points with the same X value in both the source area and deposit area profiles, while the brown dashed lines of steepest slope show what points line directly downhill from those x values on the source zone profile. Note that one x value on the source area profile line does not necessarily lie directly uphill from location with the same x value along the deposit zone profile line. This figure explains how the data in the swath profile plots in figure A5-3 are sampled. First profile lines are drawn across the escarpment through the center of the deposit zone (solid green) and the center of the source areas (solid grey). Then lines (50 m long for the deposit zone, and 25 m long for the source area) are drawn perpendicular to the first profile line at 1 m intervals. The underlying data (boulder density, roughness, slope, etc) is sampled along the perpendicular lines, also at 1 m increments. For each perpendicular line, the minimum, maximum, and mean value of the underlying data is recorded.



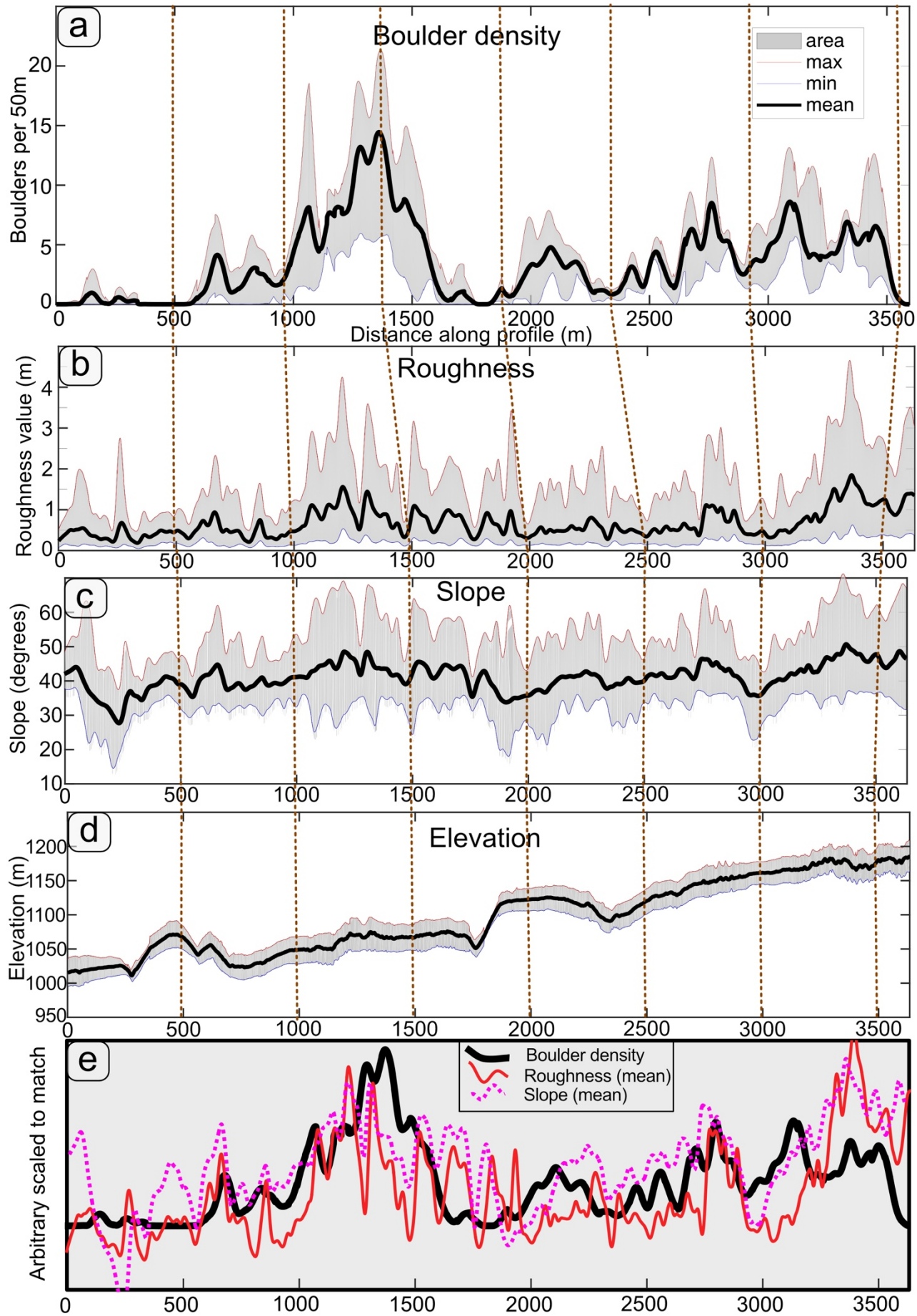


Figure A5-3 Swath profile comparisons. Subfigures (a), (b), and (c) are presented in Ch. 2 Fig.

13, but are repeated here with expanded explanation. a) boulder density data extracted from within the green dashed area along the deposit zone in A5-2. Thick black line is the mean of the data points extracted along each perpendicular cross-profile line to the along scarp profile line, while the red upper bound represents the highest value and the blue lower bound represents the lowest value along each cross-profile line. b) The slope independent roughness metric discussed in CH.2 6.4 . c) is slope data from the 1 m drone DEM and c) is elevation data from the 1 m drone DEM. The Data in a b and c are filtered with a 50 m window butterworth filter. Brown dashed lines across a-d represent comparison lines following the line of steepest slope from the source profile to the deposit profile. e) superimposes and scales the density, roughness, and slope mean profiles for easier comparison (Note that the X positions of the profiles are not altered to match the fall lines). Roughness and slope metrics follow similar paths, likely because both are calculated by comparing neighboring DEM cells though in slightly different ways. Interestingly, the maximum and minimum slope curves do not follow this pattern. The roughness profile better matches the low to high boulder density gradient in the western third of the study area, while both roughness and slope only loosely fit the boulder density profile in the east.

### ***Section A6: Bounce kinematics calculations***

To compute the coefficient of restitution values from the bounce marks, we follow the methods of Saroglou et al. (2018), using the Matlab function copied below (before Figure A6-1). Input data and calculated values are available in Table 3.

We calculated many hypothetical coefficients of restitution values, and observed a wide range in values. In this section we test to see if we can find what determines the COR values we calculated. First, we will compare the COR values for each bounce mark track to properties of the boulder which made the track (Fig. A6-1-3). Because each boulder has many associated COR values, we compare the boulder property to both the average and the standard deviation of those COR values. We find no relationships.

Then we probe the relationship between our calculated COR values and topography. First, we test the relationship between COR and the slope at the location of the bounce mark (Fig. A6-4), where we find no correlation. Then we use an elevation profile along the bounce track to visually test the relationship between COR values and the topography at neighboring bounce marks, and if the style of bounce mark (deep or shallow) relates to the COR value (Fig. A6-5).

We may expect that some COR values are determined by the slopes at neighboring bounces (Fig. A6-5). Using plots similar to Figure A6-6, I categorized every  $COR_v > 1$  bounce mark into 3 categories based on how likely I believed the  $COR_v$  value was affected by the topography neighboring the bounce mark:

1: likely- means the topography changes in such a way that we may expect trajectory changes which could result in a short bounce followed by a long bounce

2: uncertain- there are noticeable topography changes in the region of the bounce, but it is uncertain how the topographic changes should affect the bounce spacing. This category is applied also if the distance is  $\sim < 1\text{m}$ .

3: unlikely- no noticeable topography changes in the region of the bounce marks, or the exact opposite trajectory/spacing change is expected due to the topography (uncommon).

I found that of the 186 COR<sub>V</sub> exceeding 1 bounce marks judged,  $\sim 25\%$  were (1) likely,  $\sim 44\%$  were (2) uncertain, and  $\sim 30\%$  were (3) unlikely to be affected/controlled by topography. This very rough inspection illustrates that the local topography likely plays some role in our calculated COR values.

Finally, we examined the style of bounce marks along the tracks. We saw that bounce mark shapes do not commonly change much along the course of a track (at least where they are recorded in the deposition zone). High estimated COR<sub>V</sub> values are found to relate to any style of bounce.

## Coefficient of restitution calculation matlab function.

```

function [ vcor ncor tcov ] = bounce_coeff_calc( dx1, dx2, dy1, dy2, slope )
%Function to calculate the coefficients of restitution for a bounce between
%two hypothetical ballistic trajectories, connecting 3 bounce marks
% inputs required are:
% dx1 and dy1 horizontal and vertical distance between first and second bounce mark
% dx2 and dy2 horizontal and vertical distance between second and third bounce mark
% slope slope at the second bounce mark, for which the COR calculations are
% being made
%% set up the parameters
thetas=[-45:1:90]; %Will compute trajectories for all release angles in thetas
Vos1=zeros(1,length(thetas)); %get array ready for initial velocity values Vo (bounce
1-
>2)
Vos2=zeros(1,length(thetas)); %get array ready for initial velocity values Vo (bounce
2-
>3)
%tblsht
Vos1=nan(1,length(thetas));
Vos2=nan(1,length(thetas));
g=9.80665;%gravitational constant
%% calculate initial velocities
% instead of analytically solving for the minimum velocity, we loop
% through the thetas one degree at a time, solve for Vo at each theta, then
% use the minimum Vo
for tt=1:length(thetas)
    theta=thetas(tt);
    Vo1tt=(-g*dx1^2) / ( (2*cosd(theta)^2) * (dy1-(dx1*tand(theta))) ) )^(1/2); %initial
    %velocity required at each release angle
    % if the result is real and nonzero put it in the storage Vo array
    if isreal(Vo1tt)==1 % need to check, b/c not all angles are possible.
        Vos1(tt)=Vo1tt;
    end %end if

    Vo2tt=(-g*dx2^2) / ( (2*cosd(theta)^2) * (dy2-(dx2*tand(theta))) ) )^(1/2);
    if isreal(Vo2tt)==1
        Vos2(tt)=Vo2tt;
    end %end if
end %end loop through the thetas
%% get the initial velocity measurements
[Vo1_min, vmin1ind]=min(Vos1); % get minimum
thetacr1=thetas(vmin1ind); %critical release angle at minimum release velocity
[Vo2_min, vmin2ind]=min(Vos2);
thetacr2=thetas(vmin2ind);
%now we have the critical release angles, and minimum release velocities
%for both trajectory 1 and 2
%% find the impact velocities
Vo1y=Vo1_min*sind(thetacr1); Vo1x=Vo1_min*cosd(thetacr1); %Vo into x and y components
Vo2y=Vo2_min*sind(thetacr2); Vo2x=Vo2_min*cosd(thetacr2);
t1=dx1/Vo1x; % time based on x speed and dx
t2=dx2/Vo2x;
Vim1y=Vo1y-(g*t1); %impact velocity from equation of motion, only in Y orientation
Vim2y=Vo2y-(g*t2);
Vim1x=Vo1x;
Vim1=(Vo1x^2+Vim1y^2)^(1/2); % get total impact velocity from components
Vim2=(Vo2x^2+Vim2y^2)^(1/2); %
theta_imxy=atan2(-Vim1y/Vim1x); % get the impact angle relative to horizontal
%get the slope
%we calculate a simplified slope using the dx and dy coords of the points
%around it -This is likely not as accurate as a slope value extracted from

```

```

%the dem.
% this section was edited to mandate for direct slope input.
%slope=-atand((dy1+dy2)/(dx1+dx2)); % altered to be positive for below trig
calculations
%% calculate COR values
vcor= Vo2_min/Vim1;
Vo2n = sind(theta_cr2+slope)* Vo2_min ; %normal outbound velocity
Vim1n = Vim1 * sind(theta_imxy-slope); %normal impact Veloticy
ncor=Vo2n/Vim1n ; %normal coefficient of restitution
Vo2t=cosd(theta_cr2+slope)* Vo2_min ; %tangential outbound velocity
Vim1t = Vim1 * cosd(theta_imxy-slope); %tangential impact Veloticy
tcor=Vo2t/Vim1t;
end %end function

```

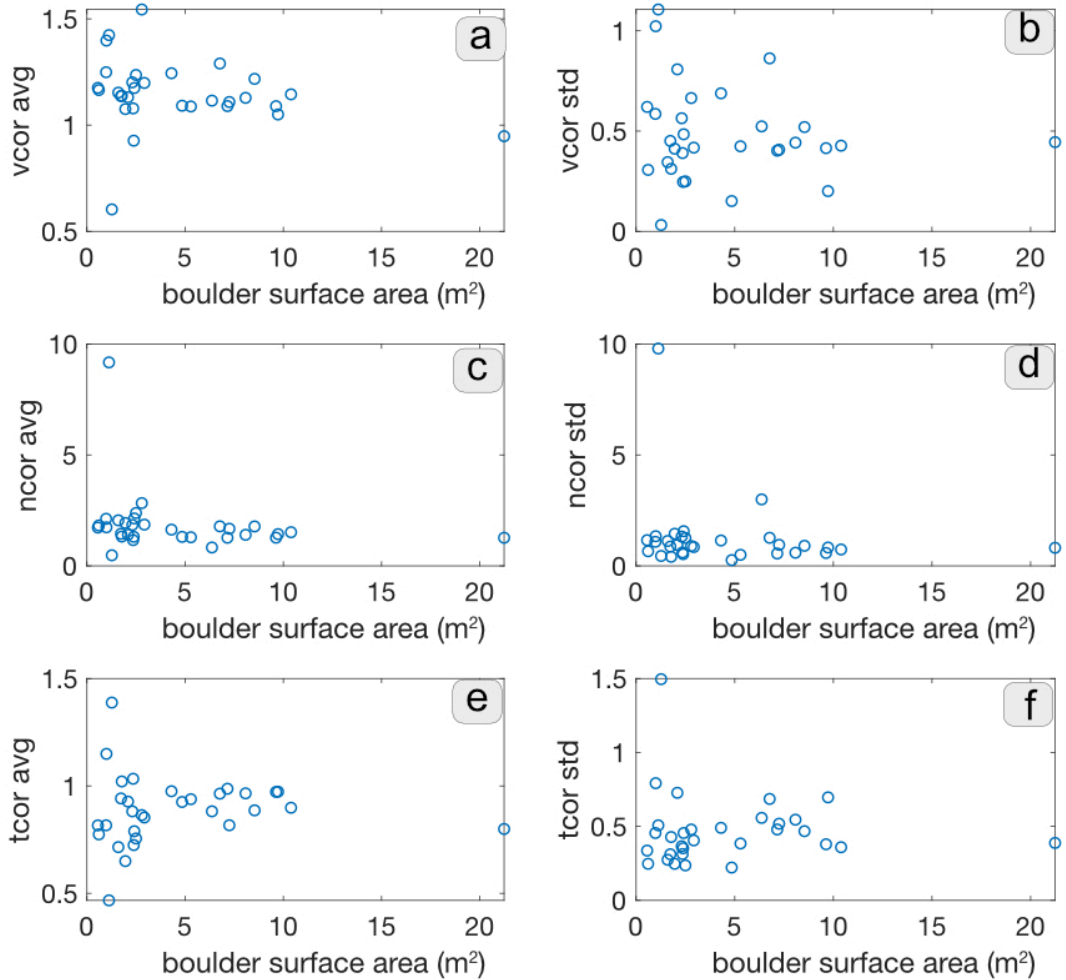


**Figure A6-1:** Comparison of calculated COR values for a specific track to the surface area of the footprint of the boulder which left them. The y-axis of the left column shows the average COR values of each track, and the y-axis of the right column shows the standard deviation of the COR values in each track. Rows separate the total velocity, normal, and tangential components of the COR values.

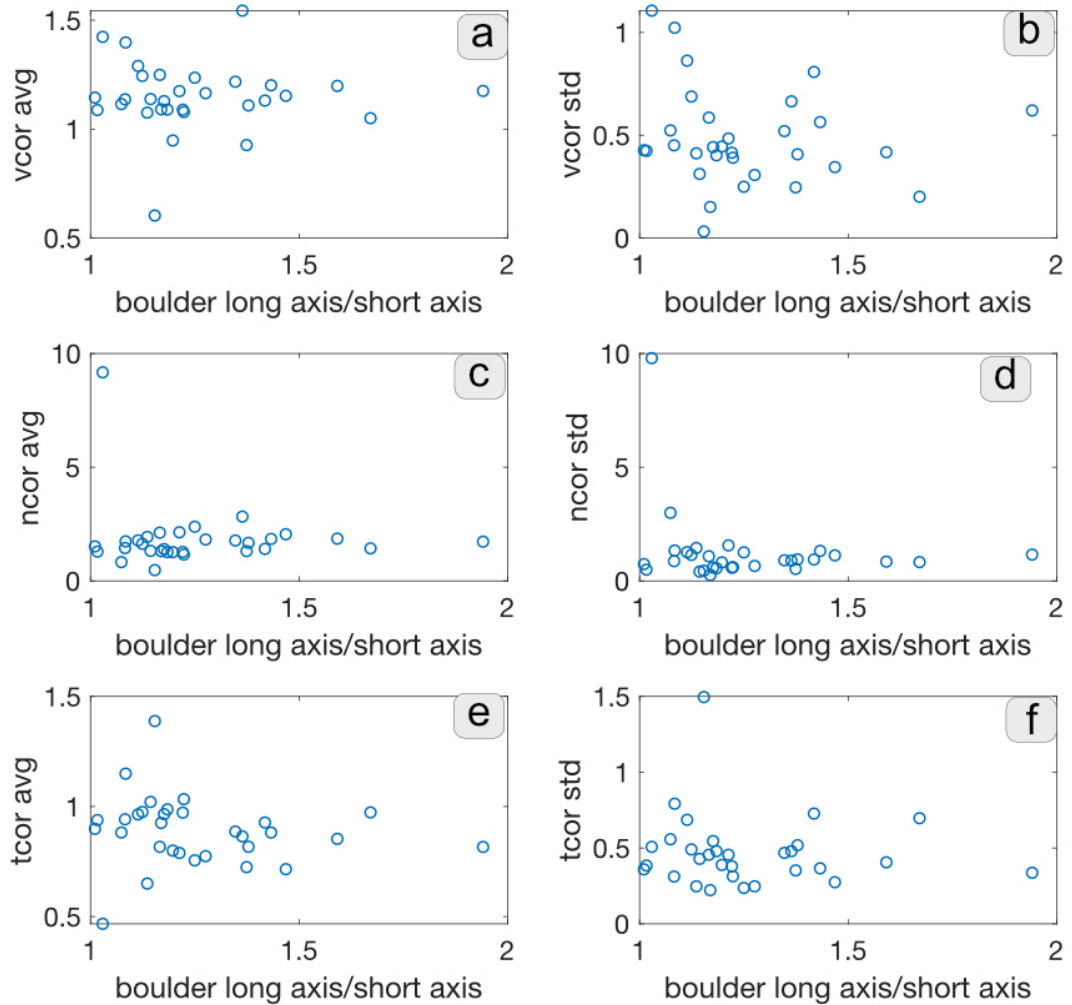


**Figure A6-2 :** Comparison of calculated COR values for a specific track to the “ellipticity” of the boulder that left them. Here “ellipticity” is calculated by dividing the boulder long axis length by the short axis length; a value of 1 is a circular boulder and higher values are more elliptical. The y-axis of the left column shows the average COR values of each track, and the y-axis of the right column shows the standard deviation of the COR values in each track. Rows separate the total velocity, normal, and tangential components of the COR values.

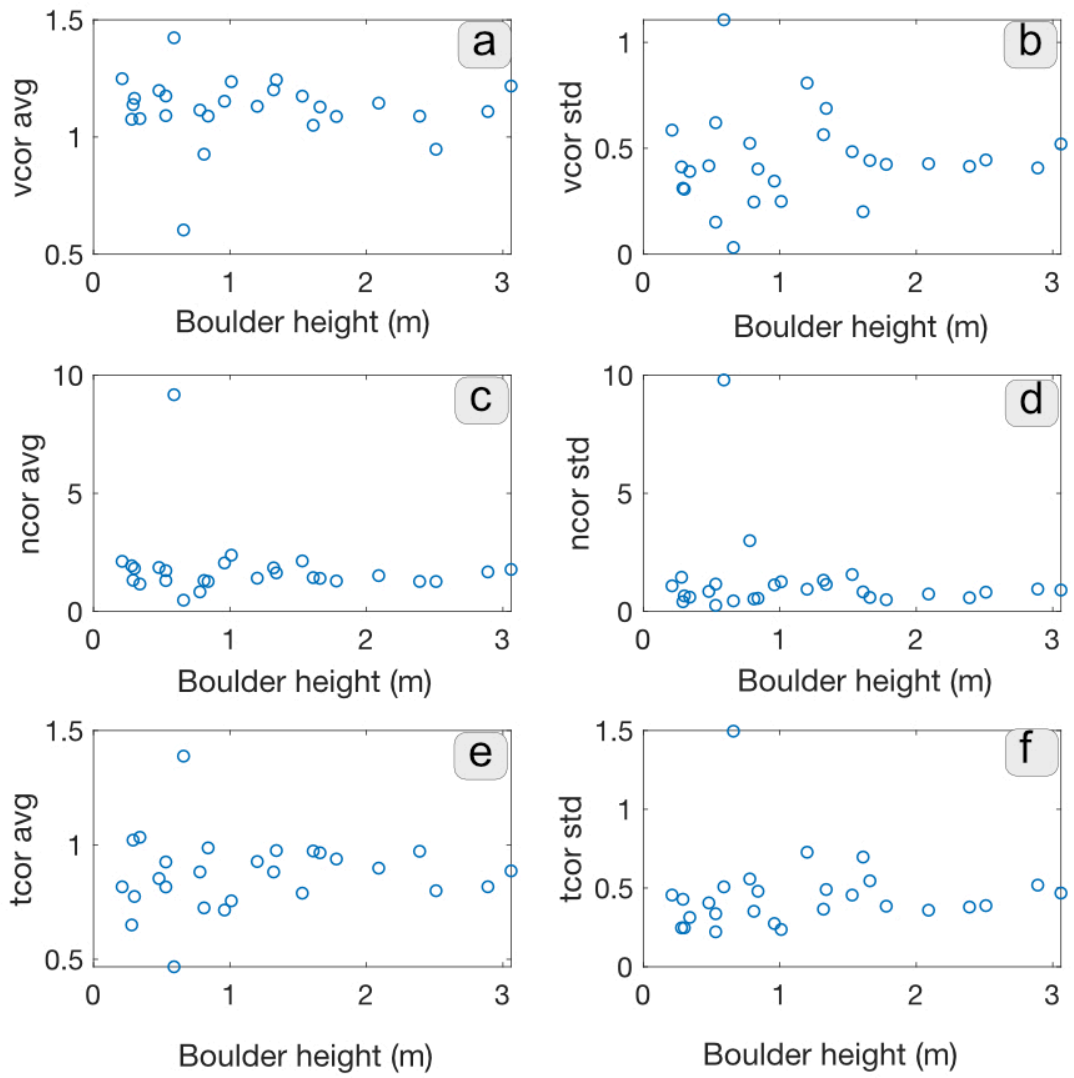


**Figure A6-3:** Comparison of calculated COR values for a specific track to height of the boulder which left them. The height is measured from the drone-based DEM. The y-axis of the left column shows the average COR values of each track, and the y-axis of the right column shows the standard deviation of the COR values in each track. Rows separate the total velocity, normal, and tangential components of the COR values.

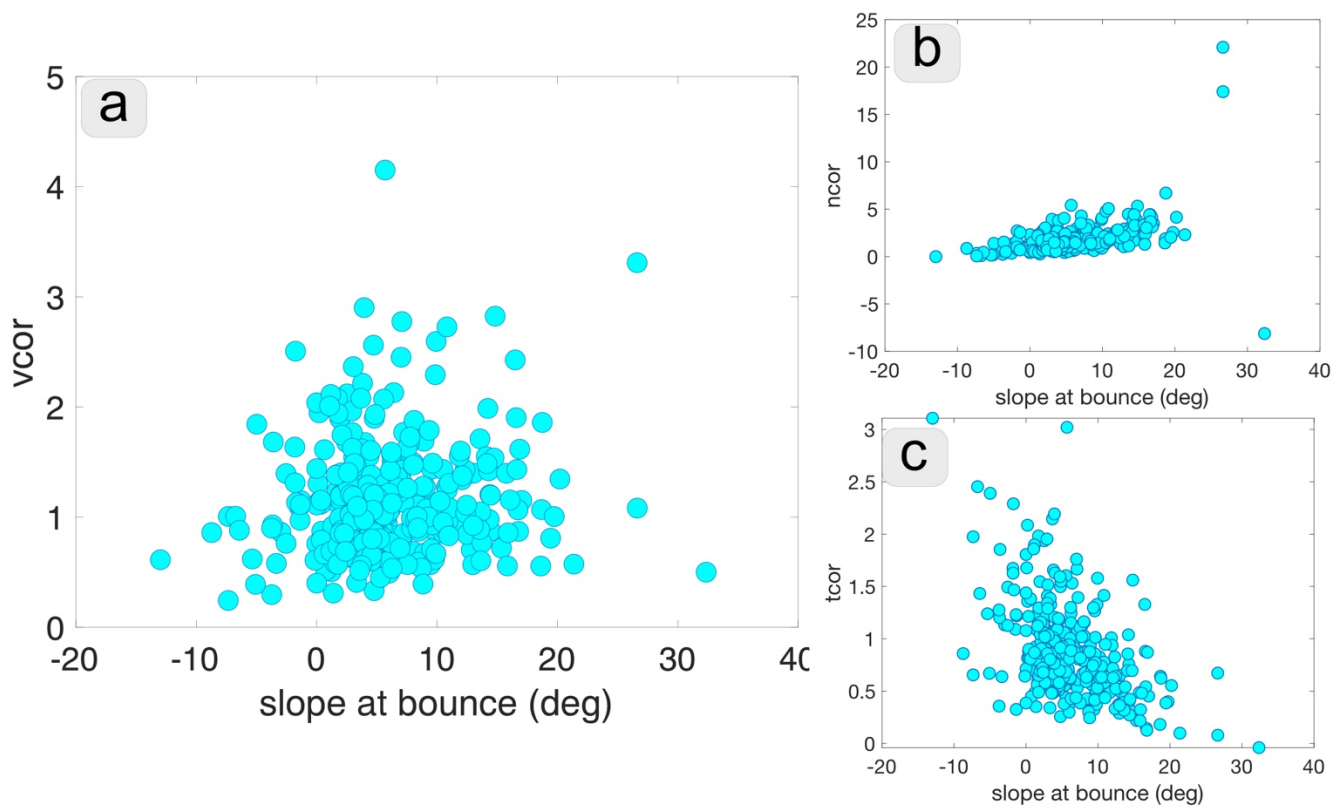


**Figure A6-4** The relationship between the slope at each bounce mark location and the COR values at that location. A) the total velocity COR value ( $\text{COR}_v$ ), there is no strong correlation between  $\text{COR}_v$  and slope ( $R^2=0.0115$ ). B) and C) show relationships between slope and the normal and tangential components of  $\text{COR}_v$ , but that is expected because the slope is used to separate the COR value into its components, and not necessarily indicative of causation.

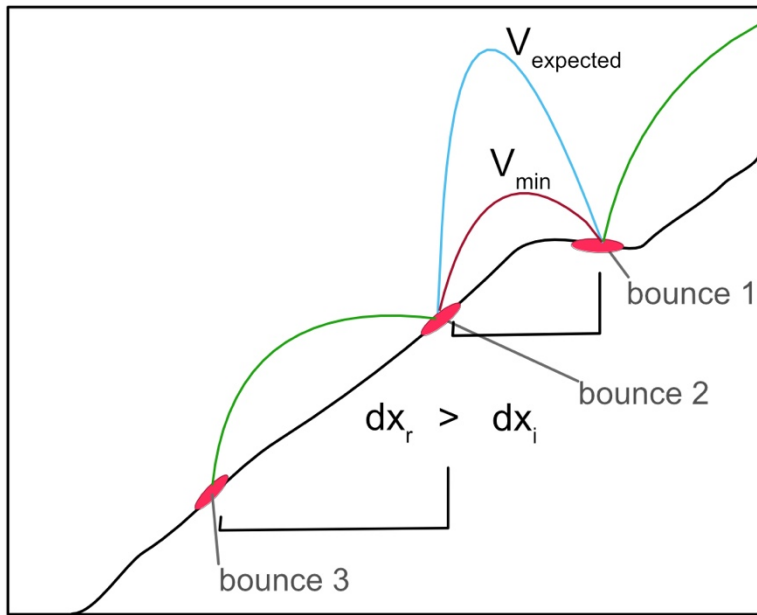


**Figure A6-5** Schematic diagram illustrating how a calculated COR value could be affected by the topography at neighboring bounces. This diagram shows a possible scenario where the expected release angle of the bounce 1 is controlled by the topography, resulting in an inefficient trajectory along the short  $dx_i$  from bounce 1 to bounce 2. In this hypothetical scenario the topography at bounce 1 controls the calculated COR of bounce 2.

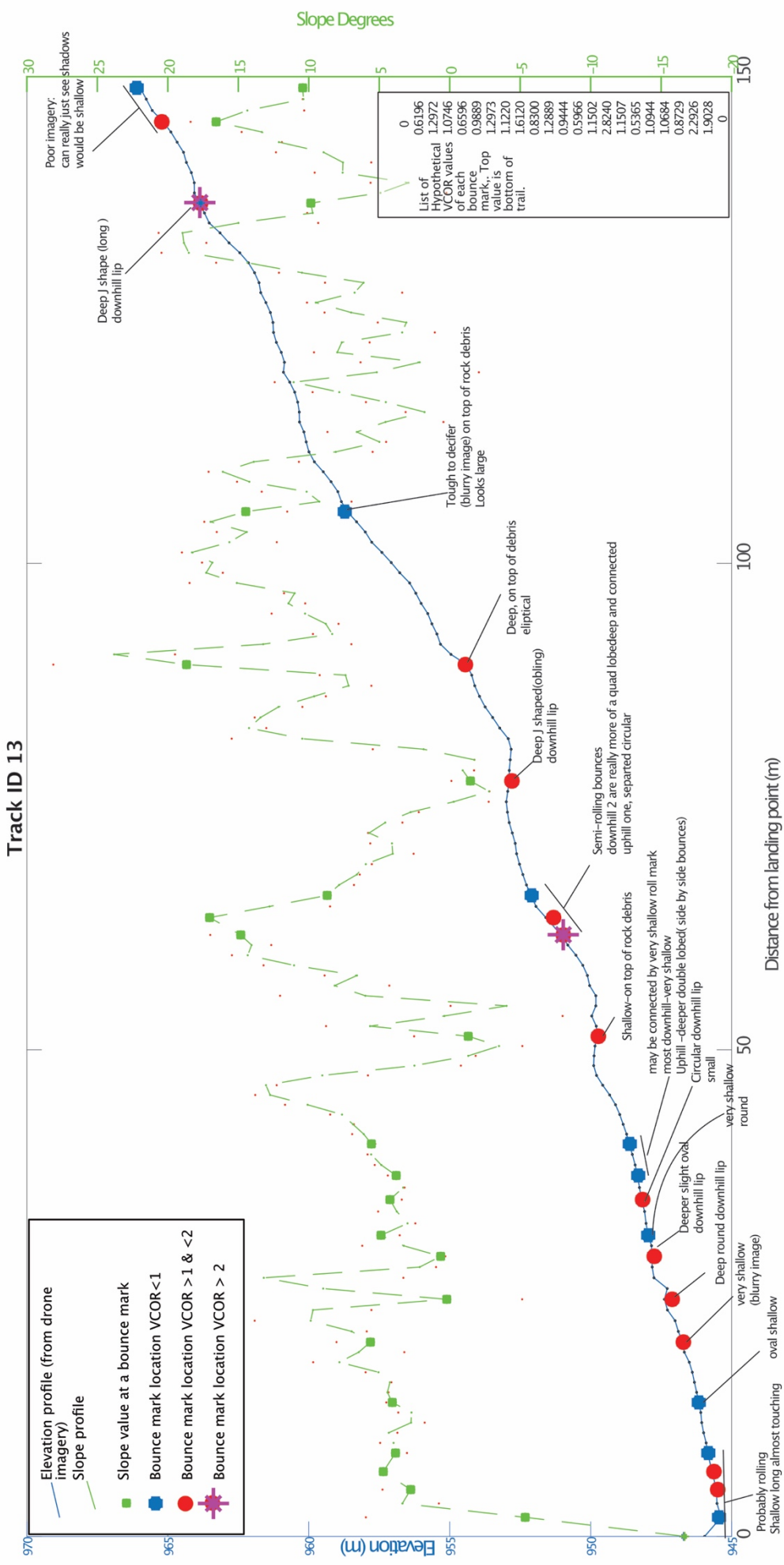


**Figure A6-6** (Previous page) Figure details the profile of a sample bounce track. Profile produced to estimate role of topography of neighboring bounces in controlling the slope. Green line represents the slope, made from a moving average of ~2 m. Blue line is the elevation profile along the path of the bouncing boulder. Bounce mark locations are marked on both the slope and elevation profiles, and on the elevation profile they are colored by COR<sub>V</sub> value COR<sub>V</sub> <1 are blue, COR<sub>V</sub> >1 & <2 are red, and COR<sub>V</sub> >2 are purple asterisks. Also included are brief informal descriptions of the visual style of each bounce mark.

## **REFERENCES**

- Matmon, A., Quade, J., Placzek, C., Fink, D., Copeland, A., & Neilson, J. W. (2015). Seismic origin of the Atacama Desert boulder fields. *Geomorphology*, 231, 28–39.  
<https://doi.org/10.1016/j.geomorph.2014.11.008>
- Placzek, C., Granger, D. E., Matmon, A., Quade, J., & Ryb, U. (2014). Geomorphic process rates in the central atacama desert, Chile: Insights from cosmogenic nuclides and implications for the onset of hyperaridity. *American Journal of Science*, 314(10), 1462–1512.  
<https://doi.org/10.2475/10.2014.03>
- Quade, J., Reiners, P., Placzek, C., Matmon, A., Pepper, M., Ojha, L., & Murray, K. (2012). Seismicity and the strange rubbing boulders of the Atacama desert, Northern Chile. *Geology*, 40(9), 851–854. <https://doi.org/10.1130/G33162.1>
- Sager, C., Airo, A., Arens, F. L., Rabethge, C., & Schulze-Makuch, D. (2020). New types of boulder accumulations in the hyper-arid Atacama Desert. *Geomorphology*, 350, 106897.  
<https://doi.org/10.1016/j.geomorph.2019.106897>
- Saroglou, C., Asteriou, P., Zekkos, D., Tsiambaos, G., Clark, M., & Manousakis, J. (2018). UAV-based mapping, back analysis and trajectory modeling of a coseismic rockfall in Lefkada island, Greece. *Natural Hazards and Earth System Sciences*, 18(1), 321–333.  
<https://doi.org/10.5194/nhess-18-321-2018>

## TABLES

**Table 1 (A1) Boulder fall field locations**

Coordinates reference system is EPSG:4326-WGS 84

Site name	Confirmed?	Study site?	Lat	Lon	Field notes
Chinchilla	yes	yes	-21.09606138	-69.81311513	primary field site
Atajaña	yes	yes	-19.29186154	-70.1504925	
Caleta punta arenas	yes	yes	-21.66354232	-70.1465835	
confirmed stop 25	Yes	no	-22.65965873	-70.26485218	
confirmed stop 23	Yes	no	-22.3354704	-70.24466516	
confirmed stop 2	Yes	no	-21.97917434	-70.17737356	
confirmed stop 4	Yes	no	-21.80527506	-70.13737095	
confirmed stop 5	Yes	no	-21.74009546	-70.14522441	
Confirmed stop 6	Yes	no	-21.72109268	-70.14291526	
confirmed stop 7	Yes	no	-21.70203562	-70.143023	
confirmed stop 8	Yes	no	-21.63405688	-70.12745931	
Confirmed stop 15	Yes	no	-21.19520364	-70.08769518	
confirmed stop 16	Yes	no	-21.06070364	-70.14301279	
Chuculay north	Yes	no	-21.08355776	-69.91249152	
pisagua	Yes	no	-19.57505468	-70.06726856	
satellite 1	no	no	-20.80986684	-70.17759083	
satellite 2	no	no	-19.40292408	-70.22260259	
satellite 3	no	no	-20.34516636	-69.92659289	
satellite 4	no	no	-21.42985859	-70.04275353	
satellite 5	no	no	-21.39839991	-70.0504825	
satellite 6	no	no	-21.35353576	-70.06957838	
satellite 7	no	no	-21.12751015	-69.85552351	

satellite 8	no	no	-20.38728304	-69.94303775	
satellite 9	no	no	-20.04762217	-69.9645997	
satellite 10	no	no	-19.97402612	-69.88860943	
satellite 11	no	no	-19.94354986	-70.02345213	
satellite 12	no	no	-19.7396382	-70.10455282	
satellite 13	no	no	-19.71434948	-69.99348498	
satellite 14	no	no	-19.48656244	-70.12603304	
satellite 15	no	no	-19.41782119	-70.21858937	
satellite 16	no	no	-19.30840006	-70.07159553	

**Table 2 (A3) Field boulder survey**

Boulder ID	Location		Size			Degradation morph.	Apron			Joint s				Hammer test	Weathering			Tracks			
	Lat	Lon	Height (m)	Width (m)	Length (m)	1 to 5	% height	Height (m)	Width (m)	Length (m)	N. Families	Min. Spacing (cm)	Max spacing (cm)	Aperature min (mm)	Aperature max (mm)	1 to 4	Soil min (cm)	Soil max (cm)	degree	Yes no or maybe	
Le1-1	- 21.09372	- 69.806	1.3	2.6	3.4	4	70	0.91	1.5	1.7	3	3	5	1	3	3	2	5	1	no	
Le2-1	- 21.09412	- 69.805 99	1.3	5.1	5.1	3.5	60	0.78	1.2	2.5	2	3	7	1	2	2	2	5	1	no	
Le2-2	-21.0942	- 69.806 11	0.7	2.6	2.6	2	15	0.10 5	0.3 2	0.32	2	2	5	1	3	2	1	1	2	Yes	
Le3-1	- 21.09465	- 69.805 9	1.3	4.2	5.1	2	20	0.26	0.4 5	1.7	3	2	6	1	3	2	3	3	3	yes	
Le3-2	- 21.09474	- 69.806 18	1.4	2.5	3.4	2	10	0.14	0.6	0.8	4	7	8	1	4	1	0	0	1	Yes	
Le3-3	- 21.09475	- 69.805 94	0.4 8	1.7	2.5	2	10	0.04 8	0.04 8	15	40	1	30	35	3	4	1	0	0	1	no
Le3-4	- 21.09475	- 69.806 22	0.6 5	5.9	5.9	4	60	0.39	1.5	2.5	2	3	5	1	5	3	7	7	1	no	
Le4-1	- 21.09486	- 69.806 07	0.5	3.4	4.2	5	100	0.5	0	0	0	0	0	0	0	4	5	10	1	May be	
Le4-2	- 21.09479	- 69.806 13	0.6	3.4	4.2	4	60	0.36	0.8	1.7	0	0	0	0	0	3	3	9	1	no	

Le4-3	- 21.09488	- 69.806 19	0.8 5	2	2.5	2	30	0.25 5	0.2 5	0.64	3	9	10	1	3	2	0	0	3	Yes
Le4-4	- 21.09503	- 69.806 17	1	2.9	2.5	2	15	0.15	0.3 2	0.64	3	15	20	1	70	1	0	0	1	Yes
Le4-5	- 21.09498	- 69.806 31	0.5	3.4	3.4	5	100	0.5	0	0	2	3	7	2	5	3	5	5	1	no
Le4-6	- 21.09512	- 69.805 98	0.5	2.5	3.6	4	66	0.33	0.8	0.8	0	0	0	0	0	1	5	8	1	May be
Le4-7	- 21.09525	- 69.805 81	1.2 4	2.5	3.4	2	48	0.59 52	1	1	2	15	20	1	4	1	0	0	1	no
Le4-8	-21.0952	- 69.805 88	0.7	5.1	3.4	4	70	0.49	0.8	0.8	1	4	7	2	5	2	7	9	1	No
Le4-9	-21.0952	- 69.805 92	1.5	5.9	5.9	3	50	0.75	0.6 4	2.5	0	0	0	0	0	1	1	7	1	May be
Le4-10	- 21.09519	- 69.806 02	1	2.5	2.5	2	10	0.1	0.8	0.8	2	2	5	1	3	2	6	7	1	no
Le4-11	- 21.09523	- 69.806 05	1.1	6.4	9.6	2	30	0.33	1.5	4.1	2	1	3	3	5	2	4	6	1	no
Le4-12	- 21.09525	- 69.806 44	0.7	5.1	5.1	2	40	0.28	1.7	2.5	1	10	12	2	3	1	7	7	1	no
Le4-13	- 21.09528	- 69.806 48	0.5 5	1	1	1	10	0.05 5	0	0.3	0	0	0	0	0	1	0	0	1	no
Le4-14	- 21.09539	- 69.806 47	1	4.2	4.2	3	55	0.55	0.8	1.7	0	0	0	0	0	2	0	0	1	yes
Ld5-1	-21.0954	- 69.806 19	1.3	0.2	8.5	3	50	0.65	3.1	5.1	3	10	35	2	4	3	1	2	1	no

Le5-1	- 21.09528	- 69.806 28	0.5	3.4	4.2	3	60	0.3	0.4 8	1.7	2	10	12	1	2	2	2	2	1	no
Le5-2	- 21.09526	- 69.806 14	0.6 5	3.4	5.1	3	50	0.32 5	0.8	3.4	2	5	12	1	2	2	2	2	1	no
Le5-3	- 21.09555	- 69.805 91	0.2	2.5	3.4	4	65	0.13	0.3 2	0.69	0	0	0	0	3	3	10	1	no	
Le5-4	- 21.09535	- 69.805 88	1.2	3.4	4.2	2	50	0.6	1	0.4	2	3	14	2	3	2	0	0	1	Yes
Le5-5	- 21.09536	- 69.805 84	0.5	1.7	1.7	2	20	0.1	32	1	0	0	0	0	2	1	2	1	may be	
Le5-6	- 21.09548	- 69.805 85	1.7	5.1	6.8	2	25	0.42 5	0.4	1	3	2	20	2	7	2	2	2	1	May be
Le5-7	- 21.09548	- 69.805 98	0.5	3.4	3.6	2	20	0.1	0.3 2	0.8	0	0	0	0	3	3	3	1	yes	
Le5-8	- 21.09539	- 69.806 04	0.5	1.7	2	2	10	0.05	0	0.64	1	16	16	1	1	0	0	1	May be	
Le5-9	- 21.09537	- 69.806 22	0.3 2	1	0.64	2	20	0.06 4	0.5	0.32	1	15	20	2	10	2	4	4	1	May be
Le5-10	- 21.09554	- 69.806 05	0.5	4.2	3.4	4	80	0.4	2.5	0.7	0	0	0	0	1	0	0	1	no	
Le5-11	- 21.09536	- 69.806 08	0.5	1.7	1.7	2	30	0.15	0	0.32	0	0	0	0	3	0	0	3	no	
Le5-12	-21.0954	- 69.806 05	0.6 4	1.5	1.6	2	10	0.06 4	0.5	0.32	1	15	20	2	2	4	0	0	1	yes
Le5-13	- 21.09552	- 69.806 06	1	2.5	2.5	2	10	0.1	0.2	0.5	1	1	4	1	3	2	0	0	1	may be

Le5-14	-21.0955	-69.80601	1.15	3.1	2.5	2	15	0.1725	0.32	0.64	3	15	2	10	20	2	0	0	1	yes
Le5-15	-21.09558	-69.80584	1.4	5.9	5.1	4	60	0.84	0.32	0.64	1	20	25	1	70	2	0	0	1	no
Le5-16	-21.09564	-69.80589	1.8	5.1	8.5	2	20	0.36	0.8	3.4	2	20	30	1	6	2	1	2	1	yes
Le5-17	-21.09557	-69.80575	0.5	1.7	0.8	1	0	0	0	0	0	0	0	0	1	0	0	1	yes	
Le5-18	-21.09565	-69.80586	1	1.7	2.5	2	10	0.1	0	0.85	0	0	0	0	0	2	0	0	1	May be
Le5-19	-21.09564	-69.80606	0.5	5.1	2.5	2	20	0.1	0.4	1.7	0	0	0	0	0	1	0	0	1	no
Le5-20	-21.09559	-69.80596	0.6	1.25	0.8	1	0	0	0	0	0	0	0	0	0	1	0	0	1	yes
Le5-21	-21.09553	-69.8061	1.3	3.4	4.2	2	20	0.26	0.6	1.7	1	5	18	2	5	2	1	2	1	no
Le5-22	-21.09543	-69.80608	0.64	1.7	1.7	2	10	0.064	0.16	0.4	0	0	0	0	0	2	1	2	1	no
Le5-23	-21.09561	-69.80619	0.8	3.4	1.7	2	30	0.24	0	0.7	0	0	0	0	0	1	0	0	1	no
Le5-24	-21.09563	-69.80627	1	1.7	1.7	2	20	0.2	0.5	0.48	0	0	0	0	0	1	0	0	1	may be
Le5-25	-21.09561	-69.80634	3.6	8.5	9.3	2	35	1.26	1.7	3.4	0	0	0	0	0	3	0	0	2	ct
Hd5-1	-21.09687	-69.81774	1.3	2.5	1.7	1	0	0	0	0	0	0	0	0	0	1	0	0	3	ct

Hd5-2	-21.09682	-69.81749	1.2	2.5	1.7	1	10	0.12	0.8	1.15	0	0	0	0	0	1	0	0	4	ct
Hd5-3	-21.09675	-69.81751	0.3	0.8	1.2	2	8	0.024	0.1	0.2	2	2	5	18	35	2	0	0	0	ct
Hd5-4	-21.09669	-69.81752	0.45	0.36	0.5	1	0	0	0	0	0	0	0	0	0	1	0	0	0	may be
Hd5-5	-21.09672	-69.81758	0.45	1.7	1.6	1	0	0	0	0	0	0	0	0	0	1	0	0	0	yes
Hd5-6	-21.09665	-69.81753	0.55	1	0.64	1	0	0	0	0	0	0	0	0	0	1	0	0	0	Yes
Hd5-7	-21.09683	-69.81783	0.5	1.5	1	1	5	0.025	0.16	0	0	0	0	0	0	2	0	0	0	no
Hd5-8	-21.0968	-69.81786	0.56	1.3	0.8	1	0	0	0	0	0	0	0	0	0	1	0	0	0	May be
Hd5-9	-21.09678	-69.81787	0.64	3.2	3.4	4	65	0.416	0.32	1	1	1	40	2	3	3	4	7	0	ct
Hd5-10	-21.0967	-69.81789	0.8	0.8	0.8	1	0	0	0	0	0	0	0	0	0	2	0	0	0	ct
Hd5-11	-21.0967	-69.81784	0.7	0.5	1.7	1	0	0	0	0	0	0	0	0	0	1	0	0	0	no
Hd5-12	-21.09665	-69.81773	0.65	2.7	1.5	1	0	0	0	0	0	0	0	0	0	1	0	0	0	no
Hd5-13	-21.09667	-69.81777	0.4	1	0.7	1	0	0	0	0	0	0	0	0	0	1	0	0	0	no
Hd5-14	-21.0966	-69.81766	0.75	1.7	2.5	2	0	0	0	0	0	0	0	0	0	1	0	0	0	no

Hd5-15	-21.0966	-69.81762	0.9	2.5	1.7	1	0	0	0	0	0	0	0	0	3	0	0	3	no	
Hd5-16	-21.09656	-69.81766	1.2	1.25	2	2	10	0.12	0.2	0.35	1	5	5	1	3	2	1	2	2	May be
Hd5-17	-21.09657	-69.81773	1.3	4.2	3.6	2	10	0.13	0.48	0.8	0	0	0	0	0	3	3	3	1	no
Hd5-18	-21.0966	-69.81777	0.9	1.7	1.5	1	0	0	0	0	0	0	0	0	1	0	0	1	May be	
Hd5-19	-21.0966	-69.8178	0.7	1.7	1.25	1	0	0	0	0	0	0	0	0	1	0	0	1	no	
Hd5-20	-21.0966	-69.81787	0.4	0.8	0.9	1	0	0	0	0	0	0	0	0	0	1	0	0	1	no
Hd4-1	-21.09654	-69.8179	0.35	1.7	0.4	1	0	0	0	0	0	0	0	0	1	0	0	1	no	
Hd4-2	-21.09655	-69.81778	0.5	3.6	2.5	2	20	0.1	0.22	0.6	1	1	12	1	10	2	4	4	1	no
Hd4-3	-21.09655	-69.81783	0.45	0.9	0.6	1	0	0	0	0	0	0	0	0	1	0	0	1	May be	
Hd4-4	-21.09653	-69.81771	0.5	2.5	2.5	2	15	0.075	0.38	0.7	1	1	6	1	3	3	0	0	4	no
Hd4-5	-21.09651	-69.81771	0.75	1.7	1	2	10	0.075	0.2	0.5	0	0	0	0	0	2	0	0	1	Yes
Hd4-6	-21.0965	-69.81766	0.6	0.7	1	1	0	0	0	0	0	0	0	0	0	1	0	0	1	no
Hd4-7	-21.09651	-69.81761	0.6	5.1	4.3	3	50	0.3	0.8	1.7	0	0	0	0	0	4	6	8	1	no

Hd4-8	-21.09645	-69.81748	0.4	1.7	1.7	4	60	0.24	0.3	0.45	0	0	0	0	0	2	0	0	3	no
Hd4-9	-21.09639	-69.81744	0.64	2.5	2.5	2	25	0.16	0.32	0.32	1	5	8	1	10	3	0	0	4	no
Hd4-10	-21.09637	-69.81748	0.55	1.3	1.3	1	0	0	0	0	2	2	7	1	5	3	0	0	3	May be
Hd4-11	-21.09624	-69.81753	0.4	0.6	0.6	1	0	0	0	0	2	5	9	1	3	1	0	0	1	no
Hd4-12	-21.09624	-69.81765	0.7	0.9	1	1	0	0	0	0	0	0	0	0	0	1	0	0	1	no
Hd4-13	-21.09623	-69.81765	0.64	1.5	1.7	1	0	0	0	0	0	0	0	0	0	1	1	2	1	no
Hd4-14	-21.09627	-69.8176	0.6	3.4	1.7	2	20	0.12	0.32	1.7	0	0	0	0	0	2	0	0	1	no
Hd4-15	-21.09624	-69.81767	0.65	3.4	4.2	2	25	0.1625	1.2	1.7	0	0	0	0	0	4	0	0	4	no
Hd4-16	-21.09627	-69.8177	0.6	1	0.4	1	0	0	0	0	0	0	0	0	0	1	0	0	1	no
Hd4-17	-21.0963	-69.81775	0.7	1.2	2	2	30	0.21	0.32	0.74	0	0	0	0	0	4	0	0	4	no
Hd4-18	-21.09632	-69.81785	0.5	1.4	0.6	1	0	0	0	0	0	0	0	0	0	1	0	0	1	no
Hd4-19	-21.09627	-69.81783	1	3.4	3.4	2	35	0.35	0.32	1.8	0	0	0	0	0	1	0	0	1	Yes
Hd4-20	-21.09626	-69.8179	0.64	0.4	0.65	2	0	0	0	0	0	0	0	0	0	2	0	0	1	no

Hd4-21	-21.09621	-69.81781	0.58	1.7	1.6	1	0	0	0	0	1	15	15	1	2	1	0	0	1	ct
Hd4-22	-21.09624	-69.81776	0.75	0.7	0.4	2	10	0.075	0.2	0	0	0	0	0	0	3	0	0	1	no
Hd4-23	-21.09622	-69.81771	1	2.5	2.5	2	20	0.2	0.3	1.5	2	12	36	1	10	1	0	0	1	may be
Hd4-24	-21.09618	-69.81771	1.7	4.7	4.2	2	5	0.085	0.32	1.2	0	0	0	0	0	3	6	6	1	no
Hd4-25	-21.09612	-69.81761	1	1.7	3	2	10	0.1	0.32	1.2	0	0	0	0	0	2	0	0	3	yes
Hd4-26	-21.0961	-69.81792	0.64	1	1	1	0	0	0	0	0	0	0	0	0	1	0	0	2	no
Hd3-1	-21.09602	-69.81794	0.5	3.4	3.6	3	50	0.25	0.32	4.2	0	0	0	0	0	1	0	0	1	no
Hd3-2	-21.09602	-69.8179	0.6	3.4	4.2	3	50	0.3	0.8	1.5	0	0	0	0	0	4	0	0	1	no
Hd3-3	-21.09603	-69.81771	0.5	2.5	2.5	2	10	0.05	0.5	1.5	0	0	0	0	0	2	0	0	1	no
Hd3-4	-21.09592	-69.81789	0.5	3.4	5.1	4	80	0.4	0.8	1.7	0	0	0	0	0	4	7	8	4	no
Hd3-5	-21.09589	-69.81785	0.45	3.4	3.4	4	80	0.36	1.7	0.8	0	0	0	0	0	4	0	0	1	no
Hd3-6	-21.09588	-69.81783	1	3.4	3.4	2	25	0.25	0.2	1.5	0	0	0	0	0	2	0	0	1	no
Hd3-7	-21.0959	-69.81778	0.4	2.5	2.5	4	85	0.34	0.3	0.3	0	0	0	0	0	4	7	9	3	no

Hd3-8	-21.09587	-69.81751	0.38	2.5	3.4	4	90	0.342	1.7	0.32	0	0	0	0	0	4	4	5	4	no
Hd3-9	-21.09583	-69.81755	0.4	4.3	3.4	4	90	0.36	0.75	1.7	0	0	0	0	0	2	0	0	1	no
Hd3-10	-21.09579	-69.81745	0.7	3.4	3	3	50	0.35	1.3	0.8	0	0	0	0	0	4	0	0	1	no
Hd3-11	-21.09574	-69.81747	1	2.5	3.4	2	30	0.3	0.3	0.8	0	0	0	0	0	4	0	0	1	no
Hd3-12	-21.09577	-69.81755	1.2	3.4	4.3	5	0	0	0	0	0	0	0	0	0	4	7	9	4	no
He2-1			3.6	8.5	9.3	2	5	0.18	1	2.5	0	0	0	0	0	2	0	0	1	yes
Hd3-13	-21.09578	-69.81765	0.9	4.2	3.4	2	30	0.27	0.8	1.7	0	0	0	0	0	3	3	4	4	ct
Hd3-14	-21.09578	-69.81772	0.4	3.6	3.6	4	80	0.32	1.7	0.32	0	0	0	0	0	2	0	0	1	ct
Hd3-15	-21.09582	-69.81784	0	6.8	6	4	80	0	3.4	3.4	1	2	6	1	10	3	7	8	1	no
Hd3-16	-21.09576	-69.81782	0.65	2.5	2.5	3	50	0.325	0.6	4.6	0	0	0	0	0	2	0	0	1	no
Hd3-17	-21.09573	-69.81783	0.45	3.4	3.4	4	60	0.27	1.7	0.8	0	0	0	0	0	4	8	10	4	no
Hd3-18	-21.09569	-69.81779	0.6	3.8	3.8	4	60	0.36	0.8	1.7	0	0	0	0	0	4	3	4	3	no
Hd3-19	-21.09568	-69.81786	0.38	1.7	2.5	5	0	0	0	0	0	0	0	0	0	4	3	9	4	no
Hd3-20	-21.09565	-69.81757	0.7	4.2	5.1	4	70	0.49	5.1	3.4	0	0	0	0	0	4	3	7	1	no

Hd3-21	-21.09567	-69.81748	0.6	2.5	3.4	4.5	80	0.48	1.7	1.7	0	0	0	0	0	4	8	9	1	no
Hd3-22			0.64	4.2	5.1	3	60	0.384	1.2	1.7	0	0	0	0	0	3	7	9	1	no
Hd2-1	-21.09556	-69.81753	0.3	2.5	3.4	5	100	0.3	2.5	3.4	0	0	0	0	0	4	4	8	4	no
Hd2-2	-21.09557	-69.81759	0.2	1.2	0.8	5	100	0.2	1.2	0.8	0	0	0	0	0	4	5	10	4	no
Hd2-3	-21.09555	-69.8179	0.35	4.2	4.5	3	50	0.175	2.5	0.8	0	0	0	0	0	3	6	7	3	no
Hd2-4	-21.09549	-69.81783	0.3	3.4	3.4	4	60	0.18	1.7	0.8	0	0	0	0	0	4	3	12	3	no
Hd2-5	-21.09545	-69.81788	1.1	4.2	1.2	2	5	0.055	0.4	0.65	2	1	4	2	5	2	0	0	2	Yes
Hd1-1	-21.0951	-69.81746	0.5	3.4	5.1	4	80	0.4	1.7	0.8	0	0	0	0	0	4	5	6	1	no
Hd1-2	-21.09476	-69.81754	0.65	5.1	6.8	4	60	0.39	0.8	4.2	0	0	0	0	0	2	2	8	3	Yes
Hd-1-1	-21.09419	-69.81801	1	5.9	6.8	4	65	0.65	2.4	1.5	0	0	0	0	0	3	1	4	1	may be
Bf4-1	-21.09821	-69.83374	0.3	0.5	0.6	1	0	0	0	0	0	0	0	0	0	1	0	0	1	no
Bf4-2	-21.09783	-69.83363	0.5	1.7	0.8	1	0	0	0	0	0	0	0	0	0	1	0	0	1	no
Bf4-3	-21.09797	-69.8337	0.47	0.5	0.5	1	0	0	0	0	0	0	0	0	0	1	0	0	1	no
Bf4-4	-21.09805	-69.8336	0.32	1.7	2.1	2	10	0.032	0.8	0.2	0	0	0	0	0	4	0	0	1	ct

Bf4-5	- 21.09784	- 69.833 52	0.3	1	0.7	1	0	0	0	0	0	0	0	0	1	0	0	1	no
Bf3-1	- 21.09756	- 69.833 42	0.3 6	0.9	0.8	1	0	0	0	0	0	0	0	0	2	0	0	1	no
Bf3-2	- 21.09761	- 69.833 56	0.6 4	1	1.2	1	0	0	0	0	0	0	0	0	1	0	0	1	no
Bf3-3	- 21.09759	- 69.833 58	0.5	0.8	0.6	1	0	0	0	0	0	0	0	0	1	0	0	1	no
Bf3-4	- 21.09732	- 69.833 46	0.3 5	0.6 5	0.5	1	0	0	0	0	0	0	0	0	1	0	0	1	no
Bf2-1	- 21.09719	- 69.833 47	0.3	2	0.8	1	0	0	0	0	0	0	0	0	1	0	0	1	no
Bf2-2	- 21.09713	- 69.833 44	0.5	2.3	0.8	1	0	0	0	0	0	0	0	0	1	0	0	1	ct
Bf2-3	- 21.09704	- 69.833 36	0.3 2	2.5	0.8	1	0	0	0	0	0	0	0	0	1	0	0	1	ct
Bf2-4	- 21.09704	- 69.833 31	0.5	0.8	1.7	1	0	0	0	0	0	0	0	0	1	0	0	1	ct
Bf1-1	-21.0969	- 69.833 34	0.3	2.1	1.2	1	0	0	0	0	0	0	0	0	1	0	0	1	May be
Bf1-2	- 21.09686	- 69.833 37	1	1.7	1.3	1	0	0	0	0	0	0	0	0	1	0	0	1	no
Bf1-3	- 21.09681	- 69.833 39	0.2 8	0.3 3	0.65	1	0	0	0	0	0	0	0	0	1	0	0	1	no
Bf1-1	- 21.09542	- 69.833 54	0.3 7	0.4 2	0.4	1	0	0	0	0	0	0	0	0	1	0	0	1	no

Bf-1-2	-	21.09504	-	69.833 53	0.6	1.2	0.8	1	0	0	0	0	0	0	0	0	1	0	0	1	no
Chuc ulay D			1.5	5.7	6.8	2	25	0.37 5	1.7	0.65	0	0	0	0	0	0	3	0	0	1	Yes
Chuc ulay B			0.8	3	1.8	2	10	0.08	0.8	0.6	0	0	0	0	0	0	2	0	0	1	Yes
Chuc ulay C			0.5	5.1	5.1	5	100	0.5	5.1	5.1	0	0	0	0	0	0	2	2	3	2	no
Chuc ulay E			0.6 5	4.2	5.1	4	60	0.39	0.9	1.7	0	0	0	0	0	0	3	7	10	2	no

**Table 3(A6): Bounce Mark information**

A space delimited text list

```
# (1)track number (2)x UTM 19s (3)y UTM 19s (4)dx2 (5)dy2 (6)vcor (7)ncor (8)tcor
1 4.150824e+05 7.666998e+06 0.000 0.000 0.000 0.000 0.000
1 4.150842e+05 7.666995e+06 3.128 0.380 2.216 1.950 2.524
1 4.150847e+05 7.666995e+06 0.777 0.060 0.592 0.569 0.616
1 4.150856e+05 7.666992e+06 2.499 0.101 1.636 1.567 1.712
1 4.150859e+05 7.666991e+06 0.964 -0.008 1.116 1.110 1.122
1 4.150862e+05 7.666991e+06 0.790 0.022 0.514 0.532 0.495
1 4.150868e+05 7.666988e+06 3.009 -0.067 1.962 2.027 1.907
1 4.150870e+05 7.666987e+06 0.830 0.069 1.069 1.034 1.110
1 4.150872e+05 7.666986e+06 0.761 -0.027 0.578 0.552 0.602
1 4.150875e+05 7.666984e+06 2.319 0.120 1.106 0.944 1.270
1 4.150881e+05 7.666982e+06 2.423 0.473 0.765 0.531 1.066
1 4.150895e+05 7.666975e+06 7.059 2.450 1.069 0.806 1.436
1 4.150916e+05 7.666963e+06 11.631 3.444 4.151 2.975 6.185
1 4.150919e+05 7.666962e+06 0.000 0.000 0.000 0.000 0.000
2 4.151091e+05 7.667051e+06 0.000 0.000 0.000 0.000 0.000
2 4.151131e+05 7.667050e+06 4.219 -2.201 0.761 0.928 0.685
2 4.151172e+05 7.667047e+06 5.063 0.698 1.329 1.176 1.507
2 4.151190e+05 7.667043e+06 3.664 0.398 1.640 1.474 1.835
2 4.151197e+05 7.667042e+06 1.616 0.102 0.451 0.425 0.479
2 4.151240e+05 7.667034e+06 8.974 0.515 0.696 0.676 0.717
2 4.151297e+05 7.667015e+06 20.195 0.583 0.809 0.664 0.950
2 4.151381e+05 7.666976e+06 0.000 0.000 0.000 0.000 0.000
3 4.150160e+05 7.667072e+06 0.000 0.000 0.000 0.000 0.000
3 4.150149e+05 7.667070e+06 1.962 -1.249 0.620 0.845 0.523
3 4.150139e+05 7.667067e+06 2.849 0.044 1.297 1.247 1.346
3 4.150139e+05 7.667066e+06 1.849 0.135 1.075 0.980 1.175
3 4.150137e+05 7.667064e+06 1.911 0.199 0.660 0.617 0.708
3 4.150136e+05 7.667059e+06 5.200 0.338 0.989 0.907 1.078
3 4.150134e+05 7.667052e+06 6.195 0.546 1.297 1.188 1.420
3 4.150128e+05 7.667048e+06 4.400 0.397 1.122 1.005 1.246
3 4.150124e+05 7.667044e+06 4.415 0.636 1.612 1.403 1.864
3 4.150123e+05 7.667041e+06 2.165 0.214 0.830 0.775 0.893
3 4.150123e+05 7.667038e+06 3.662 0.199 1.289 1.222 1.360
3 4.150124e+05 7.667035e+06 2.478 0.155 0.944 0.867 1.028
3 4.150124e+05 7.667032e+06 3.245 0.301 0.597 0.541 0.658
```

3 4.150121e+05 7.667021e+06 11.062 1.114 1.150 1.041 1.267  
 3 4.150122e+05 7.667011e+06 10.412 1.241 2.824 2.486 3.184  
 3 4.150124e+05 7.667009e+06 1.784 0.347 1.151 0.870 1.465  
 3 4.150126e+05 7.667007e+06 2.282 0.777 0.536 0.523 0.554  
 3 4.150124e+05 7.666995e+06 11.758 0.700 1.094 0.991 1.201  
 3 4.150137e+05 7.666983e+06 11.956 1.651 1.068 0.836 1.333  
 3 4.150151e+05 7.666967e+06 15.724 4.280 0.873 0.736 1.062  
 3 4.150182e+05 7.666936e+06 31.705 5.114 2.293 1.956 2.698  
 3 4.150198e+05 7.666927e+06 8.346 1.375 1.903 1.606 2.224  
 3 4.150204e+05 7.666924e+06 0.000 0.000 0.000 0.000 0.000  
 4 4.149526e+05 7.667092e+06 0.000 0.000 0.000 0.000 0.000  
 4 4.149563e+05 7.667087e+06 6.409 -1.238 1.025 1.138 0.944  
 4 4.149575e+05 7.667082e+06 5.378 0.354 1.237 1.174 1.307  
 4 4.149595e+05 7.667078e+06 3.882 0.131 1.262 1.208 1.315  
 4 4.149598e+05 7.667076e+06 2.733 0.220 0.878 0.815 0.949  
 4 4.149613e+05 7.667072e+06 4.047 0.214 0.848 0.804 0.896  
 4 4.149640e+05 7.667066e+06 6.271 0.350 0.907 0.875 0.941  
 4 4.149680e+05 7.667059e+06 8.481 0.438 1.384 1.292 1.482  
 4 4.149697e+05 7.667054e+06 4.930 0.279 1.380 1.315 1.447  
 4 4.149706e+05 7.667051e+06 2.984 0.257 0.674 0.584 0.774  
 4 4.149734e+05 7.667044e+06 8.097 1.001 0.843 0.763 0.934  
 4 4.149793e+05 7.667031e+06 14.348 1.528 1.191 1.070 1.329  
 4 4.149838e+05 7.667019e+06 12.353 1.161 2.119 1.907 2.420  
 4 4.149850e+05 7.667017e+06 2.648 -0.350 0.389 0.309 0.465  
 4 4.149923e+05 7.667001e+06 0.000 0.000 0.000 0.000 0.000  
 5 4.150354e+05 7.667031e+06 0.000 0.000 0.000 0.000 0.000  
 5 4.150353e+05 7.667028e+06 3.039 -1.141 0.900 1.128 0.775  
 5 4.150350e+05 7.667025e+06 2.775 0.180 2.077 1.943 2.238  
 5 4.150348e+05 7.667025e+06 0.649 -0.036 0.505 0.503 0.506  
 5 4.150350e+05 7.667022e+06 2.377 -0.031 0.859 0.830 0.889  
 5 4.150349e+05 7.667019e+06 3.351 0.178 1.553 1.402 1.698  
 5 4.150349e+05 7.667017e+06 1.849 0.433 1.346 0.931 1.817  
 5 4.150353e+05 7.667015e+06 1.999 0.908 1.066 0.868 1.399  
 5 4.150344e+05 7.667012e+06 3.146 0.446 1.674 1.446 1.946  
 5 4.150345e+05 7.667011e+06 1.468 0.186 0.822 0.767 0.887  
 5 4.150348e+05 7.667008e+06 2.606 0.144 0.927 0.897 0.961  
 5 4.150346e+05 7.667005e+06 3.289 0.089 0.944 0.898 0.990  
 5 4.150349e+05 7.667001e+06 4.053 0.268 1.425 1.294 1.553  
 5 4.150346e+05 7.666998e+06 2.560 0.472 1.116 0.930 1.342  
 5 4.150351e+05 7.666995e+06 2.931 0.505 0.568 0.538 0.603

5	4.150365e+05	7.666984e+06	11.554	0.781	1.769	1.616	1.916
5	4.150380e+05	7.666979e+06	4.844	0.993	1.859	1.452	2.310
5	4.150380e+05	7.666977e+06	2.442	0.878	0.556	0.468	0.676
5	4.150425e+05	7.666964e+06	0.000	0.000	0.000	0.000	0.000
6	4.151628e+05	7.667167e+06	0.000	0.000	0.000	0.000	0.000
6	4.151610e+05	7.667164e+06	3.176	-0.174	1.441	1.485	1.403
6	4.151603e+05	7.667163e+06	1.555	0.110	0.757	0.725	0.791
6	4.151582e+05	7.667161e+06	3.034	0.124	1.110	1.082	1.139
6	4.151579e+05	7.667158e+06	2.594	0.028	0.401	0.352	0.452
6	4.151561e+05	7.667140e+06	17.905	1.632	2.038	1.856	2.231
6	4.151571e+05	7.667135e+06	5.547	0.900	0.500	0.440	0.570
6	4.151596e+05	7.667105e+06	30.020	4.193	2.071	1.798	2.405
6	4.151598e+05	7.667096e+06	8.861	0.862	0.870	0.865	0.875
6	4.151620e+05	7.667084e+06	12.518	-0.379	0.886	0.777	0.983
6	4.151641e+05	7.667065e+06	18.612	3.455	1.133	0.921	1.390
6	4.151675e+05	7.667044e+06	21.348	4.336	1.152	0.963	1.384
6	4.151699e+05	7.667021e+06	23.611	4.333	1.022	0.913	1.158
6	4.151735e+05	7.666992e+06	0.000	0.000	0.000	0.000	0.000
7	4.152151e+05	7.666991e+06	0.000	0.000	0.000	0.000	0.000
7	4.152142e+05	7.666989e+06	1.771	0.780	1.036	0.888	1.282
7	4.152126e+05	7.666987e+06	2.749	0.229	1.301	1.206	1.410
7	4.152120e+05	7.666985e+06	1.810	0.046	0.859	0.791	0.927
7	4.152110e+05	7.666982e+06	2.827	0.332	1.225	1.028	1.431
7	4.152099e+05	7.666980e+06	2.634	0.581	1.987	1.555	2.523
7	4.152095e+05	7.666979e+06	1.082	0.290	0.887	0.725	1.105
7	4.152088e+05	7.666977e+06	2.203	0.456	1.616	1.255	2.050
7	4.152083e+05	7.666976e+06	1.402	0.433	1.204	0.956	1.555
7	4.152078e+05	7.666974e+06	1.622	0.348	1.267	1.079	1.516
7	4.152071e+05	7.666973e+06	1.385	0.143	0.993	0.895	1.100
7	4.152066e+05	7.666971e+06	1.742	0.194	0.978	0.896	1.071
7	4.152058e+05	7.666969e+06	2.182	0.153	0.920	0.878	0.966
7	4.152046e+05	7.666967e+06	2.856	0.093	0.712	0.668	0.757
7	4.152020e+05	7.666961e+06	0.000	0.000	0.000	0.000	0.000
8	4.152056e+05	7.666999e+06	0.000	0.000	0.000	0.000	0.000
8	4.152085e+05	7.666998e+06	3.093	0.098	1.140	1.070	1.207
8	4.152105e+05	7.666996e+06	2.769	0.333	1.364	1.222	1.528
8	4.152114e+05	7.666994e+06	1.809	0.136	1.084	1.023	1.150
8	4.152123e+05	7.666993e+06	1.726	0.068	1.432	0.824	1.977
8	4.152130e+05	7.666991e+06	1.682	1.179	0.978	0.809	1.325
8	4.152148e+05	7.666988e+06	4.021	0.704	0.943	0.812	1.095

8	4.152169e+05	7.666982e+06	6.281	0.977	1.536	1.262	1.826
8	4.152180e+05	7.666978e+06	4.011	1.036	1.047	0.856	1.289
8	4.152209e+05	7.666973e+06	5.722	1.105	1.599	1.294	1.974
8	4.152221e+05	7.666970e+06	0.000	0.000	0.000	0.000	0.000
9	4.150535e+05	7.667071e+06	0.000	0.000	0.000	0.000	0.000
9	4.150551e+05	7.667069e+06	2.684	-0.667	1.153	1.403	0.988
9	4.150551e+05	7.667067e+06	1.607	0.028	0.872	0.833	0.911
9	4.150548e+05	7.667065e+06	2.313	0.168	1.079	0.861	1.296
9	4.150540e+05	7.667062e+06	2.834	0.812	0.603	0.589	0.620
9	4.150564e+05	7.667051e+06	0.000	0.000	0.000	0.000	0.000
10	4.151092e+05	7.666977e+06	0.000	0.000	0.000	0.000	0.000
10	4.151117e+05	7.666976e+06	3.047	0.240	1.630	1.442	1.803
10	4.151131e+05	7.666975e+06	1.602	0.415	0.940	0.706	1.243
10	4.151147e+05	7.666972e+06	3.098	0.878	1.005	0.736	1.371
10	4.151169e+05	7.666967e+06	5.521	1.726	1.550	1.160	2.113
10	4.151187e+05	7.666964e+06	4.101	1.124	2.595	1.998	3.465
10	4.151191e+05	7.666963e+06	0.000	0.000	0.000	0.000	0.000
11	4.151711e+05	7.666970e+06	0.000	0.000	0.000	0.000	0.000
11	4.151708e+05	7.666969e+06	0.939	0.194	1.375	1.156	1.659
11	4.151707e+05	7.666969e+06	0.698	0.095	1.062	1.028	1.105
11	4.151702e+05	7.666968e+06	0.672	-0.036	0.689	0.641	0.732
11	4.151703e+05	7.666967e+06	1.461	0.124	0.976	0.879	1.083
11	4.151696e+05	7.666965e+06	1.835	0.176	1.125	1.003	1.254
11	4.151688e+05	7.666963e+06	1.857	0.284	2.561	2.185	3.022
11	4.151687e+05	7.666963e+06	0.358	0.030	0.514	0.477	0.554
11	4.151680e+05	7.666962e+06	1.579	0.108	1.097	1.043	1.157
11	4.151674e+05	7.666960e+06	0.000	0.000	0.000	0.000	0.000
12	4.156635e+05	7.667184e+06	0.000	0.000	0.000	0.000	0.000
12	4.156692e+05	7.667178e+06	7.872	-0.118	1.490	1.487	1.492
12	4.156726e+05	7.667176e+06	3.834	0.355	0.991	0.882	1.112
12	4.156766e+05	7.667174e+06	4.888	0.650	1.338	1.110	1.595
12	4.156793e+05	7.667171e+06	3.921	0.908	1.273	1.070	1.553
12	4.156808e+05	7.667168e+06	3.453	0.435	1.281	1.111	1.475
12	4.156826e+05	7.667166e+06	2.812	0.464	1.074	0.931	1.241
12	4.156843e+05	7.667163e+06	3.343	0.511	0.855	0.778	0.944
12	4.156851e+05	7.667157e+06	5.736	0.421	0.707	0.681	0.736
12	4.156879e+05	7.667145e+06	12.675	0.343	2.079	2.037	2.119
12	4.156889e+05	7.667141e+06	3.333	0.337	0.642	0.603	0.685
12	4.156915e+05	7.667132e+06	9.487	0.549	1.020	0.895	1.143
12	4.156957e+05	7.667121e+06	11.663	2.200	0.712	0.616	0.827

12	4.157081e+05	7.667092e+06	31.841	4.392	2.366	2.055	2.680
12	4.157106e+05	7.667084e+06	0.000	0.000	0.000	0.000	0.000
13	4.161403e+05	7.667209e+06	0.000	0.000	0.000	0.000	0.000
13	4.161418e+05	7.667206e+06	3.338	-1.044	0.879	1.063	0.768
13	4.161431e+05	7.667203e+06	3.209	0.034	1.198	1.150	1.246
13	4.161449e+05	7.667201e+06	2.384	0.127	0.950	0.878	1.025
13	4.161472e+05	7.667199e+06	3.085	0.313	1.617	1.483	1.771
13	4.161477e+05	7.667198e+06	1.363	0.058	1.677	1.599	1.773
13	4.161479e+05	7.667198e+06	0.450	-0.053	0.535	0.424	0.634
13	4.161489e+05	7.667196e+06	1.686	0.318	1.192	1.113	1.310
13	4.161496e+05	7.667195e+06	1.242	-0.177	0.790	0.810	0.774
13	4.161506e+05	7.667194e+06	1.792	0.067	0.767	0.670	0.864
13	4.161527e+05	7.667191e+06	3.664	0.538	1.767	1.535	2.059
13	4.161534e+05	7.667190e+06	1.450	0.095	0.969	0.961	0.978
13	4.161542e+05	7.667188e+06	1.606	-0.042	0.407	0.349	0.464
13	4.161613e+05	7.667180e+06	10.521	1.125	1.682	1.517	1.859
13	4.161639e+05	7.667177e+06	4.649	0.540	1.878	1.672	2.124
13	4.161647e+05	7.667175e+06	1.540	0.061	0.600	0.497	0.712
13	4.161680e+05	7.667171e+06	5.218	0.845	2.727	2.321	3.233
13	4.161685e+05	7.667170e+06	0.940	0.124	0.392	0.339	0.452
13	4.161733e+05	7.667164e+06	8.112	1.225	1.787	1.535	2.074
13	4.161751e+05	7.667161e+06	3.423	0.506	1.038	0.935	1.156
13	4.161774e+05	7.667158e+06	4.013	0.344	0.669	0.507	0.848
13	4.161839e+05	7.667147e+06	12.416	3.002	1.941	1.556	2.523
13	4.161868e+05	7.667144e+06	4.582	0.412	0.872	0.772	0.981
13	4.161907e+05	7.667137e+06	7.566	1.046	2.902	2.514	3.369
13	4.161914e+05	7.667136e+06	1.143	0.118	0.623	0.601	0.648
13	4.161929e+05	7.667133e+06	0.000	0.000	0.000	0.000	0.000
14	4.162322e+05	7.667121e+06	0.000	0.000	0.000	0.000	0.000
14	4.162332e+05	7.667122e+06	1.418	-0.361	1.132	1.303	1.033
14	4.162342e+05	7.667121e+06	1.026	0.183	1.423	1.192	1.698
14	4.162346e+05	7.667121e+06	0.722	0.128	1.620	1.346	1.928
14	4.162349e+05	7.667120e+06	0.410	0.092	0.930	0.772	1.133
14	4.162352e+05	7.667120e+06	0.696	0.114	0.857	0.702	1.039
14	4.162365e+05	7.667119e+06	1.378	0.293	1.744	1.460	2.152
14	4.162367e+05	7.667119e+06	0.582	0.023	0.664	0.555	0.781
14	4.162379e+05	7.667118e+06	1.613	0.260	1.486	1.232	1.771
14	4.162384e+05	7.667117e+06	1.097	0.271	1.198	0.960	1.506
14	4.162382e+05	7.667115e+06	1.206	0.258	1.144	0.902	1.444
14	4.162382e+05	7.667114e+06	1.450	0.352	0.603	0.491	0.743

14 4.162389e+05 7.667108e+06 6.307 1.387 2.114 1.711 2.713  
 14 4.162394e+05 7.667106e+06 1.828 0.073 0.655 0.606 0.704  
 14 4.162385e+05 7.667101e+06 4.818 0.396 1.289 1.183 1.406  
 14 4.162381e+05 7.667098e+06 3.349 0.207 1.051 0.945 1.155  
 14 4.162380e+05 7.667094e+06 3.776 0.596 1.262 1.036 1.526  
 14 4.162376e+05 7.667091e+06 0.000 0.000 0.000 0.000 0.000  
 15 4.162488e+05 7.667245e+06 0.000 0.000 0.000 0.000 0.000  
 15 4.162512e+05 7.667241e+06 4.436 -2.187 0.689 0.849 0.609  
 15 4.162548e+05 7.667237e+06 6.108 0.308 1.574 1.489 1.663  
 15 4.162550e+05 7.667234e+06 2.692 0.100 1.204 1.161 1.248  
 15 4.162560e+05 7.667232e+06 2.012 0.087 0.740 0.689 0.793  
 15 4.162575e+05 7.667228e+06 4.118 0.292 2.009 1.875 2.151  
 15 4.162578e+05 7.667227e+06 1.180 0.087 0.561 0.519 0.606  
 15 4.162602e+05 7.667223e+06 4.377 0.363 1.626 1.483 1.786  
 15 4.162609e+05 7.667222e+06 1.910 0.113 0.571 0.533 0.611  
 15 4.162642e+05 7.667216e+06 6.719 0.516 1.219 1.090 1.356  
 15 4.162670e+05 7.667211e+06 5.544 0.705 0.853 0.790 0.924  
 15 4.162701e+05 7.667202e+06 9.321 0.688 1.402 1.287 1.524  
 15 4.162728e+05 7.667197e+06 5.650 0.578 1.001 0.755 1.270  
 15 4.162755e+05 7.667189e+06 8.456 2.598 1.397 1.129 1.795  
 15 4.162771e+05 7.667183e+06 6.786 0.997 1.605 1.420 1.846  
 15 4.162780e+05 7.667180e+06 3.061 0.011 0.579 0.513 0.645  
 15 4.162811e+05 7.667170e+06 10.238 1.151 1.727 1.526 1.949  
 15 4.162823e+05 7.667166e+06 4.388 0.587 1.381 1.227 1.558  
 15 4.162833e+05 7.667163e+06 2.940 0.328 0.718 0.641 0.802  
 15 4.162846e+05 7.667156e+06 7.152 0.822 1.088 0.950 1.242  
 15 4.162864e+05 7.667148e+06 7.758 1.052 0.952 0.785 1.142  
 15 4.162884e+05 7.667137e+06 12.039 2.501 1.486 1.253 1.805  
 15 4.162899e+05 7.667129e+06 7.360 0.694 0.801 0.703 0.908  
 15 4.162916e+05 7.667115e+06 0.000 0.000 0.000 0.000 0.000  
 16 4.162826e+05 7.667213e+06 0.000 0.000 0.000 0.000 0.000  
 16 4.162824e+05 7.667211e+06 1.225 -0.253 0.970 1.035 0.925  
 16 4.162824e+05 7.667210e+06 1.173 0.119 1.473 1.316 1.644  
 16 4.162823e+05 7.667209e+06 0.684 0.092 0.830 0.652 1.031  
 16 4.162823e+05 7.667208e+06 1.451 0.360 2.427 1.913 3.085  
 16 4.162824e+05 7.667208e+06 0.393 0.088 1.113 1.048 1.210  
 16 4.162823e+05 7.667208e+06 0.347 -0.046 0.243 0.196 0.288  
 16 4.162834e+05 7.667202e+06 5.685 0.538 2.451 2.251 2.652  
 16 4.162836e+05 7.667201e+06 1.273 0.259 1.108 0.856 1.415  
 16 4.162839e+05 7.667199e+06 1.673 0.469 1.432 1.108 1.865

16 4.162841e+05 7.667198e+06 1.381 0.349 0.924 0.768 1.131  
 16 4.162845e+05 7.667196e+06 2.458 0.413 1.005 0.892 1.144  
 16 4.162845e+05 7.667192e+06 3.177 0.316 1.931 1.752 2.137  
 16 4.162844e+05 7.667191e+06 1.006 0.067 1.307 1.148 1.467  
 16 4.162844e+05 7.667191e+06 0.769 0.155 1.155 0.896 1.459  
 16 4.162843e+05 7.667190e+06 0.939 0.275 0.557 0.462 0.684  
 16 4.162843e+05 7.667185e+06 4.947 1.001 1.405 1.226 1.648  
 16 4.162842e+05 7.667182e+06 3.200 0.137 0.901 0.770 1.026  
 16 4.162841e+05 7.667177e+06 0.000 0.000 0.000 0.000 0.000  
 17 4.163186e+05 7.667162e+06 0.000 0.000 0.000 0.000 0.000  
 17 4.163205e+05 7.667159e+06 3.131 -0.061 1.190 1.124 1.251  
 17 4.163213e+05 7.667157e+06 2.456 0.306 1.039 0.973 1.115  
 17 4.163218e+05 7.667154e+06 2.693 0.118 0.848 0.795 0.904  
 17 4.163228e+05 7.667150e+06 4.127 0.221 1.176 1.098 1.256  
 17 4.163233e+05 7.667147e+06 3.492 0.362 1.203 1.086 1.330  
 17 4.163236e+05 7.667144e+06 0.000 0.000 0.000 0.000 0.000  
 18 4.162591e+05 7.667157e+06 0.000 0.000 0.000 0.000 0.000  
 18 4.162611e+05 7.667157e+06 1.984 -0.353 1.312 1.520 1.167  
 18 4.162619e+05 7.667156e+06 1.029 0.065 0.968 0.909 1.032  
 18 4.162631e+05 7.667156e+06 1.248 0.081 0.804 0.750 0.861  
 18 4.162652e+05 7.667155e+06 2.239 0.189 1.589 1.448 1.747  
 18 4.162660e+05 7.667155e+06 1.026 0.063 1.017 0.914 1.123  
 18 4.162667e+05 7.667154e+06 0.000 0.000 0.000 0.000 0.000  
 19 4.143635e+05 7.666935e+06 0.000 0.000 0.000 0.000 0.000  
 19 4.143730e+05 7.666931e+06 10.349 -1.107 1.562 1.739 1.428  
 19 4.143755e+05 7.666928e+06 4.103 0.303 1.182 1.114 1.256  
 19 4.143779e+05 7.666925e+06 3.287 0.129 1.142 1.079 1.207  
 19 4.143797e+05 7.666923e+06 2.780 0.161 0.785 0.814 0.754  
 19 4.143829e+05 7.666920e+06 4.524 -0.253 0.900 0.914 0.886  
 19 4.143860e+05 7.666916e+06 5.359 0.073 0.853 0.803 0.903  
 19 4.143883e+05 7.666908e+06 7.945 0.485 1.583 1.496 1.681  
 19 4.143899e+05 7.666905e+06 3.452 0.083 1.464 1.426 1.501  
 19 4.143909e+05 7.666904e+06 1.775 0.129 0.332 0.310 0.355  
 19 4.143994e+05 7.666887e+06 0.000 0.000 0.000 0.000 0.000  
 20 4.143450e+05 7.666841e+06 0.000 0.000 0.000 0.000 0.000  
 20 4.143450e+05 7.666840e+06 1.194 -0.036 0.636 0.573 0.697  
 20 4.143472e+05 7.666838e+06 3.152 0.298 1.203 1.076 1.346  
 20 4.143468e+05 7.666835e+06 2.711 0.340 1.529 1.318 1.766  
 20 4.143477e+05 7.666834e+06 1.597 0.314 0.615 0.568 0.674  
 20 4.143504e+05 7.666829e+06 5.602 0.492 2.506 2.271 2.813

20 4.143509e+05 7.666828e+06 0.918 -0.054 0.296 0.274 0.317  
 20 4.143535e+05 7.666818e+06 0.000 0.000 0.000 0.000 0.000  
 21 4.143656e+05 7.666847e+06 0.000 0.000 0.000 0.000 0.000  
 21 4.143662e+05 7.666846e+06 0.844 -0.231 1.194 1.507 1.018  
 21 4.143665e+05 7.666846e+06 0.491 0.040 0.791 0.687 0.903  
 21 4.143673e+05 7.666845e+06 0.977 0.134 0.891 0.733 1.077  
 21 4.143682e+05 7.666844e+06 1.716 0.337 1.494 1.253 1.785  
 21 4.143685e+05 7.666843e+06 1.126 0.211 1.243 1.010 1.507  
 21 4.143691e+05 7.666842e+06 1.101 0.251 1.398 1.112 1.774  
 21 4.143693e+05 7.666841e+06 0.859 0.169 0.854 0.767 0.966  
 21 4.143700e+05 7.666840e+06 1.576 0.153 0.813 0.739 0.897  
 21 4.143714e+05 7.666837e+06 2.878 0.266 1.145 1.044 1.258  
 21 4.143728e+05 7.666835e+06 2.648 0.251 1.504 1.377 1.640  
 21 4.143734e+05 7.666834e+06 1.445 0.167 0.964 0.815 1.127  
 21 4.143740e+05 7.666832e+06 2.077 0.363 1.688 1.425 2.025  
 21 4.143743e+05 7.666831e+06 0.000 0.000 0.000 0.000 0.000  
 22 4.140078e+05 7.666874e+06 0.000 0.000 0.000 0.000 0.000  
 22 4.140101e+05 7.666873e+06 2.390 -0.948 1.006 1.389 0.815  
 22 4.140117e+05 7.666873e+06 1.659 0.056 0.893 0.841 0.945  
 22 4.140134e+05 7.666871e+06 2.327 0.182 1.301 1.201 1.409  
 22 4.140149e+05 7.666871e+06 1.592 0.109 0.828 0.729 0.934  
 22 4.140173e+05 7.666869e+06 2.853 0.396 0.673 0.581 0.775  
 22 4.140233e+05 7.666863e+06 8.444 1.311 0.955 0.800 1.138  
 22 4.140307e+05 7.666853e+06 12.746 2.101 1.678 1.466 1.994  
 22 4.140336e+05 7.666849e+06 5.063 -0.262 0.777 0.749 0.802  
 22 4.140375e+05 7.666841e+06 8.621 0.689 1.891 1.734 2.071  
 22 4.140388e+05 7.666839e+06 2.689 0.080 0.590 0.552 0.629  
 22 4.140422e+05 7.666831e+06 8.496 0.548 1.086 1.018 1.159  
 22 4.140452e+05 7.666823e+06 8.197 0.525 1.395 1.344 1.454  
 22 4.140474e+05 7.666819e+06 0.000 0.000 0.000 0.000 0.000  
 23 4.140666e+05 7.666812e+06 0.000 0.000 0.000 0.000 0.000  
 23 4.140695e+05 7.666813e+06 3.160 -1.762 1.008 1.617 0.793  
 23 4.140710e+05 7.666812e+06 2.141 0.340 1.229 1.050 1.434  
 23 4.140728e+05 7.666811e+06 1.993 0.365 1.014 0.889 1.170  
 23 4.140743e+05 7.666809e+06 2.568 0.254 0.702 0.568 0.853  
 23 4.140772e+05 7.666802e+06 7.052 1.454 1.272 1.015 1.579  
 23 4.140804e+05 7.666796e+06 6.868 1.733 1.197 1.078 1.380  
 23 4.140821e+05 7.666791e+06 5.780 -0.358 0.928 0.811 1.032  
 23 4.140847e+05 7.666783e+06 0.000 0.000 0.000 0.000 0.000  
 24 4.139768e+05 7.666797e+06 0.000 0.000 0.000 0.000 0.000

24 4.139778e+05 7.666795e+06 2.070 -0.279 1.435 1.442 1.430  
 24 4.139782e+05 7.666794e+06 1.275 0.485 0.718 0.522 0.996  
 24 4.139788e+05 7.666789e+06 4.959 1.643 3.310 2.386 4.435  
 24 4.139785e+05 7.666788e+06 0.967 0.432 1.082 0.725 1.600  
 24 4.139784e+05 7.666786e+06 1.925 0.817 0.573 0.483 0.701  
 24 4.139760e+05 7.666775e+06 0.000 0.000 0.000 0.000 0.000  
 25 4.139897e+05 7.666840e+06 0.000 0.000 0.000 0.000 0.000  
 25 4.139862e+05 7.666837e+06 4.443 -1.353 1.144 1.509 0.937  
 25 4.139840e+05 7.666836e+06 2.619 0.104 1.288 1.191 1.378  
 25 4.139823e+05 7.666835e+06 1.915 0.295 0.786 0.700 0.886  
 25 4.139790e+05 7.666833e+06 4.001 0.402 1.161 0.986 1.349  
 25 4.139762e+05 7.666830e+06 4.011 0.811 0.968 0.833 1.133  
 25 4.139722e+05 7.666825e+06 6.074 0.911 2.130 1.809 2.523  
 25 4.139709e+05 7.666824e+06 1.758 0.217 0.846 0.785 0.915  
 25 4.139691e+05 7.666822e+06 3.020 0.250 0.708 0.714 0.701  
 25 4.139662e+05 7.666816e+06 6.351 -0.194 1.843 1.907 1.785  
 25 4.139651e+05 7.666815e+06 1.885 0.072 0.751 0.721 0.782  
 25 4.139638e+05 7.666811e+06 3.644 0.175 1.395 1.316 1.473  
 25 4.139626e+05 7.666809e+06 2.129 0.170 0.893 0.806 0.988  
 25 4.139615e+05 7.666806e+06 3.185 0.306 0.756 0.641 0.885  
 25 4.139592e+05 7.666799e+06 0.000 0.000 0.000 0.000 0.000  
 26 4.138855e+05 7.666821e+06 0.000 0.000 0.000 0.000 0.000  
 26 4.138863e+05 7.666818e+06 2.610 -0.976 0.863 1.108 0.724  
 26 4.138864e+05 7.666816e+06 2.432 0.001 1.540 1.534 1.545  
 26 4.138861e+05 7.666815e+06 1.066 0.040 0.762 0.714 0.812  
 26 4.138859e+05 7.666813e+06 2.033 0.132 0.859 0.803 0.918  
 26 4.138853e+05 7.666810e+06 3.174 0.241 0.936 0.826 1.054  
 26 4.138835e+05 7.666806e+06 4.467 0.601 1.859 1.619 2.127  
 26 4.138827e+05 7.666804e+06 0.000 0.000 0.000 0.000 0.000  
 27 4.138948e+05 7.666819e+06 0.000 0.000 0.000 0.000 0.000  
 27 4.138939e+05 7.666817e+06 1.433 -0.201 0.955 0.744 1.112  
 27 4.138934e+05 7.666815e+06 1.951 0.710 1.711 1.281 2.406  
 27 4.138932e+05 7.666814e+06 1.140 0.207 1.026 0.856 1.224  
 27 4.138931e+05 7.666813e+06 1.562 0.294 0.569 0.553 0.588  
 27 4.138929e+05 7.666807e+06 6.061 0.252 1.116 1.052 1.183  
 27 4.138925e+05 7.666801e+06 0.000 0.000 0.000 0.000 0.000  
 28 4.136808e+05 7.666876e+06 0.000 0.000 0.000 0.000 0.000  
 28 4.136824e+05 7.666868e+06 7.471 -0.578 1.946 2.135 1.806  
 28 4.136826e+05 7.666866e+06 2.143 0.345 0.651 0.545 0.771  
 28 4.136848e+05 7.666859e+06 7.202 1.393 0.690 0.591 0.804

28	4.136930e+05	7.666839e+06	21.478	3.399	2.775	2.292	3.470
28	4.136945e+05	7.666837e+06	3.186	-0.078	0.310	0.248	0.374
28	4.137048e+05	7.666801e+06	37.199	5.253	1.549	1.328	1.801
28	4.137106e+05	7.666781e+06	21.124	3.579	1.108	0.956	1.283
28	4.137168e+05	7.666758e+06	0.000	0.000	0.000	0.000	0.000
29	4.146726e+05	7.666991e+06	0.000	0.000	0.000	0.000	0.000
29	4.146713e+05	7.666986e+06	5.301	-3.086	1.303	3.018	0.881
29	4.146714e+05	7.666984e+06	2.099	0.331	1.429	1.201	1.689
29	4.146716e+05	7.666983e+06	1.436	0.255	0.899	0.795	1.022
29	4.146713e+05	7.666980e+06	2.384	0.282	0.491	0.419	0.571
29	4.146768e+05	7.666969e+06	12.898	1.912	1.420	1.203	1.678
29	4.146824e+05	7.666962e+06	0.000	0.000	0.000	0.000	0.000
30	4.153514e+05	7.667078e+06	0.000	0.000	0.000	0.000	0.000
30	4.153521e+05	7.667078e+06	0.676	-0.554	0.613	1.236	0.393
30	4.153527e+05	7.667078e+06	0.648	-0.181	0.629	0.566	0.676
30	4.153538e+05	7.667077e+06	1.420	0.190	0.568	0.450	0.702
30	4.153578e+05	7.667072e+06	0.000	0.000	0.000	0.000	0.000
31	4.155267e+05	7.667132e+06	0.000	0.000	0.000	0.000	0.000
31	4.155278e+05	7.667132e+06	1.193	-0.397	0.880	1.118	0.739
31	4.155288e+05	7.667132e+06	1.089	-0.021	0.608	0.581	0.633
31	4.155317e+05	7.667131e+06	3.011	0.119	1.198	1.135	1.260
31	4.155338e+05	7.667130e+06	2.354	0.177	1.032	0.958	1.112
31	4.155362e+05	7.667129e+06	2.556	0.182	1.029	0.940	1.127
31	4.155387e+05	7.667128e+06	2.833	0.254	0.766	0.701	0.840
31	4.155436e+05	7.667125e+06	5.764	0.505	1.218	1.117	1.329
31	4.155478e+05	7.667123e+06	4.688	0.470	1.897	1.736	2.073
31	4.155491e+05	7.667122e+06	1.567	0.133	1.286	1.177	1.405